Quantum Transport of Non-Interacting Electrons in 2D Systems of Arbitrary Geometries

by

Dominique Dresen

Master Thesis in Physics

Submitted to the

Faculty of Mathematics, Computer Science and Natural Sciences

Institute of Quantum Information

RWTH Aachen University

in September 2014

Supervised by Prof. Dr. Hassler

I declare that I have developed and written the enclosed Master Thesis completely by myself, and have not used sources or means without declaration in the text. Any thoughts from others or literal quotations are clearly marked. The Master Thesis was not used in the same or in a similar version to achieve an academic grading or is being published elsewhere.

Aachen, September 15, 2014

_____

Dominique Dresen

Abstract

We give a comprehensive introduction to the scattering formalism for describing the transport properties of systems, characterized by a single-particle Hamiltonian. A derivation of the scattering matrix from the Hamiltonian is shown. We discuss the relevant properties of the scattering matrix, as well as the connection to transport properties, such as the conductance and density of states. Furthermore, it is shown how the present formalism relates to the Weidenmüller formula from nuclear physics, and the non-equilibrium Green's function formalism. As an application, the scattering formalism is used to numerically study the transport in a 2DEG of for example GaAs heterojunctions, and the transport in graphene systems. We discuss disorder, comparing the results obtained from Born approximation to the numerically obtained results, and evaluate the localization scaling function. Furthermore, the integer quantum Hall effect is discussed and simulated via a Peierls substitution in both setups. For graphene, we describe how to minimize the contact resistance, when leads are attached to the system, in a numerically efficient way by introducing an impedance matching zone in between. As examples, we discuss and simulate a quantum point contact and the Aharonov-Bohm effect. Moreover, we discuss and simulate strain on the lattice, and their implications on the breakdown of the quantum Hall effect in suspended graphene. Finally, we discuss strain induced long-range disorder. For the latter, we use the staggered fermion model to simulate a single Dirac cone and extend the model by a magnetic field. This enables us to discuss the effects of long-range disorder, while simulating only local disorder.

Contents

1. Introduction

1.1. The Future of Electronics

Nowadays, it is hard to enter a room, which contains no electronic devices. All of our daily lives became more and more dependent on little electronic components. For example, the center of any office room nowadays is a personal computer, and it is hard to imagine a life without them. The basis for most of the modern technologies are integrated circuits, which are based on silicon. Since the invention of the first transistors around 1950 in the Bell Laboratories, which could be fabricated by hand, the computational power of the circuits is mainly increased by scaling down the size of the components. The miniaturization proceeded at a breathtaking pace. Whereas, a microprocessor counted about 2000 transistors in 1970, modern processors count several billion transistors on a single chip today. Gordon Moore, co-founder of Intel, conjectured already in 1965 a doubling of this count every two years, which became a self fulfilling prophecy coined as "Moore's law".

But in our present years, the pace starts to slow down. Thermodynamics and quantum physics set bounds on the progress in miniaturization. As silicon transistors are made out of atoms, the reduction of the system size will ultimately have to stop. It is already foreseeable that the stop will happen in the next one or two decades. Alternative approaches are needed for the future of electronics if the performance of electric devices still wants to be increased. Already now, advances in computational power are mostly obtained by the use of multiple central processing units. These can be used in a parallel fashion, whenever the algorithms allow it, to increase the computational speed. But there are many other approaches for the advancement in electronics, which are pursued in current research groups.

One idea is to make more explicit use of quantum mechanics to solve certain computational problems in a more efficient way. In quantum information, one seeks to build a quantum computer, which could then run algorithms that can make for example use of the superposition property of quantum mechanical states. Due to the possible parallelism in the computation itself, some problems, as the factorization of large prime numbers in Shor's algorithm, can be solved with greater efficiency than on any classical computer. But on the other hand, there are a lot of problems that come with the use of quantum mechanical states for computation. For example, one needs systems with large coherence times to perform the calculations with high fault tolerance. Due to decoherence and other forms of noise the information is easily corrupted. In classical computations, this can be corrected by redundancy, whereas in quantum computation the no-cloning theorem forbids the copying of quantum information. The field of quantum error correction provides algorithms, which could be used for correcting the corrupted data. Therefore, computation could be done if the time scale for the error occurrence is in the order or below the time scale needed to correct the data. Still, up to today there are not many algorithms known in quantum information, which can make use of the quantum

mechanical advantages. Hope is that better understanding may come during the research and once a quantum computer is built. For our use in daily electronics, this research may be still far ahead in time.

Another idea is to make use of different materials. Most of electronics is based on silicon nowadays, which is after oxygen the second most abundant element on Earth's crust. Single crystals of silicon can be grown in industrial scales with a high purity. The monocrystalline silicon can then be used for the fabrication of wafers, as basis for integrated circuits. Silicon can be doped with other elements to increase its generally low intrinsic conductivity, and to produce devices as diodes and transistors. It can withstand high temperatures and electrical powers, and has proven itself for most parts to be a reliable material in present electrical devices.

But silicon does not need to be the only material of choice. In 2004, Andre Geim and Kostya Novoselov found for the first time a method to fabricate in a reproducible fashion a material which is called graphene [1], and for which they were awarded with the Nobel prize in physics just six years later in 2010. Details of its structure and electronic properties are discussed in Chapter 4. Important for the potential use in the electronics of tomorrow are graphenes special properties. It is only one layer of atoms thick and therefore extremely light and nearly transparent. Still, it has a great tensile strength and is an excellent conductor with high carrier mobility at room temperature. Graphene transistors operating in the order of $f = 100\,\text{GHz}$ have been reported [2], which is higher than the frequency of a silicon transistor of the same size. Still, problems arise in the usage of graphene transistors in logical circuits, as bulk graphene has no bandgap and the transistors can not be switched off. It is essential to understand how the material behaves in different setups, as to come up with promising ways to tap the possibilities.

1.2. Mesoscopic Physics

In this thesis, we are going to discuss methods to simulate numerically the electronic properties of small systems. We are going to use methods of mesoscopic physics, which deals with materials of intermediate length scale that lie at the nanometer to micrometer regime. These materials, like graphene, are made up out of thousands of atoms and therefore it is practically impossible to describe them in an atomic basis. But with the understanding of the essential physics, we can identify the important length scales of the problems and virtually simulate quantum mechanical models, which give us an insight into the electronic properties. The quantum mechanical effects, which are visible at this scale, can be quite different from the macroscopic classical laws. For example, according to Ohm's law the conductance G of a macroscopic wire is given by a material constant, the conductivity σ, times the cross sectional area over the length $G = \sigma A/L$. But, if the wire is scaled down, one will notice under certain conditions that the conductance increases only step wise $G = nG_0$, in terms of a quantum of conductance G_0, due to the quantum mechanical nature and the momentum quantization associated with a confinement.

Scattering theory provides a framework to describe and understand mesoscopic systems. In our discussion in the first part of this thesis, we will assume that the Hamiltonian, which will

be used to describe the system, only contains single-particle terms, which means that it does not contain any interaction terms for the electrons. From the viewpoint of Fermi liquid theory, where the basic conclusion is that a gas of interacting particles can be described by a system of almost non-interacting quasiparticles [3], this approximation is in many cases sufficient to describe the essential physics. If wanted, some interaction terms can also be approximated by a Hartree term and added in a single particle Hamiltonian. Furthermore, we will allow in our discussion of scattering theory for a general geometry. Ring structures or certain constrictions for example, can greatly alter the electronic properties of a system due to the wave nature of electrons. The general geometry and additional ingredients like disorder make the used approach numerical by nature. The calculations will result in a scattering matrix, from which we can extract information on the electronic properties by the Landauer-Büttiker formalism.

The mesoscopic system of interest are going to be given by a finite-sized single particle Hamiltonian, and can therefore always be diagonalized. Therefore, the system alone boils down to a discrete set of energy levels. For a transport problem, we have to connect the finite-sized closed system via leads to reservoirs. These are presumed to be at fixed chemical potentials, and for simplicity we will discuss in this thesis only the case of zero temperature. In this open system setup, every reservoir tries now to bring the system into equilibrium with itself. Therefore, the different reservoirs create a non-equilibrium state in the system, where in a stationary state reservoirs acting as sources pump electrons into the system, and reservoirs acting as drains take out electrons from the system. By adding furthermore a backgate, we can imagine that it is possible to tune the Fermi energy of the system. We will see that the thus determined number of open channels will control the conductance of the system.

The framework of a scattering problem with in and outgoing electrons will essentially be the starting point of Ch. 2. We will see, how the general problem can be solved numerically. The Landauer formulation of transport will allow us to interpret the transmission of the system as conductance, and the Büttiker formula finally tells us how measurable quantities like current and voltages have to be treated in the multiterminal case. Having become a standard method in mesoscopic physics, a great amount of literature is available, which discusses the Landauer-Büttiker formalism. To name just a few, a look into [4, 5, 6, 7] is advised.

For practical implementations in the calculation of the scattering matrix, we make use of a recently published Python package that is called kwant [8]. It solves the system of equations, which is going to be presented in Ch. 2, and the easy implementation gives us the possibility to quickly start focusing on more complex aspects. A great advantage of the package is that is free to use and that it can easily be extended and implemented with own codes to improve the analysis.

2. Scattering Theory

In this chapter, we will present the general framework that will be used to describe a mesoscopic system and to calculate transport properties. For this purpose, we identify in Sect. 2.1 a general non-interacting system with a tight binding Hamiltonian. Subsequently, we show how solving the Schrödinger equation of such a system can lead to a quantity which we will identify as the scattering matrix in Sect. 2.2. Before even solving for the scattering matrix, we proof its unitary in Sect. 2.3, and discuss its connection to the the transfer matrix formalism in Sect. 2.4, where we also discuss how the blocks of the scattering matrix are connected to the transmission probability. Afterwards, we derive an equation in Sect. 2.6 to directly solve for the scattering matrix from the Hamiltonian, and we connect it to a formula from nuclear physics, which is known as the Weidenmüller formula. Sect. 2.7 deals with the calculation of the conductance in the Landauer-Büttiker formalism. We also show the equivalence of our derived formula for the scattering matrix to the Non-Equilibrium Green's Function (NEGF) formalism in Sect. 2.8, which is an alternative and common approach to problems in mesoscopic physics. As a last section, we discuss in Sect. 2.9 & 2.10 the density of states of the system, and its connection to the scattering matrix.

After this chapter, the reader should feel ready to tackle any given transport problem of arbitrary geometry, which can be described by a non-interacting Hamiltonian, and he should be able to make quantitative statements about it.

2.1. Defining the System

In general, we are interested in the transport properties of a mesoscopic system of any desired shape, which is connected to an arbitrary number of leads. The geometry can be of any form and any dimension. An example for a 2D system is shown in Fig. 2.1. As we are going to be interested in calculating transport properties from one attached lead to another, the geometry should be connected. Several systems of interest can be described in a model that neglects effects due to interactions and are thus describable by a single-particle Hamiltonian of the form

$$\mathcal{H} = \sum_{i,j} h_{i,j} \left|i\right\rangle \left\langle j\right| , \tag{2.1.1}$$

where i, j represent some coordinates in real-space. We obtain such a Hamiltonian for example if we discretize the continuous Schrödinger equation of an electron

$$\left[\frac{\left(\boldsymbol{p} + e\boldsymbol{A}\right)^2}{2m} + V\right]\Psi = E\Psi \tag{2.1.2}$$

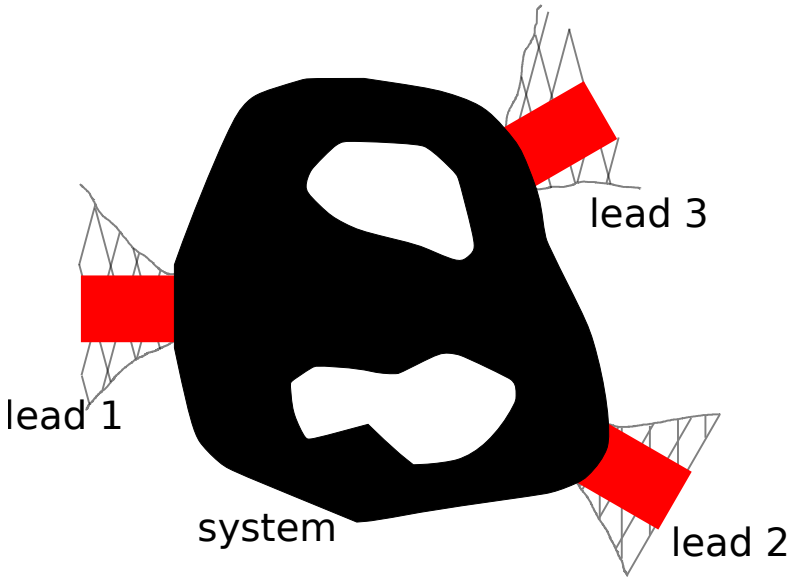

Figure 2.1.: The figure shows an example of a 2-dim system that is connected to three leads. The leads extend infinitely away from the system and are intended to connect the system to reservoirs which are at fixed temperature and chemical potential. The system geometry may be arbitrary but should be connected. In experiments the leads are often widening with distance from the system to prevent localization, which is hinted with the grey background. For a theoretical description, the leads are assumed to be periodic and free of disorder, which is hinted by the red blocks.

in real space on a square lattice. An example of this procedure is given in A.2. It will explicitly be used in the simulation of transport properties of GaAs in Ch. 3. In the following, we choose the convention that the electron charge is given by $q = -e$, with the elementary charge $e > 0$.

Different systems may need other lattice structures. For example, we will also simulate the Dirac equation of an massless electron

$$\Big[v_{\mathsf{F}}\big(\boldsymbol{p} + e\boldsymbol{A}\big) \cdot \boldsymbol{\sigma} + V\Big]\Psi = E\Psi \tag{2.1.3}$$

by using a honeycomb lattice in Ch. 4. The usage of different lattices is summarized in the Hamiltonian given in (2.1.1). It can be understood as having put some lattice structure, appropriate for the system that wants to be discussed, on top of the geometry as depicted in Fig. 2.2. In the following, we will use the notation conventions of [8] and [9].

The Hamiltonian of Eq. (2.1.1) has a certain structure if it is used to describe a mesoscopic system. The Hamiltonian can be split into three parts

$$\mathcal{H} = \mathcal{H}_{\mathsf{L}} + H_{\mathsf{S}} + H_{\mathsf{LS}}. \tag{2.1.4}$$

One Hamiltonian $\mathcal{H}_{\mathsf{L}}$ for the description of the leads, one Hamiltonian H_{S} for the description of the finite-sized mesoscopic system and one part for describing the coupling between the

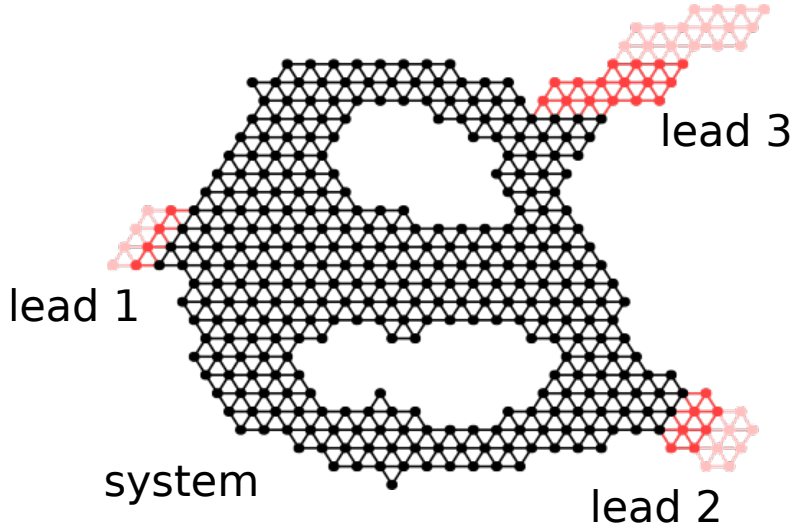

Figure 2.2.: System of Fig. 2.1 on a discrete lattice. The image was created with the Python package kwant [8]. The discretized geometry in the picture represents a tight binding Hamiltonian which can be evaluated numerically. Every dot represents an onsite term whereas every link represents an hopping from one lattice site to another.

system and the lead $H_{\mathsf{LS}} = T_{\mathsf{LS}} + T_{\mathsf{LS}}^{\dagger}$ (where the Hermitian conjugate needs to be added to ensure that the complete Hamiltonian is Hermitian).

For the discussion of transport problems, it is essential that the system of discussion is open. The attachment of H_{S} to the semi-infinite leads make it possible that electrons can enter and leave the system, and therefore that something like a current can be described. In an experiment, the leads are often widening as one distances from the system, which is hinted by the shaded backgrounds of the leads of Fig. 2.1. Otherwise, disorder in the leads would lead to localization as we will see in Ch. 3. Then, the leads are connected to some metal junctions, which lead to the experimental apparatus of voltmeters, etc. to measure the conductance of the system. In the theoretical model, we can assume that the leads are ideal. This means they are free of disorder and extend periodically away from the system. This assumption is necessary to describe the semi-infinite extending leads with only a finite amount of information, and thus enable us to calculate anything. In this case, the leads can be described by unit cell Hamiltonians $H_{\mathsf{L}}^{(\nu)}$, which are connected only to their nearest neighbor unit cell via $T_{\mathsf{L}}^{(\nu)}$ (here ν numbers the leads). For any practically application this should be achievable, if the unit cells of the leads are chosen large enough. The knowledge of the unit cells and the couplings thus suffice to describe the complete semi-infinite leads.

In our notation the N_{L} unit cells of the various lead Hamiltonians are summarized in the

disjoint sections of one effective unit cell Hamiltonian

$$H_{\mathsf{L}} = \begin{pmatrix} H_{\mathsf{L}}^{(1)} & & & \\ & H_{\mathsf{L}}^{(2)} & & \\ & & \ddots & \\ & & & H_{\mathsf{L}}^{(N_{\mathsf{L}})} \end{pmatrix}. \tag{2.1.5}$$

The same thing is done for the couplings between the neighboring unit cells within T_{L}.

Summarizing, the complete Hamiltonian of the open system

$$\mathcal{H} = \mathcal{H}_{\mathsf{L}} + \mathcal{T}_{\mathsf{L}} + \mathcal{T}_{\mathsf{L}}^{\dagger} + H_{\mathsf{S}} + T_{\mathsf{LS}} + T_{\mathsf{LS}}^{\dagger} \tag{2.1.6}$$

consists of the following parts. A semi-infinite part for the collection of unit cells, where in the mathematical description, the collection can be thought of as an effective lead described by

$$\mathcal{H}_{\mathsf{L}} = \sum_{n,\alpha,\beta} H_{\mathsf{L},\alpha,\beta} \left|n,\alpha\right\rangle \left\langle n,\beta\right|. \tag{2.1.7}$$

Here, α and β represent the matrix structure of the unit cells and include any additional degrees of freedom. The unit cells of this effective lead are enumerated by their respective distance to the system $n = 1, \ldots, \infty$. In this enumeration, the system site is considered to be positioned at site $n = 0$. Furthermore, the complete Hamiltonian contains a semi-infinite part for the collection of hoppings between those unit cells

$$\mathcal{T}_{\mathsf{L}} = \sum_{n,\alpha,\beta} T_{\mathsf{L},\alpha,\beta} \left|n+1,\alpha\right\rangle \left\langle n,\beta\right|, \tag{2.1.8}$$

a finite part for the system

$$H_{\mathsf{S}} = \sum_{\alpha\beta} H_{\mathsf{S},\alpha,\beta} \left|0,\alpha\right\rangle \left\langle 0,\beta\right|, \tag{2.1.9}$$

and a finite part for the hopping from the system into the lead

$$T_{\mathsf{LS}} = \sum_{\alpha,\beta} T_{\mathsf{LS},\alpha,\beta} \left|1,\alpha\right\rangle \left\langle 0,\beta\right|. \tag{2.1.10}$$

In matrix notation, the Hamiltonian has the block-tridiagonal form

$$H = \begin{pmatrix} \ddots & T_{\mathsf{L}} & & \\ T_{\mathsf{L}}^{\dagger} & H_{\mathsf{L}} & T_{\mathsf{L}} & \\ & T_{\mathsf{L}}^{\dagger} & H_{\mathsf{L}} & T_{\mathsf{LS}} \\ & & T_{\mathsf{LS}}^{\dagger} & H_{\mathsf{S}} \end{pmatrix}. \tag{2.1.11}$$

This repetitive structure can be depicted as a semi-infinite quasi one-dimensional chain as shown in Fig. 2.3. The matrices H_{L} and T_{L} are square and of the same dimension

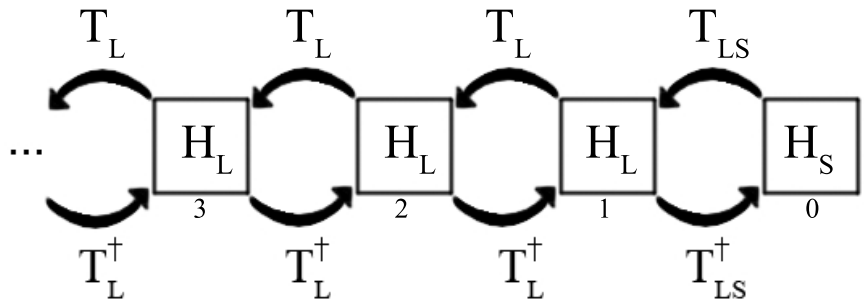

Figure 2.3.: The Hamiltonian (2.1.6) describes a quasi one-dimensional chain. The system is at one side of the chain and connected via T_{LS} to the lead. The lead can be understood as an semi-infinite chain of unit cells described by H_{L} and which are connected to one another by T_{L}.

$\dim(H_{\mathsf{L}}) = \dim(T_{\mathsf{L}}) = d_{\mathsf{L}}$. The system Hamiltonian H_{S} that describes the finite scattering region is an Hermitian matrix with $\dim(H_{\mathsf{S}}) = d_{\mathsf{S}}$. Consequentially, T_{LS} is a $d_{\mathsf{L}} \times d_{\mathsf{S}}$ matrix. The numbers d_{S} and d_{L} are the respective numbers of lattice sites in the system and the lead. The wavefunction of the semi-infinite system is defined here as

$$\Psi = \begin{pmatrix} \vdots \\ \psi^{\mathsf{L}}(2) \\ \psi^{\mathsf{L}}(1) \\ \phi^{\mathsf{S}} \end{pmatrix}. \tag{2.1.12}$$

The vectors $\psi^{\mathsf{L}}(n)$ have d_{L} and ϕ^{S} correspondingly d_{S} components. The dimensions d_{S} and d_{L} are finite as we discretized the real-space, and as the system and lead unit cells extend only about a finite region. In this setup, the problem of solving the Schrödinger equation

$$H\Psi = E\Psi \tag{2.1.13}$$

is now written in terms of a linear algebra problem for a semi-infinite matrix.

2.2. The Effective Lead

Before we turn to the problem of the semi-infinite effective lead connected to a system, we will describe an isolated infinitely extending lead. This will give us a basis set of states corresponding to the asymptotic states deep within the semi-infinite lead. Later, we will use those to solve the Schrödinger equation (2.1.13) for the scattering matrix, which will tell us how one asymptotic state is scattered into another by the system.

The Hamiltonian of the infinite lead, which is translationally invariant, is given by

$$H_{\mathsf{iL}} = \begin{pmatrix} \ddots & T_{\mathsf{L}} & & \\ T_{\mathsf{L}}^\dagger & H_{\mathsf{L}} & T_{\mathsf{L}} & \\ & T_{\mathsf{L}}^\dagger & H_{\mathsf{L}} & T_{\mathsf{L}} \\ & & T_{\mathsf{L}}^\dagger & \ddots \end{pmatrix}. \tag{2.2.1}$$

The translation invariance of the Hamiltonian implies a translational invariance for the eigenstates of the infinite lead and can be used by a Bloch ansatz. The m-th eigenmode can be expressed as

$$\phi_m(n) = (\lambda_m)^n \chi_m. \tag{2.2.2}$$

The state for the transverse mode structure of the corresponding eigenmode is represented by χ_m. With this ansatz, the Schrödinger equation $H_{\mathsf{iL}}\phi_m = E\phi_m$ reads

$$T_{\mathsf{L}}^\dagger(\lambda_m)^{n+1}\chi_m + H_{\mathsf{L}}(\lambda_m)^n\chi_m + T_{\mathsf{L}}(\lambda_m)^{n-1}\chi_m = E(\lambda_m)^n\chi_m, \tag{2.2.3}$$

which simplifies to

$$\left[T_{\mathsf{L}}^\dagger\lambda_m + (H_{\mathsf{L}} - E\mathbb{1}) + T_{\mathsf{L}}\lambda_m^{-1}\right]\chi_m = 0. \tag{2.2.4}$$

Another way to read this equation is to multiply it with λ_m. This way, we deal with the generalized quadratic eigenvalue problem[1]

$$\left[T_{\mathsf{L}}^\dagger\lambda_m^2 + (H_{\mathsf{L}} - E\mathbb{1})\lambda_m + T_{\mathsf{L}}\right]\chi_m = 0. \tag{2.2.5}$$

Introducing the vector

$$x_m = \begin{pmatrix} \chi_m \\ \lambda_m\chi_m \end{pmatrix}, \tag{2.2.6}$$

the problem is equivalent to a general eigenvalue problem

$$\begin{pmatrix} 0 & \mathbb{1} \\ T_{\mathsf{L}} & H_{\mathsf{L}} - E\mathbb{1} \end{pmatrix} x_m = \lambda_m \begin{pmatrix} \mathbb{1} & 0 \\ 0 & -T_{\mathsf{L}}^\dagger \end{pmatrix} x_m. \tag{2.2.7}$$

By solving this equation, which can be done numerically, the λ_m and corresponding χ_m are found. As the general eigenvalue problem stems from a quadratic eigenvalue problem of matrices that are d_{L} dimensional, one finds up to $2d_{\mathsf{L}}$ eigenvalues and the χ_m have d_{L} components.

For the eigenstates (2.2.2) to be normalizable for the semi-infinite lead, the eigenvalues need to fulfill $|\lambda_m| \leq 1$. The modes with an absolute value smaller than one are evanescent, and tend to zero deep within the positive direction of the lead (cf. Eq. (2.2.2) for $n \to \infty$). As the modes with $|\lambda_m| > 1$ are not normalizable, they are not part of the Hilbert space of the semi-infinite system and will be discarded.

[1] The special form of the eigenvalue problem is referred to as palindromic eigenvalue problem in mathematics, and has raised interest in just the previous ten years in numerical mathematics. Especially in the vibrational analysis of buildings, machines or vehicles [10, 11, 12].

The modes with $|\lambda_m| = 1$ are propagating and can be expressed by the longitudinal momentum k_m of mode m by writing $\lambda_m = \exp(ik_m a)$, where k_m is a real number and a is the lattice spacing. Each propagating mode is characterized by its velocity

$$v_m = \frac{1}{\hbar}\frac{\mathrm{d}E}{\mathrm{d}k_m} = \frac{ia}{\hbar}\frac{\mathrm{d}E}{\mathrm{d}\log\lambda_m}. \tag{2.2.8}$$

The velocity is related to the density of states in one dimension. It is given for a state propagating into only a single direction by

$$d(E) = \frac{1}{2\pi}\frac{\mathrm{d}k_m}{\mathrm{d}E} = \frac{1}{2\pi\hbar}\frac{1}{v_m}. \tag{2.2.9}$$

The short derivation of the first equality is analogue to the calculation performed in Appendix A.4 for the density of states in two dimensions. We show in the Appendix A.1.1, by using the Feyman-Hellman theorem, that the particle flux of the propagating states in the lead, which is related to the velocity by $j_m = \rho_m v_m$ (where $\rho_m = \chi_m^\dagger \chi_m$ is the particle density at a single site in the mode m of the lead), is given by

$$j_m = \frac{2a}{\hbar}\chi_m^\dagger \,\mathrm{Im}\big(\lambda_m^* T_\mathsf{L}\big)\chi_m. \tag{2.2.10}$$

By changing the normalization of the propagating states, we can set the particle flux magnitude of the states to unity $\big|j_m\big| = 1$. We will obtain N_o outgoing modes with λ_m^o, χ_m^o, where the current is $j_m = 1$, N_i incoming modes with λ_m^i, χ_m^i, where $j_m = -1$, and N_e evanescent modes with λ_m^e, χ_m^e. The number of incoming and outgoing modes have to be equal $N_\mathsf{o} = N_\mathsf{i} \equiv N_\mathsf{p}$ as the Bloch bands $E(k)$ are periodic. Thus for a given energy E, the band will be intersected equally often for a positive and a negative slope as described in [9]. As it can be easily checked that the eigenstates ϕ_m of the infinite lead form a complete set of basis states on the semi-infinite lead space, we are able to express the states within the semi-infinite lead in terms of

$$\psi_m^\mathsf{L}(n) = \big(\lambda_m^\mathsf{i}\big)^n \chi_m^\mathsf{i} + \sum_{m'=1}^{N_p} S_{m'm}\big(\lambda_{m'}^\mathsf{o}\big)^n \chi_{m'}^\mathsf{o} + \sum_{p}^{N_\mathsf{e}} \tilde{S}_{pm}\big(\lambda_p^\mathsf{e}\big)^n \chi_p^\mathsf{e}, \tag{2.2.11}$$

where the amplitude for the contribution of a mode m to a mode m' are explicitly named as the elements of a scattering matrix $S_{m'm}$. The part of the scattering matrix that gives the amplitude for a mode m to turn into an evanescent mode, is given by $\tilde{S}_{m'm}$. It is not explicitly needed for the calculation of transport properties, and thus will be eliminated in Sect. 2.5 from the system of equations, where we solve the Schrödinger equation (2.1.13) for the scattering matrix. Due to the normalization of the propagating modes to unit flux, the scattering matrix is unitary, which is discussed in Sect. 2.3.

2.3. Unitarity

An element of the scattering matrix is given by the transition amplitude from an incoming asymptotic state of lead α to an outgoing asymptotic state of lead β, which is expressed by

$$S_{\beta\alpha} = \langle \mathsf{out}, \beta | \mathsf{in}, \alpha \rangle \,. \tag{2.3.1}$$

The scattering matrix represents the solution of the Schrödinger equation within a form that is very practicable for discussing transport problems.

Because of the particle conservation $\partial_t \rho + \nabla j = 0$, which can be deduced from the Schrödinger equation, the particle current is conserved in a stationary state $\partial_t \rho = 0$. This means, the currents coming into the system have to be equal to the currents leaving the system. We can conclude from this that the scattering matrix S is unitary if the propagating modes are normalized to unit flux, as we will have the same amount of incoming modes, carrying the flux $j = -1$, and of outgoing modes carrying the flux $j = 1$ and the scattering matrix relates the incoming modes to the outgoing modes. By summarizing all incoming amplitudes in c^{i}, and all outgoing amplitudes in c^{o}, the relation reads $c^{\mathsf{o}} = Sc^{\mathsf{i}}$. Now due to the current conservation, c^{o} needs to be of the same magnitude as c^{i}, and therefore

$$|c^{\mathsf{o}}|^2 = c^{\mathsf{o}\,\dagger} c^{\mathsf{o}} = c^{\mathsf{i}\,\dagger} S^\dagger S c^{\mathsf{i}} \stackrel{!}{=} \left|c^{\mathsf{i}}\right|^2 . \tag{2.3.2}$$

The equality thus demands the unitarity of the scattering matrix

$$S^\dagger S = \mathbb{1}. \tag{2.3.3}$$

This is a very general property of the scattering matrix that is very important for the numerical stability of transport calculations. We show in Appendix A.1.5 explicitly the unitarity property for the expression of the scattering matrix, which is derived in Sect. 2.5.

2.4. Connection of S-Matrix to Transfer Matrix

Before we present the equation to obtain the scattering matrix from the Schrödinger equation, which is done in Sect. 2.5, we want to discuss its connection to the transfer matrix formalism. This will help us to gain an intuitive picture of the scattering matrix. In the transfer matrix formalism one is bound to the description in a two-terminal setup as pictured in Fig. 2.4. Multiterminal system can be reduced to a two-terminal system by describing several leads within an effective lead with disjoint sections, similar to the procedure that we presented in Sect. 2.1.

In a two-terminal device, we can denote the coefficients of the N_{L} incoming and outgoing modes of the left lead as c^{iL}, c^{oL} and correspondingly c^{iR}, c^{oR} for the N_R modes of the right lead. The notation is adapted from [13]. The asymptotic scattering state, where the transport direction is set along the x-axis, is then given by

$$\psi(x) = \begin{cases} \sum_{m=0}^{N_{\mathsf{L}}} [c_m^{\mathsf{iL}} \phi_m^{\mathsf{iL}}(x) + c_m^{\mathsf{oL}} \phi_m^{\mathsf{oL}}(x)] & x \to -\infty, \\ \sum_{m=0}^{N_R} [c_m^{\mathsf{iR}} \phi_m^{\mathsf{iR}}(x) + c_m^{\mathsf{oR}} \phi_m^{\mathsf{oR}}(x)] & x \to +\infty, \end{cases} \tag{2.4.1}$$

where the $\phi(x)$ represent only the propagating states of the respective leads, as all evanescent states have decayed in the asymptotic region. The transfer matrix relates now the incoming and outgoing states of the left lead, to the incoming and outgoing modes of the right leads by

$$\begin{pmatrix} c^{\mathsf{oR}} \\ c^{\mathsf{iR}} \end{pmatrix} = M \begin{pmatrix} c^{\mathsf{iL}} \\ c^{\mathsf{oL}} \end{pmatrix}, \tag{2.4.2}$$

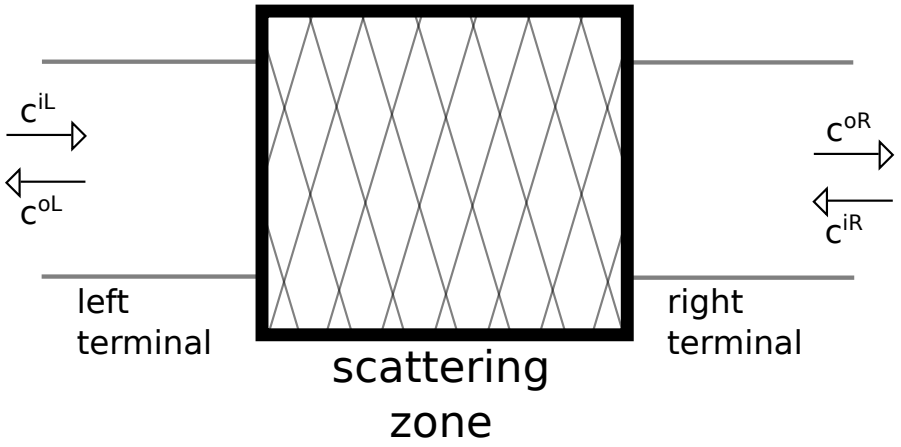

Figure 2.4.: Two-terminal setup, which is used in the transfer matrix formalism. The transfer matrix relates the amplitudes of the incoming and outgoing modes of the left lead c^{iL}, c^{oL}, to the amplitudes of the incoming and outgoing modes of the right lead c^{iR}, c^{oR}. On the other hand, the scattering matrix relates the incoming amplitudes of the left and right terminal c^{iL}, c^{iR} to the outgoing amplitudes c^{oL}, c^{oR}.

where all amplitudes c_m have been grouped into the respective c. The four blocks of the transfer matrix are denoted by

$$M = \begin{pmatrix} m_{11} & m_{12} \\ m_{21} & m_{22} \end{pmatrix}, \tag{2.4.3}$$

where m_{11} and m_{12} are the amplitudes from the incoming and outgoing modes of the left lead associated with the outgoing modes of the right lead, and m_{21}, m_{22} respectively for the incoming modes of the right lead.

An advantage of the transfer matrix is that the connection of two systems, which are connected via a lead, is multiplicative in the transfer matrix formalism. This can be understood from the point that a second scattering zone, which could be positioned right of the one depicted in Fig. 2.4, would have as incoming and outgoing modes c^{iR} and c^{oR}, and thus one would successively go through the system. For modes, which are normalized to a particle flux of unity, the current conservation between the left and the right side of the system implies a conjugate symplectic structure[2] for the transfer matrix

$$M^\dagger \sigma_z M = \sigma_z. \tag{2.4.4}$$

Here, σ_z acts on the left-going and right-going degree of freedom, which is related to the block structure of (2.4.3). Therefore, transfer matrices are elements of the symplectic group

[2]The standard definition of the symplectic property of a matrix A is $A^T i\sigma_y A = i\sigma_y$, where σ_y is a Pauli matrix acting on the left-going and right-going degree of freedom. Replacing the transpose by the conjugate $A^\dagger i\sigma_y A^\dagger = i\sigma_y$, as we did, is referred to as conjugate symplectic. Furthermore, we switched σ_y by σ_z, which can be understood from having obtained M by the rotation $M = R^\dagger A R$, where the unitary rotation matrix is given by $R = (1 + i\sigma_x)/\sqrt{2}$.

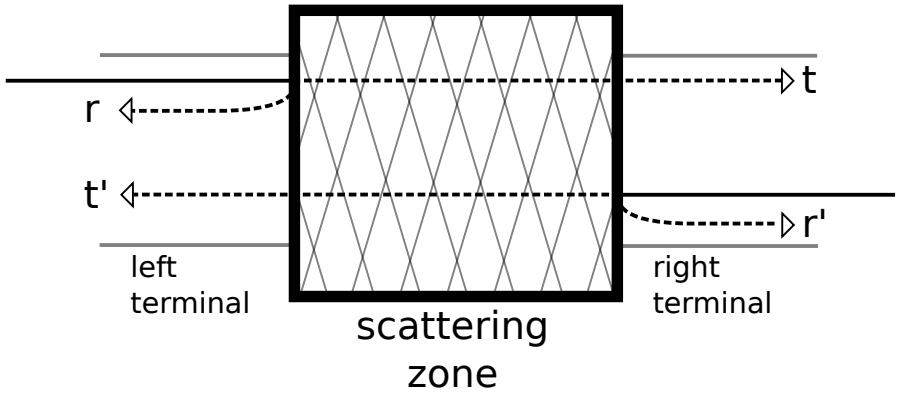

Figure 2.5.: Illustration of the four blocks of a two-terminal scattering matrix. The incoming modes of the left terminal contribute to the outgoing amplitudes of the same terminal via r. Their contribution to the outgoing amplitudes of the right terminal is given by t. Respectively r' and t' are the contribution for the incoming amplitudes of the right terminal.

$M \in \mathrm{SL}(2N_p)$. The conjugate symplectic property (2.4.4) also implies that the magnitude of the determinant of the transfer matrix is always $|\det M| = 1$. However, numerical calculations in the transfer matrix formalism are unstable, as some eigenvalues of the transfer matrix tend to become exponentially large and some eigenvalues become exponentially small. This is a bad conditioning in any numerical evaluation.

However, the scattering matrix formalism can help us to stabilize the numerical calculations, due to the unitary property of the scattering matrix, which restricts every eigenvalue to the magnitude of one. To transform a transfer matrix into a scattering matrix, we compare Eq. (2.4.2) to the relations given by the scattering matrix, where the coefficients of the incoming states are mapped onto the outgoing states by

$$\begin{pmatrix} c^{\mathrm{oL}} \\ c^{\mathrm{oR}} \end{pmatrix} = S \begin{pmatrix} c^{\mathrm{iL}} \\ c^{\mathrm{iR}} \end{pmatrix}. \tag{2.4.5}$$

The four blocks of the scattering matrix are denoted in the two-terminal device by

$$S = \begin{pmatrix} r & t' \\ t & r' \end{pmatrix}, \tag{2.4.6}$$

where r (r') denotes the amplitudes for reflection back to the left (right) lead, and t (t') the transmission from right to left (left to right), which is illustrated in Fig. 2.5. Due to the unitarity of the scattering matrix, which was discused in Sect. 2.3, we can derive relations between the four blocks of a two-terminal system scattering matrix that are listed in Appendix A.1.9.

By simple matrix algebra, we can derive relations between the blocks of the transfer matrix and the blocks of the scattering matrix, which is sketched in A.1.9, and summarized by

$$m_{11} = t^{\dagger -1}, \tag{2.4.7}$$
$$m_{12} = r' t'^{-1}, \tag{2.4.8}$$
$$m_{21} = -t'^{-1} r, \tag{2.4.9}$$
$$m_{22} = t'^{-1}, \tag{2.4.10}$$

$$r = -m_{22}^{-1} m_{21}, \tag{2.4.11}$$
$$t = m_{11}^{\dagger -1}, \tag{2.4.12}$$
$$t' = m_{22}^{-1}, \tag{2.4.13}$$
$$r' = m_{12} m_{22}^{-1}. \tag{2.4.14}$$

These relations map between the transfer matrices from the symplectic group and the scattering matrices, which are part of the unitary group $\mathrm{U}(2N_p)$. The composition of two-terminal devices in the formulation of scattering matrices follow a more complex rule. It can be derived from the matrix multiplication rule of the transfer matrix formalism, and is sketched in Appendix A.1.9.

We note furthermore, that from the block structure of the scattering matrix, we are given the transmission amplitudes of the modes α of the left lead to the modes β of right lead by $t_{\alpha\beta}$, which are simply the entries of t. To calculate the multimode transmission probability for an particle from the left lead to the right lead, we only need to sum the square amplitudes of the various modes

$$T = \sum_{\alpha,\,\beta} |t_{\alpha\beta}|^2 = \mathrm{tr}\Big(tt^\dagger\Big), \tag{2.4.15}$$

which is also known in mathematics as the square of the Frobenius norm of t. We can furthermore use the relations given by the unitarity of the scattering matrix, to show that $\mathrm{tr}(tt^\dagger) = \mathrm{tr}(t't'^\dagger)$. This can be seen by comparing the trace of Eq. (A.1.75) and Eq. (A.1.77). If we define the multimode reflection probability of the left and right lead $R_L = \mathrm{tr}(rr^\dagger)$, $R_R = \mathrm{tr}(r'r'^\dagger)$, the reflection and transmission probabilities always sum up to the number of propagating modes in the corresponding lead $R_L + T = N_L$, $R_R + T = N_R$. This is just a multimode extension of the statement that the probability has to sum up to one for every propagating mode $R_m + T_m = 1$.

From the discussion of the scattering matrix in a two-terminal setup, we can easily understand the structure of the scattering matrix of a multi-terminal device. The block structure of the scattering matrix will just be extended. For a system with M leads, it reads

$$S = \begin{pmatrix} r_1 & t_{12} & \dots & t_{1M} \\ t_{21} & r_2 & & t_{2M} \\ \vdots & & \ddots & \vdots \\ t_{M1} & t_{M2} & \dots & r_M \end{pmatrix}, \tag{2.4.16}$$

where r_i is a square matrix, which has as a dimension the number of propagating modes N_i in the corresponding lead, and contains the reflection amplitudes of lead i. The transmission

amplitudes t_{ij} can be non square and are of dimension $N_i \times N_j$. The transmission probabilities T_{ij} to scatter from lead j into lead i can be defined in the same manner by the square Frobenius norm of every transmission amplitude matrix t_{ij}. Analogue, we can define the reflection probabilities by the Frobenius norm of the reflection amplitudes $R_i = \mathrm{tr}(r_i r_i^\dagger)$. By taking the trace of the unitary relations on the block diagonal of $S^\dagger S = \mathbb{1}$, we obtain relations between the probabilities

$$R_i + \sum_{j \neq i} T_{ji} = N_i. \tag{2.4.17}$$

Furthermore, as the unitarity states $S^\dagger S = S S^\dagger$, a symmety in the transmission probabilities is also implied from

$$N_i - R_i = \sum_{j \neq i} T_{ji} = \sum_{j \neq i} T_{ij}. \tag{2.4.18}$$

The probabilities will be very important in the discussion of the conductance in Sect. 2.7.

2.5. Solving for the Scattering Matrix

We can now insert the lead states in terms of the normalized modes of the infinite lead given by Eq. (2.2.11) into the lower two block rows of the Schrödinger equation (2.1.13), which connect the system with the lead. The remaining rows are solved via the definition of the infinite lead states. Using Eq. (2.2.4) for the transverse states from within the lead, the two block rows are given by

$$-T_{\mathsf{L}}\Big(\chi^{\mathsf{i}}_m + \sum_{m'=1}^{N_p} S_{m'm}\chi^{\mathsf{o}}_{m'} + \sum_{p}^{N_{\mathsf{e}}} \tilde{S}_{pm}\chi^{\mathsf{e}}_p\Big) + T_{\mathsf{LS}}\phi^{\mathsf{S}}_m = 0, \tag{2.5.1}$$

$$T^\dagger_{\mathsf{LS}}\Big(\lambda^{\mathsf{i}}_m\chi^{\mathsf{i}}_m + \sum_{m'=1}^{N_p} S_{m'm}\lambda^{\mathsf{o}}_{m'}\chi^{\mathsf{o}}_{m'} + \sum_{p}^{N_{\mathsf{e}}} \tilde{S}_{pm}\lambda^{\mathsf{e}}_p\chi^{\mathsf{e}}_p\Big) + \big(H_{\mathsf{S}} - E\big)\phi^{\mathsf{S}}_m = 0. \tag{2.5.2}$$

We define for $a \in \{\mathsf{i},\mathsf{o},\mathsf{e}\}$ the matrices which are build up by the eigenvectors and eigenstates of the infinite lead

$$U_a \equiv \big(\chi^a_1,\chi^a_2,\ldots,\chi^a_{N_a}\big), \tag{2.5.3}$$

$$\Lambda_a \equiv \mathrm{diag}\big(\lambda^a_1,\lambda^a_2,\ldots,\lambda^a_{N_a}\big), \tag{2.5.4}$$

and we define the matrix containing the system states corresponding to the different incoming modes

$$\phi_{\mathsf{S}} \equiv \big(\phi^{\mathsf{S}}_1,\phi^{\mathsf{S}}_2,\ldots,\phi^{\mathsf{S}}_{N_{\mathsf{i}}}\big). \tag{2.5.5}$$

Thus, the two equations to solve from the Schrödinger equation are given in block matrix notation by

$$\begin{pmatrix} T_{\mathsf{L}}U_{\mathsf{o}} & T_{\mathsf{L}}U_{\mathsf{e}} & -T_{\mathsf{LS}} \\ T^\dagger_{\mathsf{LS}}U_{\mathsf{o}}\Lambda_{\mathsf{o}} & T^\dagger_{\mathsf{LS}}U_{\mathsf{e}}\Lambda_{\mathsf{e}} & H_{\mathsf{S}} - E \end{pmatrix} \begin{pmatrix} S \\ \tilde{S} \\ \phi_{\mathsf{S}} \end{pmatrix} = \begin{pmatrix} -T_{\mathsf{L}}U_{\mathsf{i}} \\ -T^\dagger_{\mathsf{LS}}U_{\mathsf{i}}\Lambda_{\mathsf{i}} \end{pmatrix}. \tag{2.5.6}$$

In A.1.2, we eliminate $\tilde{S}$ from these equations. To shorten the notation, we introduce new matrices T and K, which essentially are given by the amplitudes to hop from the lead into the system or the next lead site. The K matrices concern only the propagating states and they include contributions of possibly intermediate hoppings into evanescent states. Their explicit form is given as

$$T_{ab} = \Lambda_a^\dagger U_a^\dagger T_{\mathsf{L}} U_b, \qquad a,b \in (\mathsf{o},\mathsf{i},\mathsf{e}), \tag{2.5.7}$$

$$T_{a\mathsf{s}} = \Lambda_a^\dagger U_a^\dagger T_{\mathsf{LS}}, \qquad a \in (\mathsf{o},\mathsf{i},\mathsf{e}), \tag{2.5.8}$$

$$K_{ab} = T_{ab} - T_{a\mathsf{e}} \frac{1}{T_{\mathsf{ee}}} T_{\mathsf{e}b}, \qquad a,b \in (\mathsf{o},\mathsf{i},\mathsf{s}). \tag{2.5.9}$$

The system of equations in terms of K read

$$\begin{pmatrix} K_{\mathsf{oo}} & -K_{\mathsf{os}} \\ -K_{\mathsf{so}} & E - H_{\mathsf{S}} - T_{\mathsf{se}} T_{\mathsf{ee}}^{-1} T_{\mathsf{es}} \end{pmatrix} \begin{pmatrix} S \\ \phi_{\mathsf{S}} \end{pmatrix} = \begin{pmatrix} -K_{\mathsf{oi}} \\ K_{\mathsf{si}} \end{pmatrix}. \tag{2.5.10}$$

This system can now be solved solely for the scattering matrix S by using the block matrix inversion formula

$$\begin{pmatrix} A & B \\ C & D \end{pmatrix}^{-1} = \begin{pmatrix} A^{-1} + A^{-1}B(D-CA^{-1}B)^{-1}CA^{-1} & -A^{-1}B\left(D-CA^{-1}B\right)^{-1} \\ -\left(D-CA^{-1}B\right)^{-1}CA^{-1} & \left(D-CA^{-1}B\right)^{-1} \end{pmatrix}, \tag{2.5.11}$$

which can be applied if one assumes that A and $\left(D-CA^{-1}B\right)$ are invertible. This the generic case and further details on this topic can be found in A.1.6 and A.1.7. The resulting scattering matrix is

$$S_{oi} = -\frac{1}{K_{\mathsf{oo}}} K_{\mathsf{oi}} + \frac{1}{K_{\mathsf{oo}}} K_{\mathsf{os}} \frac{1}{E - H_{\mathsf{S}} - T_{\mathsf{se}} T_{\mathsf{ee}}^{-1} T_{\mathsf{es}} - K_{\mathsf{so}} K_{\mathsf{oo}}^{-1} K_{\mathsf{os}}} \left(K_{\mathsf{si}} - K_{\mathsf{so}} \frac{1}{K_{\mathsf{oo}}} K_{\mathsf{oi}} \right), \tag{2.5.12}$$

which we refer to in the following as S_{oi}. This notation refers to the fact that we generally left the possibility to describe the incoming and outgoing states in two different basis sets. This is discussed in more detail in Sect. 2.6.

In A.1.3 and A.1.4, we analyze the definitions of the K matrices in more detail, and define further helpful identities and formulas, which are used in Sect. 2.6 and are also listed in the glossary. Furthermore, the existence of K_{oo}^{-1} (and K_{ii}^{-1}) is discussed in Appendix A.1.6.

2.6. Mahaux-Weidenmüller Formula

To get a intuitive picture of the scattering matrix formula, we further transform the equation. The derivations of the following basis transform matrix is presented in more detail in Appendix A.1.3 and A.1.4. Here, the matrices containing the transverse eigenstates and eigenvalues of the outgoing and evanescent modes are grouped within the matrices $U_< = \left(U_{\mathsf{o}}, U_{\mathsf{e}}\right)$ and $\Lambda_< = \mathrm{diag}\left(\Lambda_{\mathsf{o}}, \Lambda_{\mathsf{e}}\right)$. By introducing the matrix

$$\Gamma = i\Big(T_{\mathsf{L}}^\dagger U_< \Lambda_< U_<^{-1} - U_<^{-1\,\dagger} \Lambda_<^\dagger U_<^\dagger T_{\mathsf{L}}\Big), \tag{2.6.1}$$

we can define the unitary basis transform matrix

$$C_{\mathsf{io}} = C_{\mathsf{oi}}^{\dagger} = U_{\mathsf{i}}^{\dagger} \Gamma U_{\mathsf{o}}. \tag{2.6.2}$$

We can use the basis transform matrix to change the index of the K matrices as derived in Appendix A.1.4 and listed in the glossary. Using the identities given in (G.29) and (G.34), we can transform the formula for S_{oi} given in Eq. (2.5.12) into

$$S_{\mathsf{oi}} = -U_{\mathsf{o}}^{\dagger} \Gamma U_{\mathsf{i}} + i \frac{1}{K_{\mathsf{oo}}} K_{\mathsf{os}} \frac{1}{E - H_{\mathsf{S}} - T_{\mathsf{se}} T_{\mathsf{ee}}^{-1} T_{\mathsf{es}} - K_{\mathsf{so}} K_{\mathsf{oo}}^{-1} K_{\mathsf{os}}} K_{\mathsf{si}} \frac{1}{K_{\mathsf{ii}}^{\dagger}}. \tag{2.6.3}$$

In general, we are free in the choice as to which basis set we use for the incoming and outgoing leads. We can perform a unitary transformation on the scattering matrix, which does not intermix the leads and only changes the basis set of the modes, and will obtain the same physical results. For example the transmission probability T for scattering from one lead to another is given by the Frobenius norm of the corresponding transmission amplitude t, as stated in Eq. (2.4.15). Transforming the basis of the corresponding incoming and outgoing modes results for the transmission amplitude in the transformation $t \to UtV^{\dagger}$, where U and V represent the unitary matrices for the transformation from one basis set to the other. However, in the evaluation of the transmission probability the unitary matrices cancel within the trace, and therefore we obtain the same result as before the basis set transformation

$$T = \mathsf{tr}\big(UtV^{\dagger} V t^{\dagger} U^{\dagger}\big) = \mathsf{tr}\big(tt^{\dagger}\big). \tag{2.6.4}$$

The change of the basis set of the incoming or outgoing modes into the other is done if we apply the unitary operation C_{io} on S_{io}. Therefore, we define the corresponding scattering matrices

$$S_{\mathsf{oo}} \equiv S_{\mathsf{oi}} C_{\mathsf{io}}, \tag{2.6.5}$$

$$S_{\mathsf{ii}} \equiv C_{\mathsf{io}} S_{\mathsf{oi}}. \tag{2.6.6}$$

The equation for the transformed scattering matrices read

$$S_{\mathsf{oo}} = -\mathbb{1} + i \frac{1}{K_{\mathsf{oo}}} K_{\mathsf{os}} \frac{1}{E - H_{\mathsf{S}} - T_{\mathsf{se}} T_{\mathsf{ee}}^{-1} T_{\mathsf{es}} - K_{\mathsf{so}} K_{\mathsf{oo}}^{-1} K_{\mathsf{os}}} K_{\mathsf{so}} \frac{1}{K_{\mathsf{oo}}^{\dagger}}, \tag{2.6.7}$$

$$S_{\mathsf{ii}} = -\mathbb{1} + i \frac{1}{K_{\mathsf{ii}}} K_{\mathsf{is}} \frac{1}{E - H_{\mathsf{S}} - T_{\mathsf{se}} T_{\mathsf{ee}}^{-1} T_{\mathsf{es}} - K_{\mathsf{si}} K_{\mathsf{ii}}^{\dagger\,-1} K_{\mathsf{is}}} K_{\mathsf{si}} \frac{1}{K_{\mathsf{ii}}^{\dagger}}. \tag{2.6.8}$$

In the following, we discuss the scattering matrix in the form of S_{ii}. Results for the other forms are implied, as they are obtained by unitary transformations. For a simpler notation, we define the matrix

$$W = \frac{1}{\sqrt{2\pi}} \frac{1}{K_{\mathsf{ii}}} K_{\mathsf{is}} \tag{2.6.9}$$

and use the normalization of the propagating modes (G.25) to obtain the identity

$$i\pi W^{\dagger} W = \tfrac{1}{2} K_{\mathsf{si}} \left(\frac{1}{K_{\mathsf{ii}}} - \frac{1}{K_{\mathsf{ii}}^{\dagger}} \right) K_{\mathsf{is}}. \tag{2.6.10}$$

Moreover, we define the Hermitian matrix Δ

$$\Delta = T_{\mathsf{se}} \frac{1}{T_{\mathsf{ee}}} T_{\mathsf{es}} + \tfrac{1}{2} K_{\mathsf{si}} \left(\frac{1}{K_{\mathsf{ii}}} + \frac{1}{K_{\mathsf{ii}}^\dagger} \right) K_{\mathsf{is}}. \tag{2.6.11}$$

The objects in the parentheses of the right side of the equations for Δ and $W^\dagger W$ can be interpreted essentially by the real and imaginary part of K_{ii}^{-1} as denoted in the glossary by (G.16) and (G.17). With the defined matrices, we can write our formula for the scattering matrix, which is given in Eq. (2.6.8), as

$$S_{\mathsf{ii}} = -\mathbb{1} + i2\pi W \frac{1}{E - H_{\mathsf{S}} - \Delta + i\pi W^\dagger W} W^\dagger, \tag{2.6.12}$$

We can define an effective Hamiltonian to incorporate Δ, which has the effect that it shifts the energy levels of the Hamiltonian

$$H_{\mathsf{eff}} = H_{\mathsf{S}} + \Delta. \tag{2.6.13}$$

Now this equation can be compared to a popular formula of nuclear physics, which associates the Hamiltonian H of a system and its coupling W to the environment with the corresponding scattering matrix. This formula is named after Weidenmüller and Mahaux[3] and reads

$$S = \mathbb{1} - 2\pi i W \frac{1}{E - H + i\pi W^\dagger W} W^\dagger. \tag{2.6.14}$$

We can directly see the equivalent form of Eq. (2.6.12) to the Weidenmüller formula (2.6.14) for the effective Hamiltonian. The results differ by a global phase factor of minus one, which comes from our definition of the scattering matrix. The factor becomes intuitively clear when one imagines having a system, where the incoming and outgoing modes are given in the same basis set, and then asks which value the scattering matrix should have if one sets the coupling from the leads to the system to zero. For the system site, the wave function vanishes in this case, the only remaining equation to solve for the Schrödinger equation is thus given by Eq. (2.5.1), and reads with sum convention $\chi_m + S_{m'm}\chi_{m'} + \tilde{S}_{pm}\chi_p^{\mathsf{e}} = 0$. The solution to this equation is then simply given by $\tilde{S} = 0$ and as already stated $S = -\mathbb{1}$.

To get an intuition to the Weidenmüller formula, we evaluate it for simple leads. With simple leads, we mean leads where the unit cells H_{L} and the hopping in between T_{L} are diagonal. Furthermore the energy in the leads is fixed at a level where all modes are propagating. By looking at the quadratic eigenvalue equation, which determines the lead states and is given in Eq. (2.2.5), we see that this can be achieved by $H_{\mathsf{L}} = 0$ and evaluating the leads at $E = 0$. In the simplest case, we set the hopping in between the lead sites for every mode to $T_{\mathsf{L}} = -t\mathbb{1}$. The calculations are performed in Appendix A.1.8, where we find as resulting scattering matrix

$$S = -\mathbb{1} + i2\frac{1}{t} T_{\mathsf{LS}} \frac{1}{E - H_{\mathsf{S}} + (i/t) T_{\mathsf{LS}}^\dagger T_{\mathsf{LS}}} T_{\mathsf{LS}}^\dagger, \tag{2.6.15}$$

[3] Hans-Arwed Weidenmüller and Claude Mahaux derive the formula in a different manner in their book *Shell-model approach to nuclear reactions*.

note that even though we set $E = 0$ in the lead, we still allow the energy to vary within the system. The local density of states for the simple leads is evaluated in the Appendix A.1.8 to

$$d\big(E = 0\big) = \frac{1}{\pi t}. \tag{2.6.16}$$

Therefore, one way to write the Weidenmüller formula for a system with simple leads is given by

$$S = -\mathbb{1} + i2\pi d\big(0\big) T_{\mathsf{LS}} \frac{1}{E - H_{\mathsf{S}} + i\pi d\big(0\big) T_{\mathsf{LS}}^{\dagger} T_{\mathsf{LS}}} T_{\mathsf{LS}}^{\dagger}. \tag{2.6.17}$$

Therefore, the Weidenmüller formula (2.6.14) is obtained up to a global phase for the Hamiltonian $H = H_{\mathsf{S}}$ and the coupling $W = T_{\mathsf{LS}}$, when one assumes that the leads have a local density of states of $d\big(0\big) = 1$. Our presented derivation allows on the other hand explicitly to see how leads with a more complicated mode structure play into the scattering matrix.

2.7. Conductance

Once the scattering matrix is calculated, we can use the Landauer-Büttiker formulism to calculate the conductance of the system. Here, we assume that every lead i is connected to a respective reservoir, which lies at a chemical potential that could be set due to a voltage potential $\mu_i = eV_i$. Furthermore, there should be no coherence between the different reservoirs in the Landauer formulation, which is explained in more detail in [4].

To calculate the current, we can use the Büttiker formula [14]. In general, it states that the current in lead i is given by

$$I_i = \frac{e}{h} \int \mathrm{d}E \bigg[\big(N_i - R_i\big) f_i - \sum_{j \neq i} T_{ij} f_j \bigg]. \tag{2.7.1}$$

This means, we count for all energies the number of incoming propagating modes in the lead N_i, and weight them by their respective distribution function f_i, where in this case f_i are the Fermi distribution functions for the electrons in reservoir i,

$$f_i = \frac{1}{\exp[(E - \mu_i)/kT_i] + 1}, \tag{2.7.2}$$

which at zero temperature $T_i = 0$ assumes the simple form $f_i = \Theta(\mu_i - E)$. And furthermore, we subtract with the appropriate weight the modes which run into the other directions, either because they got reflected $R_i f_i$, or because they got transmitted into the lead from another lead $T_{ij} f_j$.

We introduced N_i, R_i and T_{ij} already in Sect. 2.4. Using the symmetry relation in the probabilities, which were stated in Eq. (2.4.18), the Büttiker formula is transformed to

$$I_i = \frac{e}{h} \int \mathrm{d}E \sum_j T_{ij} \big(f_i - f_j\big), \tag{2.7.3}$$

where we let the sum run over all indices, as the distribution functions cancel anyway in the case of $j = i$. In general, N_i, R_i and T_{ij} might depend on the energy. We are interested however only in the linear response regime, considering only a small bias $\Delta\mu = \mu_j - \mu_i \ll E_c$, where E_c is an energy range with a nearly constant transmission function T_{ij}, see [4] for more details. Then, the Büttiker formula can once again be simplified as for small $\Delta\mu$, we obtain $f_i - f_j \approx -e(V_i - V_j)\mathrm{d}f_i/\mathrm{d}E$, where the last factor is at zero temperature simply the negative Dirac delta distribution $\mathrm{d}f_i/\mathrm{d}E = -\delta(E - \mu)$. Moreover, we can use the Landauer relation

$$G_{ij} = \frac{e^2}{h} T_{ij}, \tag{2.7.4}$$

where the constant prefactor is called the conductance quantum. Often, an additional factor of two or more is included at this point to account for the spin or valley degeneracy of the system, which possibly was not included in the calculation of the transmission probability. For a simple intuitive derivation of the Landauer relation, we advice to take a look to Ref. [15, 4]. In the linear response regime, the Büttiker formula reads

$$I_i = \sum_j G_{ij}(V_i - V_j). \tag{2.7.5}$$

Having used the property of the transmission probability (2.4.18), obtained from the unitarity of the scattering matrix, the Büttiker formula (2.7.1) assumes a gauge invariant form, seen in Eq. (2.7.3) and Eq. (2.7.5). This means, it is invariant under the transformation $V_i \to V_i + V_0$ for all voltages, and the current depends only on the difference of the voltages in the different reservoirs. Furthermore, as we used in Sect. 2.3 the current conservation to deduce the unitarity of the scattering matrix, we can rediscover the conservation easily in the transformed Büttiker formulas. To check this relation, we can use the symmetry in the transmission probabilities (2.4.18), which for the case of Eq. (2.7.5) can also be written in terms of the conductance by using the Landauer formula (2.7.4) as $\sum_j G_{ij} = \sum_j G_{ji}$. If we calculate the sum over all currents given by (2.7.3), we can use the symmetry in the first summand, and switch the names of the indices in the second summand, and obtain as a result

$$\sum_i I_i = \frac{e}{h} \int \mathrm{d}E \left(\sum_{ij} T_{ji} f_i - \sum_{ij} T_{ji} f_i \right) = 0. \tag{2.7.6}$$

For an experiment in a two-terminal setup, where a current I is driven from the left lead to the right lead, which have a voltage difference of $V = V_2 - V_1$, the Landauer formula (2.7.4) gives the measured conductance $G = I/U$ directly from the scattering matrix.

On the other hand, we often consider in experiments the case of a multiterminal setup. In the four-terminal setup of Fig. 2.6, a current I is driven for example through lead one and two, and the voltage drop is measured over the leads three and four. In this manner, the contact resistance is eliminated from the conductance measurement of the system. Using the Landauer formula (2.7.4), we obtain the elements G_{ij} of the conductance matrix. We can apply the Büttiker formula (2.7.5) to calculate the current in the leads i. From this, we get a linear system of equations for our four-terminal system connecting the potentials V_i to

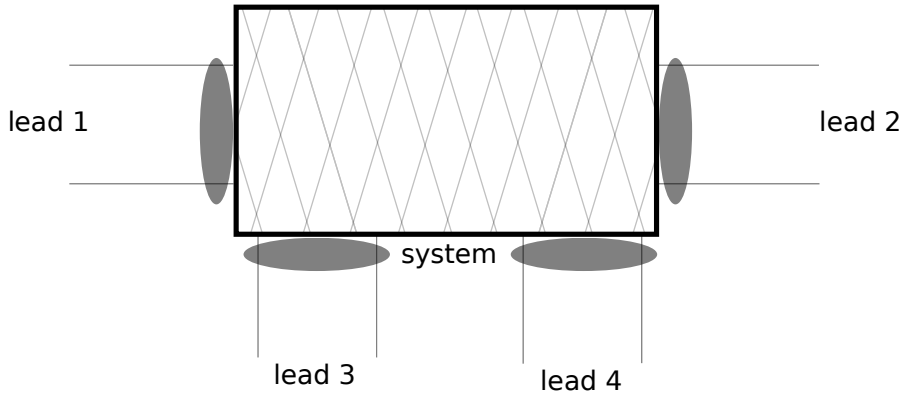

Figure 2.6.: In experiments, we often consider a four-terminal setup. The current is driven through two leads, where the voltage is measured over the other two respective leads. By this technique, the contact resistance, hinted by the grey ellipsoids, is eliminated from the measurement.

the currents I_i. We can make use of the current conservation and the gauge freedom in the potential. With this, the system of equations can be simplified by setting for example $V_4 = 0$, as only the differences in the voltages are important, and calculate the corresponding current from $I_4 = -I_1 - I_2 - I_3$. Then, there only remains to solve

$$\begin{pmatrix} I_1 \\ I_2 \\ I_3 \end{pmatrix} = \begin{pmatrix} G_{12}+G_{13}+G_{14} & -G_{12} & -G_{13} \\ -G_{21} & G_{21}+G_{23}+G_{24} & -G_{23} \\ -G_{31} & -G_{32} & G_{31}+G_{32}+G_{34} \end{pmatrix} \begin{pmatrix} V_1 \\ V_2 \\ V_3 \end{pmatrix}. \tag{2.7.7}$$

Here, we still have to apply the condition on the system, that the current is only being driven through lead one and two, therefore $I_1 = -I_2 = I$. As we measure the voltage drop over lead 3 and lead 4, the resulting resistance is given by

$$R_{4t} = \left.\frac{V_3}{I}\right|_{V_4=0}. \tag{2.7.8}$$

The voltage V_3 is obtained from solving the system of equations (2.7.7) and can for example be found in [16].

Furthermore, when we are given a four-terminal system, we can also ask the question what the current would be if the system setup would also allow for a two-terminal treatment. This can for example be the case if lead one and three can be treated as a single effective lead, as well as lead two and four. In practice, this means G_{13}, G_{31}, G_{24} and G_{42} will be much greater than the other conductance values. Treating the remaining conductance values as small quantities, we obtain in leading order for the inverse of the four-terminal resistance of Eq. (2.7.8)

$$R_{4t}^{-1}\big|_{\text{2t limit}} = G_{12} + G_{14} + \Big(G_{32} + G_{34}\Big)\frac{G_{13}}{G_{31}}. \tag{2.7.9}$$

The last fraction equals to one for zero magnetic field, as in this case we find the symmetry $G_{ij} = G_{ji}$, which is explained in [4]. Therefore, the result is just given in this limit by the sum of the separate conductance values of one lead to the respective leads of the other group.

2.8. Fisher-Lee Relation

In the appendix of [9], the Fisher-Lee relation, which connects the non-equilibrium Green's function formalism (NEGF) to the scattering theory, is derived as

$$S_{mn} = \frac{1}{\sqrt{|j_{m,<}|\,|j_{n,>}|}}\Big(-\phi^{\dagger}_{m,<}\Gamma\phi_{n,>} + i\phi^{\dagger}_{m,<}\Gamma G^{r}_{\mathsf{S}}\Gamma\phi_{n,>}\Big). \tag{2.8.1}$$

Here, the scattering matrix, given by this formula, describes a system with one effective lead, where a unit cell of the lead was added to the system, and thus $T_{\mathsf{LS}} = T_{\mathsf{L}}$. The states with subscript $<$ denotes outgoing propagating states and $>$ refers to incoming states. The Γ matrix is defined in the same manner, as we did in Appendix A.1.3. The object G^{r}_{S} is the retarded Green's function of the system, which is given in [9] by

$$G^{r}_{\mathsf{S}} = \frac{1}{E - H_{\mathsf{S}} - T^{\dagger}_{\mathsf{LS}} g_{\mathsf{L}} T_{\mathsf{LS}}}, \tag{2.8.2}$$

where g_L is the retarded surface Green's function of the lead, which can be calculated according to [9] from

$$g_{\mathsf{L}} T_{\mathsf{L}} = U_{<}\Lambda_{<}U_{<}^{-1}. \tag{2.8.3}$$

With all the tools in hand, we can show that our derived formula for the scattering matrix is equivalent to the Fisher-Lee relation. For this purpose, we rewrite the Fisher-Lee relation into our matrix notation, and use our normalization of the modes to obtain

$$S = -U^{\dagger}_{\mathsf{o}}\Gamma U_{\mathsf{i}} + iU^{\dagger}_{\mathsf{o}}\Gamma G^{r}_{\mathsf{S}}\Gamma U_{\mathsf{i}}. \tag{2.8.4}$$

We can directly compare this to our derived formula given in Eq. (2.6.3), which read

$$S_{\mathsf{oi}} = -U^{\dagger}_{\mathsf{o}}\Gamma U_{\mathsf{i}} + i\frac{1}{K_{\mathsf{oo}}}K_{\mathsf{os}}\frac{1}{E - H_{\mathsf{S}} - T_{\mathsf{se}}T^{-1}_{\mathsf{ee}}T_{\mathsf{es}} - K_{\mathsf{so}}K^{-1}_{\mathsf{oo}}K_{\mathsf{os}}}K_{\mathsf{si}}\frac{1}{K^{\dagger}_{\mathsf{ii}}}. \tag{2.8.5}$$

The augend of the sum is obviously the same. For the addend, we have to show first the equivalence of the large inverse term in the center to the retarded Green's function of the system and thus

$$T_{\mathsf{se}}\frac{1}{T_{\mathsf{ee}}}T_{\mathsf{es}} + K_{\mathsf{so}}\frac{1}{K_{\mathsf{oo}}}K_{\mathsf{os}} = T^{\dagger}_{\mathsf{LS}} g_{\mathsf{L}} T_{\mathsf{LS}}. \tag{2.8.6}$$

We introduce therefore the inverse of the matrix build by the outgoing and evanescent modes (see A.1.3 for more details)

$$U_{<}^{-1} = \begin{pmatrix} \Upsilon^{\dagger}_{\mathsf{o}} \\ \Upsilon^{\dagger}_{\mathsf{e}} \end{pmatrix} \tag{2.8.7}$$

and can therefore write

$$g_{\mathsf{L}} T_{\mathsf{L}} = U_{<} \Lambda_{<} U_{<}^{-1} = U_{\mathsf{o}} \Lambda_{\mathsf{o}} \Upsilon_{\mathsf{o}}^{\dagger} + U_{\mathsf{e}} \Lambda_{\mathsf{e}} \Upsilon_{\mathsf{e}}^{\dagger}. \tag{2.8.8}$$

Splitting off the terms without T_{LS} and $T_{\mathsf{LS}}^{\dagger}$, we can define a matrix R, which fulfills

$$T_{\mathsf{LS}}^{\dagger} R T_{\mathsf{LS}} = T_{\mathsf{se}} \frac{1}{T_{\mathsf{ee}}} T_{\mathsf{es}} + K_{\mathsf{so}} \frac{1}{K_{\mathsf{oo}}} K_{\mathsf{os}}. \tag{2.8.9}$$

By a straight forward calculation that involves the insertion of $\mathbb{1} = \Upsilon_{\mathsf{o}} \Upsilon_{\mathsf{o}}^{\dagger} + \Upsilon_{\mathsf{e}} \Upsilon_{\mathsf{e}}^{\dagger}$ into the definition of R, we can see that $R T_{\mathsf{L}} = g_{\mathsf{L}} T_{\mathsf{L}}$. Incorporating a lead site into the system, we have $T_{\mathsf{LS}} = T_{\mathsf{L}}$ also in our formalism, and can conclude Eq. (2.8.6) is fulfilled.

In the same manner, we can derive by a straight forward calculation

$$\frac{1}{K_{\mathsf{oo}}} K_{\mathsf{os}} = i U_{\mathsf{o}}^{\dagger} T_{\mathsf{L}}^{\dagger} \Big(g_{\mathsf{L}}^{\dagger} - g_{\mathsf{L}} \Big) T_{\mathsf{LS}}, \tag{2.8.10}$$

and

$$K_{\mathsf{si}} \frac{1}{K_{\mathsf{ii}}^{\dagger}} = i T_{\mathsf{LS}}^{\dagger} \Big(g_{\mathsf{L}} - g_{\mathsf{L}}^{\dagger} \Big) T_{\mathsf{L}} U_{\mathsf{i}}. \tag{2.8.11}$$

Comparing with Eq. (A.1.33), which states that

$$\Gamma = i T_{\mathsf{L}}^{\dagger} \Big(g_{\mathsf{L}} - g_{\mathsf{L}}^{\dagger} \Big) T_{\mathsf{L}}, \tag{2.8.12}$$

we see the equivalence of our derived Weidenmüller formula to the Fisher-Lee relation. Therefore, the derived Weidenmüller formula for S_{io} is equivalent to the result from the NEGF formalism. This way, we can always choose the method of preference and will yield equivalent results. For the NEGF formalism, we find in [9] an algorithm for the calculation of the Green's function of the lead, which avoids the explicit calculation of the evanescent eigenvectors, and is therefore more stable in some cases. By this means, the scattering matrix can thus also be calculated after having calculated the Green's function of the lead via the formula

$$S_{\mathsf{oi}} = -C_{\mathsf{oi}} - i U_{\mathsf{o}}^{\dagger} T_{\mathsf{L}}^{\dagger} \Big(g_{\mathsf{L}} - g_{\mathsf{L}}^{\dagger} \Big) T_{\mathsf{LS}} \frac{1}{E - H_{\mathsf{S}} - T_{\mathsf{LS}}^{\dagger} g_{\mathsf{L}} T_{\mathsf{LS}}} T_{\mathsf{LS}}^{\dagger} \Big(g_{\mathsf{L}} - g_{\mathsf{L}}^{\dagger} \Big) T_{\mathsf{L}} U_{\mathsf{i}}. \tag{2.8.13}$$

2.9. Density of States

The density of states (DOS) $D(E)$ is a fundamental quantity. We can measure the number of states in the interval $[E, E + dE]$ by evaluating $D(E)dE$. To calculate the DOS for a system that is described by the Hamiltonian H, we consider the total number of states with an energy lower than E

$$N(E) = \sum_{n} \Theta(E - E_n), \tag{2.9.1}$$

where E_n are the eigenstates of the Hamiltonian. The DOS is consequentially the derivative of this quantity [17]

$$D(E) = \sum_{n} \delta(E - E_n). \tag{2.9.2}$$

In our open system setup, this quantity typically diverges. Therefore, it makes sense to only discuss the local density of states $d(\boldsymbol{r}, E)$ (LDOS), which is defined to extract only the information of the system at a certain spatial point. This is especially convenient for the open systems, to analyze only the finite-sized scattering region. It is defined [4] as

$$d(\boldsymbol{r}, E) = \sum_n \left|\phi_n(\boldsymbol{r})\right|^2 \delta(E - E_n), \tag{2.9.3}$$

where ϕ_n are the corresponding eigenfunctions of the system. By definition, the DOS is given by integrating the LDOS over the whole space. To calculate the LDOS at a point of the finite-sized system, we return to the system of equations (2.5.10). Instead of solving it for the scattering matrix, we solve it for the system states by

$$\phi_{\mathsf{S}} = i \frac{1}{E - H_{\mathsf{S}} - \Delta + i\pi W^\dagger W} K_{\mathsf{si}} \frac{1}{K_{\mathsf{ii}}^\dagger}. \tag{2.9.4}$$

The columns of the resulting matrix ϕ_{S} correspond to the system states associated to the different modes of the asymptotic lead states and evaluated at the specified energy. From this the LDOS at the corresponding lattice site can be calculated by Eq. (2.9.3).

Another way to calculate the DOS can be achieved by using the definition of the retarded Green's function in energy representation

$$G_0^R = \frac{1}{E - H + i0^+}. \tag{2.9.5}$$

Using the Sokhotski-Plemelj theorem

$$\frac{1}{x \pm i0^+} = \mathcal{P}\left(\frac{1}{x}\right) \mp i\pi\delta(x), \tag{2.9.6}$$

we have

$$\mathsf{Im}(G_0^R) = -\pi\delta(E - H), \tag{2.9.7}$$

and can thus write the density of states as

$$D(E) = -\frac{1}{\pi} \mathsf{tr}\Big(\mathsf{Im}\, G_0^R\Big). \tag{2.9.8}$$

The total local density of states can be calculated from the system Green's function, which was introduced in Sect. 2.8 as

$$G_{\mathsf{S}}^R = \frac{1}{E - H_{\mathsf{S}} - \Delta + i\pi W^\dagger W}, \tag{2.9.9}$$

and is given by

$$d(E) = -\frac{1}{\pi} \mathsf{tr}\Big(\mathsf{Im}\, G_{\mathsf{S}}^R\Big). \tag{2.9.10}$$

The leads contribute to the LDOS via the self-energy of the systems Green's function. As we will see in the following, it is important that the energy within the leads is fixed and therefore

Δ and W are independent of E. The space resoluted LDOS is obtained from this formula if one does not take the trace of the imaginary part of the Green's function, but associates every point on the diagonal of the matrix, with the respective lattice site.

To see the connection between the calculated LDOS from the Green's function and the scattering matrix, we use the Wigner-Smith Matrix [18]

$$Q = \frac{1}{2\pi i}\frac{\mathrm{d}}{\mathrm{d}E}\log S = \frac{1}{2\pi i}S^\dagger\frac{\mathrm{d}S}{\mathrm{d}E}. \tag{2.9.11}$$

We can show that the trace of this matrix gives $d(E)$ by using the Weidenmüller formula for the case that W and Δ are independent of E. Meaning, we fix the energy within the leads but allow for variation within the system. In the following, we abbreviate $G \equiv G_S^R$ for a shorter notation. From Eq. (2.6.12), we find that

$$\operatorname{tr} Q = \operatorname{tr}\Big(WG^2W^\dagger + 2i\pi WG^\dagger W^\dagger WG^2W^\dagger\Big) \tag{2.9.12}$$

$$= \operatorname{tr}\Big[\Big(G + 2i\pi G^\dagger W^\dagger WG\Big)GW^\dagger W\Big] \tag{2.9.13}$$

We can use the equations,

$$2i\pi G^\dagger W^\dagger WG = G^\dagger - G, \tag{2.9.14}$$

$$2i\pi GW^\dagger WG^\dagger = G^\dagger - G, \tag{2.9.15}$$

$$\tag{2.9.16}$$

which were obtained by considering that the systems Green's function is given with the form $G = 1/(A - iB)$, where $A = E - H_S - \Delta$ and $B = \pi W^\dagger W$, where A and B are Hermitian. We can easily see that the difference with the complex conjugate can be written after inserting a matrix of unity as

$$G^\dagger - G = \frac{1}{A+iB}(A+iB)\frac{1}{A-iB} - \frac{1}{A+iB}(A-iB)\frac{1}{A-iB}, \tag{2.9.17}$$

or with the terms in fraction the other way around. This results in the two mentioned equations, which can be plugged into $\operatorname{tr} Q$. Using the invariance of the trace under cyclic permutations, we obtain for

$$\operatorname{tr} Q = \operatorname{tr}\frac{1}{2\pi i}\Big(G^\dagger - G\Big) \tag{2.9.18}$$

$$= -\frac{1}{\pi}\operatorname{tr}\operatorname{Im} G. \tag{2.9.19}$$

Thus, we can follow the assertion

$$d\big(E\big) = \operatorname{tr} Q, \tag{2.9.20}$$

and have yet another way to evaluate the LDOS. In practical implementations this method is less preferable, as it demands either a matrix logarithm or the derivative of the scattering matrix for the evaluation of Q. However, for theoretical discussions it can be useful, as shown in the next section.

2.10. DOS when Including Part of the Lead

In the definition of the scattering problem, we numbered the sites. We set on site number zero the system, on site number one the first lead unit cell, on site number two the second lead unit cell, and so on (cf. (2.1.12)). We could also have said that position zero is another lead site and the system just starts at position -1, which is equivalent to incorporating one lead site into the system definition. In the evaluation of the total LDOS of the system from the scattering matrix, we fixed the energy within the lead, and allowed only for a variation of the energy within the system. We could ask ourselves, how does the total LDOS change now that one site of the lead is added to the system, and therefore allowed to vary in energy?

For this purpose, we ask in a first step, what the corresponding scattering matrix is if the lead is shifted by one site. Performing the same mathematical steps, as in the beginning of Sect. 2.1, with just a different numbering of the sites yields the scattering matrix $\bar{S}$, which is connected to the result with standard numbering by

$$\bar{S} = \Lambda_{\mathsf{o}}^{\dagger} S \Lambda_{\mathsf{i}}. \tag{2.10.1}$$

If we do not allow the incorporated site to vary in energy, meaning the Λ are independent of E, this transformation does not change anything in the density of states. As the shifted total LDOS is given by

$$\bar{d}\big(E\big) = \frac{1}{2\pi i}\,\mathsf{tr}\bigg(\frac{1}{\Lambda_{\mathsf{o}}^{\dagger} S \Lambda_{\mathsf{i}}} \Lambda_{\mathsf{o}}^{\dagger} \frac{\mathrm{d}S}{\mathrm{d}E} \Lambda_{\mathsf{i}}\bigg), \tag{2.10.2}$$

and using $\big(\Lambda_{\mathsf{o}}^{\dagger} S \Lambda_{\mathsf{i}}\big)^{-1} = \Lambda_{\mathsf{i}}^{\dagger} S^{\dagger} \Lambda_{\mathsf{o}}$, as well as the invariance of the trace under cyclic permutation, we find

$$\bar{d}\big(E\big) = \frac{1}{2\pi i}\,\mathsf{tr}\bigg(S^{\dagger} \frac{\mathrm{d}S}{\mathrm{d}E}\bigg), \tag{2.10.3}$$

which is exactly the result, which we obtain for the total LDOS $d\big(E\big)$ in Sect. 2.9 without shifting the numbering.

On the other hand, if we allow for a variation of the energy within the incorporated lead site, the density of states will get a contribution from the additional site. In this case

$$\frac{\mathrm{d}\bar{S}}{\mathrm{d}E} = \frac{\mathrm{d}\Lambda_{\mathsf{o}}^{\dagger}}{\mathrm{d}E} S \Lambda_{\mathsf{i}} + \Lambda_{\mathsf{o}}^{\dagger} \frac{\mathrm{d}S}{\mathrm{d}E} \Lambda_{\mathsf{i}} + \Lambda_{\mathsf{o}}^{\dagger} S \frac{\mathrm{d}\Lambda_{\mathsf{i}}}{\mathrm{d}E}. \tag{2.10.4}$$

Using additionally $\Lambda_{\mathsf{o}}^{\dagger} = \Lambda_{\mathsf{i}}$, which is the case if incoming and outgoing states are given in the same basis, we obtain

$$\bar{d}\big(E\big) = \frac{1}{2\pi i}\,\mathsf{tr}\bigg(S^{\dagger} \frac{\mathrm{d}S}{\mathrm{d}E} + 2\frac{\mathrm{d}\log\Lambda_{\mathsf{i}}}{\mathrm{d}E}\bigg). \tag{2.10.5}$$

Using the form of the propagating eigenvalues $\lambda = \exp\big(ik\big)$, and the diagonal structure of Λ this can be written as

$$\bar{d}\big(E\big) = d\big(E\big) + \sum_m \frac{1}{\pi}\frac{\mathrm{d}k_m}{\mathrm{d}E}. \tag{2.10.6}$$

The result can be understood by considering that the one dimensional density of states of the propagating states in the leads is given by $g\big(E\big) = \big(1/2\pi\big)dk/dE$. We see that for $2N_p$ propagating modes, as we have N_p incoming modes and N_p outgoing modes, the additional term adds to $d\big(E\big)$ the density of states from the incorporated site of the lead

$$\bar{d}\big(E\big) = d\big(E\big) + 2N_p g\big(E\big), \tag{2.10.7}$$

The result of Eq. (2.10.6) can be associated to Friedel's theorem, which can for example be found in the fourth chapter of Ref. [19], and can be expressed as

$$\frac{\mathrm{d}n}{\mathrm{d}E} = \rho_0 + \frac{1}{\pi}\frac{\mathrm{d}\delta}{\mathrm{d}E}. \tag{2.10.8}$$

Friedel's theorem states that if an impurity is added to a system, the number of states $\mathrm{d}n$ in the interval $\big[E, E + \mathrm{d}E\big]$ is given by the number of states in the interval for the system without the impurity $\rho_0 \mathrm{d}E$, and is added by the the phase shift $\mathrm{d}\delta$ in this interval due to the impurity scattering in terms of π. This can be understood intuitively from the picture of a particle in a one-dimensional box. Here, the mode is characterized by the number of antinodes, where every antinode corresponds to a phase of π. In our case, we add a site to the system, where from every propagating mode a shift of k_m is contributed.

3. Gallium Arsenide

A lot of effort in the recent investigations of two-dimensional mesoscopic conductors has been based on GaAs-AlGaAs heterojunctions [4, 20]. Due to the conduction band offset of the two semiconductors, a potential well is formed at the interface as depicted Fig. 3.1. This confines the low-energy electrons of the conduction band to the interface, where the electrons form a free two-dimensional electron gas (2DEG). The confinement results in two-dimensional subbands. For low temperatures and low carrier densities only the lowest subband is occupied and the motion of an electron along the interface of the heterojunction can be described by an effective mass Schrödinger equation

$$\left[\frac{\big(\boldsymbol{p}+e\boldsymbol{A}\big(x,y\big)\big)^2}{2m}+V\big(x,y\big)\right]\Psi\big(x,y\big)=(E-E_{\mathsf{S}})\Psi\big(x,y\big). \tag{3.0.1}$$

Here, the energy of the lowest occupied subband is denoted by E_{S}, the potential energy by $V\big(x,y\big)$, the vector potential by $\boldsymbol{A}\big(x,y\big)$, and the effective mass by m, which is $m\approx 0.067m_e$ for GaAs. The dispersion relation of a free two-dimensional electron gas $\big(\boldsymbol{A}=0,V=0\big)$ is thus given by

$$E\big(k\big)=E_{\mathsf{S}}+\frac{\hbar^2k^2}{2m}, \tag{3.0.2}$$

where $k=\big(k_x^2+k_y^2\big)^{1/2}$. To simulate the transport of electrons in an arbitrary potential landscape, we discretize the continuous Schrödinger equation on a square lattice like shown in the Appendix A.2. Then, we demonstrate how disorder is simulated and compare the result with the expectation from Born approximation in Sect. 3.2.1. Following, the vector potential associated with a magnetic field can be incorporated on the links of the resulting tight binding model like shown in A.3 and done in Sect. 3.3. This chapter is intended to explicitly show how the previous points can be implemented in a fairly simple model, such as the one for GaAs. The same methods will then be used and translated to a graphene model, in the following chapter to study questions of recent interest.

3.1. Dispersion Relation for System of Finite Width

For the simulation of the electron transport in the GaAs heterojunction, we set up a tight binding model on a square lattice. We use the Python package kwant [8], which enables us to quickly design a tight binding model in any geometry we want, and additionally can solve directly for the scattering matrix. As a preliminary work, we check simple system setups. Naturally, the lattice constant of the square lattice is set to $a=1$ in the simulation. Any physical length scale of interest for the system should be considerably larger in the simulation

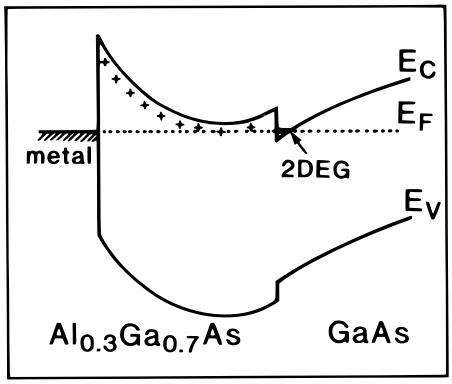

Figure 3.1.: Band bending diagram of GaAs-AlGaAs heterostructure [20]. The electrons are confined for low energies at the interface of the two materials. Therefore the dimensionality is reduced and they are only free to move in the remaining two dimensions.

than the length scale set by the lattice constant. The hopping parameter on the lattice is set to $t = 1$, which sets the energy scale.

Consider for the simplest case a clean infinite lead of finite width W. The continuum Hamiltonian would be given by

$$H = \frac{p_x^2}{2m} + \frac{p_y^2}{2m}, \tag{3.1.1}$$

with the boundary conditions that the wavefunction vanishes at $y = 0$ and $y = W$. In the numerical simulation the lattice structure is taken as shown in Fig. 3.2.

The onsite terms are set to the number of nearest neighbors for each lattice site. First, we check the dispersion relation by evaluating the phase k of the propagating modes for different energies. For an infinite tight binding system on a two timensional square lattice, we would expect (see for example Ref. [17])

$$E = 4t - 2t\cos\big(k_x a\big) - 2t\cos\big(k_y a\big). \tag{3.1.2}$$

From this expectation, we already see that the results of the tight binding model only agrees with the continuum model for low energy modes, where the cosine is approximately parabolic. Furthermore due to the lateral confinement, the motion is only free in the x-direction. The confinement quantizes the transverse momentum to $k_y = n\pi/W$ and the 2-dimensional band is split into 1-dimensional subbands with band bottoms E_n $\big(n = 0,1,2,\ldots,W-1\big)$ at

$$E_n = \frac{\pi^2 t a^2}{W^2} n^2. \tag{3.1.3}$$

This quantization is the reason why one observes a step-wise increase in the conductance for quantum point contacts of small width. The number of transmitting channels for such a constrained system at Fermi energy E_F is given by

$$N = 1 + \left\lfloor \frac{W\sqrt{E_\mathsf{F}}}{\pi a\sqrt{t}} \right\rfloor. \tag{3.1.4}$$

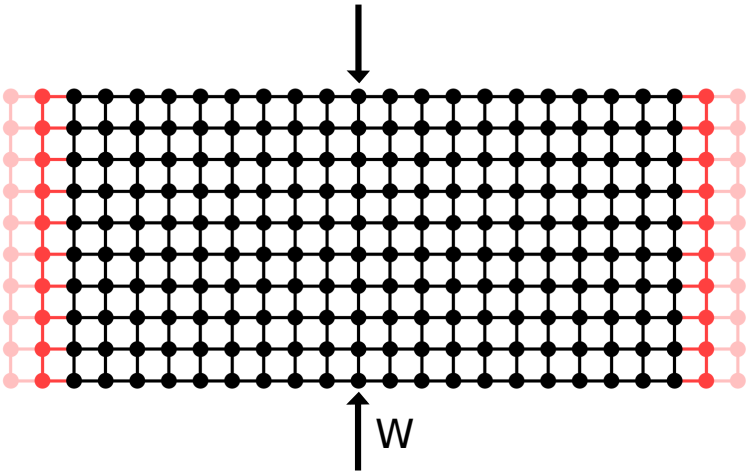

Figure 3.2.: Square lattice structure used for the simulation of the lead. The lead extends infinitely in horizontal x-direction and we choose to simulate 100 lattice sites in the transverse y-direction (i.e. $W = 100a$). The onsite terms are set to the number of nearest neighbors and the hopping is set to $t = -1$.

The upper panel of Fig. 3.3 shows the simulated dispersion relation of the lead. It is obtained by evaluating Eq. (2.2.4), where the eigenvalues E are calculated for the propagating modes $\lambda^{\mathsf{P}} = \exp(ik_x a)$. A single slice of the lattice structure is used as unit cell for the infinite lead. If we zoom to the low energy levels, the $n-th$ mode appears if the energy is greater than E_n. The modes follow for low energy values the parabolic form of the continuum limit

$$E = E_n + ta^2 k_x^2, \tag{3.1.5}$$

which can be seen in the lower panel of Fig. 3.3. It is important to note here that we choose as constant onsite terms the number of nearest neighbors. Therefore, we are giving the edge sites an onsite value of $\epsilon_n = 3$ and not $\epsilon_n = 4$, like the simple discretization scheme of Sect. A.2 would suggest. For large system sizes both discretizations of the derivative should converge to the same result, but with our limited resources this little difference would for example open up a small gap between zero energy and the lowest mode. This is avoided in the presented discretization scheme here.

Now, we see from the previous plots that the model gives, as expected, only for the low energy values a good description of the continuum model. As a next step we should ask, what is the parameter regime we need to simulate, such that we can be sure our model gives appropriate results.

Clearly for the parabolic dispersion relation this is only given in the low energy limit, therefore demanding the condition

$$E \ll t. \tag{3.1.6}$$

Furthermore we can think about the number of modes within this limit. The wavelength from the n-th mode should be much greater than the lattice constant to ensure that it is

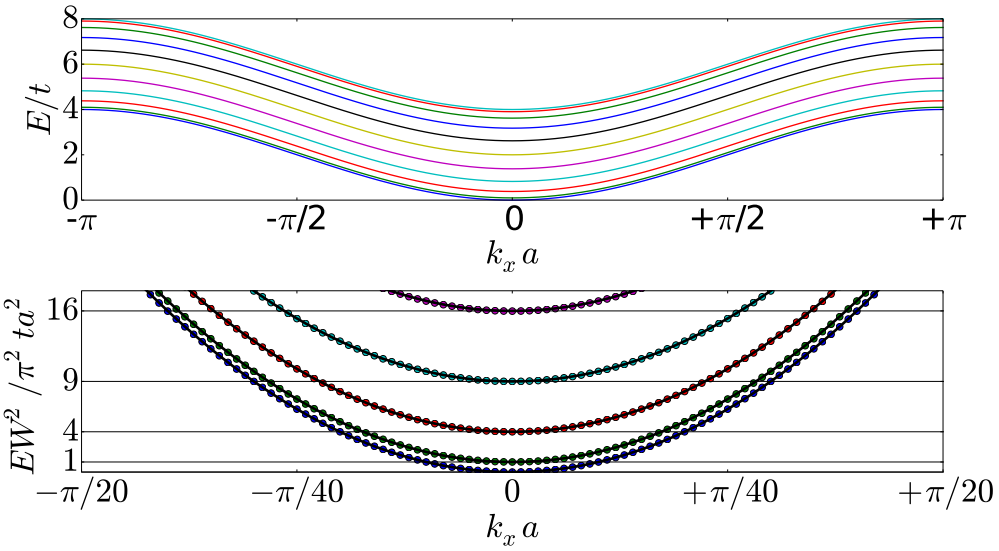

Figure 3.3.: The upper panel shows the first Brillouin zone of the square lattice dispersion relation for an infinite lead of finite width $W = 100a$. The plot shows every 10$^{\text{th}}$ mode of the 100 modes, which follow a cosine dispersion. It can be understood by Eq. (3.1.2), and the quantization of the transverse modes. In the lower panel, we zoom to the first five low energy modes, which follow a parabolic dispersion. The energy axis is scaled, such that we directly see the connection between the transverse confinement and the appearance of another mode, as given in Eq. (3.1.3). The dots are the results of the simulated dispersion relation whereas the solid curves follow Eq. (3.1.5).

still correctly simulated. At $k_x = 0$ using $\lambda_F = 2\pi/k_\mathsf{F}$ and demanding $\lambda_F \gg a$, we get the condition

$$\frac{W}{a} \gg \frac{n}{2}, \tag{3.1.7}$$

meaning that the width has to be orders greater than the number of modes we want to simulate. This was certainly fulfilled for Fig. 3.3, where we showed five modes which were simulated on a lead of width $W = 100a$. But if we look at higher energies, we notice the deviation from the continuum expectations due to the lattice structure. In Fig. 3.4, we show for the lead of width $W = 100a$ the location of the simulated band minima in comparison to the expected location from Eq. (3.1.3). We can clearly see the deviation of the two curves as soon as the number of modes reaches the order of the width of the lead.

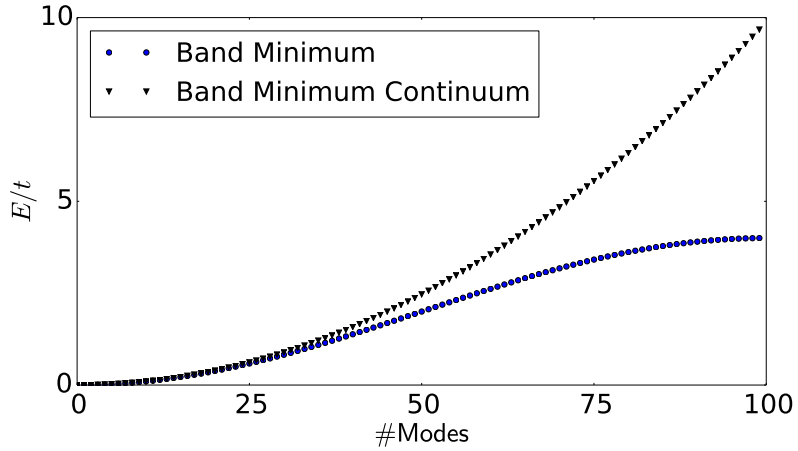

Figure 3.4.: The energy of the band minimum taken from the simulation (blue curve) compared to the theoretical minima from Eq. (3.1.3) (black curve) for a system of width $W = 100a$. We see that the curves start to deviate greatly when the number of modes is of the order of W/a.

3.2. Disorder

3.2.1. Born Approximation

To simulate more interesting systems, we introduce a simple method to simulate disorder on our two-dimensional lattice. We add impurities to the system by adding a disorder potential $V(\boldsymbol{r})$ to the Hamiltonian of (3.1.1)

$$H = \frac{p_x^2}{2m} + \frac{p_y^2}{2m} + V(x, y). \tag{3.2.1}$$

Numerically, each site of the lattice is independently added by a Gaussian or otherwise distributed random onsite potential. An ensemble average (denoted by $\langle\cdot\rangle$) of this potential gives

$$\langle V(\boldsymbol{r})\rangle = 0, \tag{3.2.2}$$

$$\langle V(\boldsymbol{r})V(\boldsymbol{r'})\rangle = a^2 V_0^2 \delta^{(2)}(\boldsymbol{r} - \boldsymbol{r'}). \tag{3.2.3}$$

Here, V_0^2 is the variance of the random distribution and a^2 accounts for the volume taken by the random potential. We discuss the theoretical expected mean free path for the system by calculating it in Born approximation, which is going to be explained in the following. Then, we check for diffusive systems whether the simulated conductance behaves appropriately.

The Fourier transform and its inverse are defined for this potential by

$$V(\boldsymbol{q}) = \int \mathrm{d}^2 r\, e^{-i\boldsymbol{q}\boldsymbol{r}} V(\boldsymbol{r}), \tag{3.2.4}$$

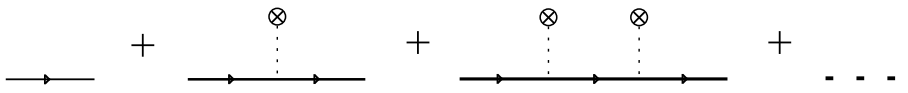

Figure 3.5.: Diagrammatic representation of the Dyson equation (3.2.10) for a disordered system. The solid line represents the free propagator, whereas the dashed lines represent the disorder potential.

$$V(\boldsymbol{r}) = \int \frac{\mathrm{d}^2 q}{(2\pi)^2} e^{i\boldsymbol{q}\boldsymbol{r}} V(\boldsymbol{q}). \tag{3.2.5}$$

Furthermore, we see the ensemble averaged potential is also delta correlated in Fourier space as

$$\langle V(\boldsymbol{q})\rangle = \int \mathrm{d}^2 r\, e^{-i\boldsymbol{q}\boldsymbol{r}} \langle V(\boldsymbol{r})\rangle = 0, \tag{3.2.6}$$

$$\langle V(\boldsymbol{q}) V(\boldsymbol{q'})\rangle = \int \mathrm{d}^2 r\, \mathrm{d}^2 r'\, e^{-i\boldsymbol{q}\boldsymbol{r}} e^{-i\boldsymbol{q'}\boldsymbol{r'}} \langle V(\boldsymbol{r}) V(\boldsymbol{r'})\rangle = a^2 V_0^2 (2\pi)^2 \delta^{(2)}(\boldsymbol{q}+\boldsymbol{q'}). \tag{3.2.7}$$

For a system with Hamiltonian $H = H_0 + V(\boldsymbol{r})$, the retarded Green's function of the clean system G_0 is defined as

$$G_0 = \frac{1}{E - H_0 + i0^+}. \tag{3.2.8}$$

The Green's function of the disordered system

$$G = \frac{1}{E - H + i0^+} \tag{3.2.9}$$

is obtained by expanding in V, which gives the Dyson equation

$$G = G_0 + G_0 V G_0 + G_0 V G_0 V G_0 + \cdots = G_0 + G_0 V G. \tag{3.2.10}$$

In diagrammatic terms, this series can be depicted as shown in Fig. 3.5. For further use, we are interested now in calculating the self energy Σ of the ensemble averaged Green's function for the disordered system. This means, we want to calculate Σ of

$$\langle G\rangle = G_0 + G_0 \Sigma \langle G\rangle. \tag{3.2.11}$$

In Born approximation, we sum the ensemble averaged one particle irreducible diagrams up to second order, meaning we calculate

$$\Sigma = \langle V\rangle + \langle V G_0 V\rangle, \tag{3.2.12}$$

which is diagrammatically depicted in Fig. 3.6.

The first order term vanishes from the property of the chosen disorder potential

$$\Sigma^{(1)}(\boldsymbol{p}) = \langle V(\boldsymbol{p})\rangle = 0. \tag{3.2.13}$$

Whereas the second order is given by

$$\Sigma^{(2)}(\boldsymbol{p}) = \int \frac{\mathrm{d}^2 q}{(2\pi)^2} \frac{\mathrm{d}^2 q'}{(2\pi)^2} \langle V(\boldsymbol{q}) G_0(\boldsymbol{p}-\boldsymbol{q}) V(-\boldsymbol{q'})\rangle. \tag{3.2.14}$$

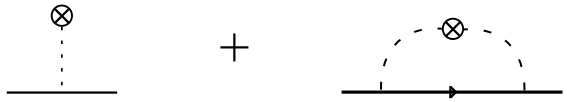

Figure 3.6.: Ensemble averaged terms evaluated in Born approximation in Eq. (3.2.12). The first term will vanish, whereas the second term will give a contribution that gives rise to a finite mean free path.

The Green's function of the clean system is not affected by the ensemble average, and thus we can make use of the delta-correlation of the potential, which gives

$$\Sigma^{(2)}(\boldsymbol{p}) = a^2 V_0^2 \int \frac{\mathrm{d}^2 q}{(2\pi)^2} G_0(\boldsymbol{p}-\boldsymbol{q}). \tag{3.2.15}$$

We use the density of states $\int \mathrm{d}E D_{2d}(E) = \int \mathrm{d}^2 k/(2\pi)^2$ to evaluate the integral as an energy integral

$$\Sigma^{(2)}(\boldsymbol{p}) = a^2 V_0^2 \int \mathrm{d}E\, D_{2d}(E) \frac{1}{E - H_0 + i0^+}. \tag{3.2.16}$$

The imaginary part of the self-energy gives rise to a finite lifetime of the associated quasiparticles. It is defined by

$$\frac{1}{\tau} = -\frac{2}{\hbar} \operatorname{Im} \Sigma(\boldsymbol{p_F}). \tag{3.2.17}$$

Then, using the Sokhotski-Plemelj theorem (2.9.6), the lifetime is essentially given by Fermis golden rule

$$\frac{1}{\tau} = \frac{2\pi}{\hbar} a^2 V_0^2 D_{2d}(E_\mathsf{F}). \tag{3.2.18}$$

We define the mean free path via $l = v_\mathsf{F}\tau$, and obtain the formula

$$l = \frac{\hbar v_\mathsf{F}}{2\pi} \frac{1}{a^2 V_0^2 D_{2d}(E_\mathsf{F})}. \tag{3.2.19}$$

The density of states is calculated in Appendix A.4. For a system with parabolic dispersion relation as in our GaAs case, the density of states is independent of the energy and given by Eq. (A.4.4). The calculation of the velocity yields $\hbar v = dE/dk = 2ka^2 t$, and therefore we obtain the mean free path in Born approximation by

$$\frac{l_\mathsf{GaAs}}{a} = \frac{4t^{3/2}\sqrt{E_\mathsf{F}}}{V_0^2}. \tag{3.2.20}$$

3.2.2. Mean Free Path and Beta Function

In the next step, we check whether our numerical simulation reproduces the result from the Born approximation. Therefore, we look at a disordered system of finite length L, which is connected to clean leads of the same lattice structure. We would expect that the system shows diffusive transport for $l < L < Nl$ and localized transport for $L > Nl$ [21]. For shorter

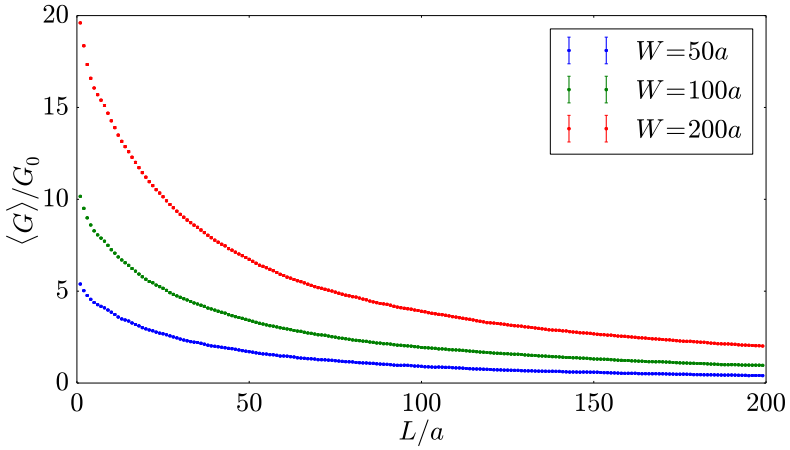

Figure 3.7.: Simulated conductance in units of the conductance quantum $G_0 = 2e^2/h$ averaged over 200 systems. The systems are simulated at $E = 0.1t$ with gaussian distributed onsite disorder terms with a variance of $V_0 = 0.3t$. The conductance falls of proportional to the inverse of the system length in the diffusive regime, and then starts to decrease exponentially in the localized regime. The value of the conductance of a system without disorder is determined by the number of transmitting channels, which can be obtained from Eq. (3.1.4), and is reached at $L = 0$.

systems the conductance should tend to the ballistic value, which is essentially determined by the number of propagating modes N.

In the diffusive regime the ensemble averaged conductance G should, for a system with fixed width W, decrease with the inverse of the length following Ohm's law

$$\langle G\rangle = \sigma\frac{W}{L}. \tag{3.2.21}$$

In the localized regime on the other hand we expect an exponential decay of the conductance

$$\langle G\rangle \propto e^{-L/\xi}. \tag{3.2.22}$$

The localization length ξ for a system with time reversal and spin rotational symmetry is approximately given by $\xi \approx Nl$ [21]. In the following, we calculate from the simulated scattering matrix the conductance (as described in Sect. 2.7) of different systems with fixed width and energy for different lengths. In the definition of the conductance quantum, we include a factor of two to account for the spin degeneracy, which is not simulated. We average the conductance for systems with fixed width and increasing length over various disorder configurations. The result for three different simulations is shown in Fig. 3.7. The diffusive and localized regime become visible in the plot of the inverse data and respectively in the logarithmic data, which are shown in Fig. 3.8.

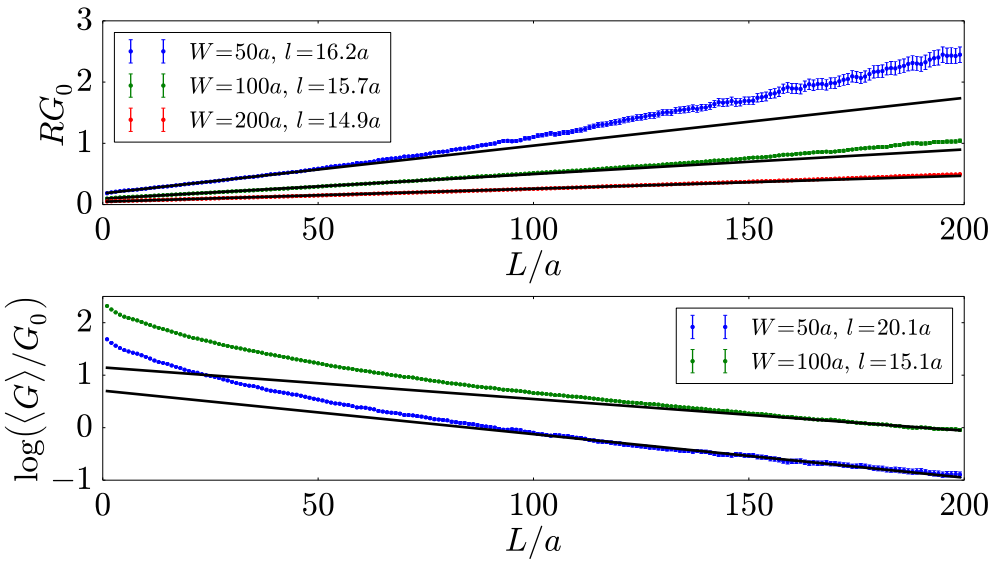

Figure 3.8.: The upper panel shows the inverse plot of Fig. 3.7. The data where the conductance $\langle G\rangle > 2G_0$ is estimated to behave linearly as expected in the diffusive regime and fit to Eq. (3.2.26). From this we calculate the mean free path, which should be $l = 14.1a$ in Born approximation (3.2.20) for the given parameters. The agreement improves with increasing system width. In the lower panel, we see a logarithmic plot of Fig. 3.7. The data corresponding to system lengths $L > Nl$ is linearly fit according to Eq. (3.2.22). The data for $W = 200a$ is not shown, as the localized regime is not within the simulated data. We calculate the mean free path from the slope by using $\xi \approx Nl$, where N is calculated from Eq. (3.1.4). The order of the results agrees quite well with the result from Born approximation. Visible error bars can be reduced by averaging over more systems.

For a ballistic system at $E = 0.1t$, we would expect at $W = 50a$ ($100a$, $200a$) from Eq. (3.1.4) $N = 6$ (11, 21) conducting modes. This coincides with the conductance of Fig. 3.7 for a system of zero length, which is equivalent to an infinite clean lead. With the inset of the disordered lattice sites, the conductance starts to drop. From Born approximation, we would expect from Eq. (3.2.20) that the mean free path is given by $l \approx 14.1a$. In the upper panel of Fig. 3.8, we plot the inverse data. We approximate the diffusive regime, which we use to estimate the mean free path numerically, as the data where there are still more than two transmissive channels. Here, we see a clear linear behavior with system length consistent with the expectation from Ohm's law

$$R = \frac{1}{\sigma W} L. \tag{3.2.23}$$

The conductivity is given in the diffusive regime by the Drude formula

$$\sigma = \frac{ne^2\tau}{m}. \tag{3.2.24}$$

Alternatively, by using $n = g_s g_v k_\mathsf{F}^2/4\pi$ (where we include possible spin and valley degeneracy), $\hbar k_\mathsf{F} = m v_\mathsf{F}$, and $v_\mathsf{F} = l/\tau$, the conductivity can be given by

$$\sigma = g_s g_v \frac{e^2}{h}\frac{k_\mathsf{F} l}{2}. \tag{3.2.25}$$

For the GaAs system with dispersion relation $E_\mathsf{F} = a^2 t k_\mathsf{F}^2$ and accounting for the spin degeneracy [1] $g_s = 2$, we can write

$$R = \frac{h}{2e^2}\frac{2a\sqrt{t}}{W\sqrt{E}l}L. \tag{3.2.26}$$

Therefore, we conclude from the slope of Fig. 3.8 (upper panel) the mean free path, which is in the same order as the expectation from the Born approximation. Wider systems, which start with a higher number of ballistic channels, get closer to the Born approximation result.

Furthermore, we can also compare the result to the mean free path that is estimated if we look at the localized regime, where the system length is $L > Nl$. In the lower panel of Fig. 3.8, we show the logarithm of the data and perform a linear fit for the the data with $L > Nl$, where we take N from Eq. (3.1.3), and approximate l from the result of the diffusive regime. The data for $W = 200a$ is dropped from the analysis as the localized regime is outside of the simulated frame. Using Eq. (3.2.22) and $\xi = Nl$, we can calculate the mean free path. The results show that the order of magnitude is reproduced in the simulation, and for the larger systems the agreement to the Born approximation is quite well. The visible error bars, which reduce the quality of the result, can be reduced by taking a greater ensemble average. As the errorbars are proportional to the inverse square root number of simulations, one would need to average over four times of the number of simulations to reduce the error bars by half.

Another interesting point, which is often analyzed in disordered systems [22, 23, 24, 25], is the scaling function $\beta(g)$ of the localizing system

$$\beta(g) = \frac{\mathrm{d}\log(g)}{\mathrm{d}\log(L)}. \tag{3.2.27}$$

Here, we defined the dimensionless conductance

$$g = \frac{G}{G_0}, \tag{3.2.28}$$

which is equal to the dimensionless conductivity for a system of aspect ratio $W/L = 1$. The β function gives us information about how the system localizes due to the disorder of the system if we were to increase the system size at fixed aspect ratio. According to the scaling

[1] Which we consistently also did when we applied the Landauer formula as described in Sect. 2.7.

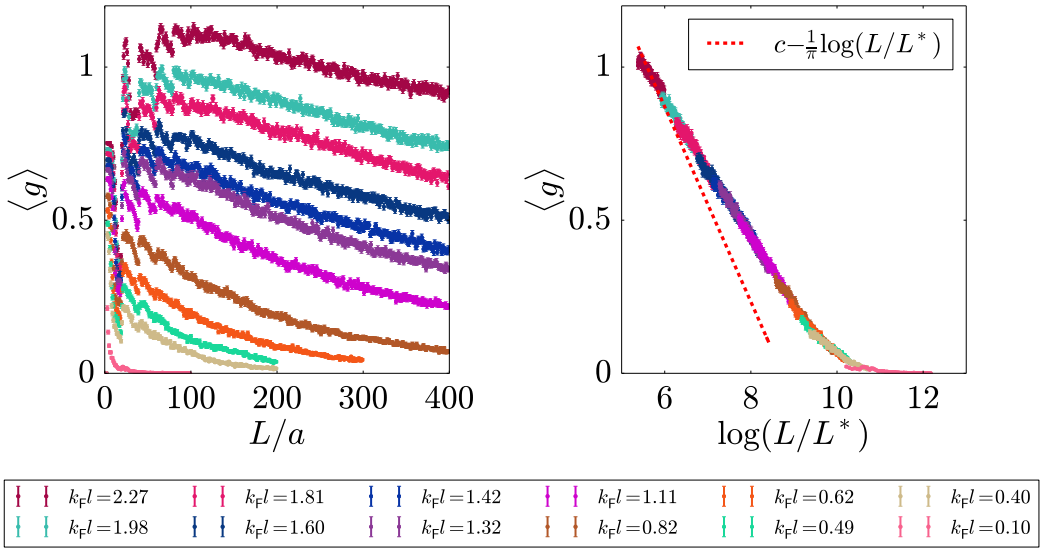

Figure 3.9.: The left panel shows the dimensionless conductivity g over the system size L for disordered 2-dimensional systems with a fixed aspect ratio of $W/L = 1$, averaged over 1000 systems each. The data rises to the value that can be calculated from the Drude formula in Eq. (3.2.25), and then drops due to localization effects. In the right panel, the length scales of the different datasets were rescaled to collapse all sets onto a single curve. The red dashed line shows the behaviour of the slope expected in first order from weak localization, as in Eq. (3.2.30), where we used some arbitrary y-axis intercept c for visibility. The data deviates a bit from the slope due to finite-size corrections and the low conductivity values, but still the tendency is visible.

theory of localization of Anderson et al. [22], the β function is universal for system sizes $L > l$ and depends only on the conductivity of the system and the dimensionality. We expect in two dimensions for $k_F l \gg 1$ that $\beta(g)$ tends to zero for large conductances in accordance to Ohm's law. For weak disorder, the theory of weak localization predicts negative corrections, which go as g^{-1} and are given in first order by [23]

$$\beta(g) = -\frac{1}{\pi}\frac{1}{g}. \tag{3.2.29}$$

For the evaluation, we can simulate different systems around $k_F l \approx 1$, and due to the universal behaviour they should all collapse to a single curve, after rescaling the length scales of the different simulations. In Fig. 3.9, we show in the left panel the measured dimensionless conductance for various systems simulated at different $k_F l$ values. The aspect ratio was fixed at $W/L = 1$ and the disorder average was taken over 1000 systems for each curve. The value for the mean free path is estimated from the Eq. (3.2.20) of the Born approximation for each

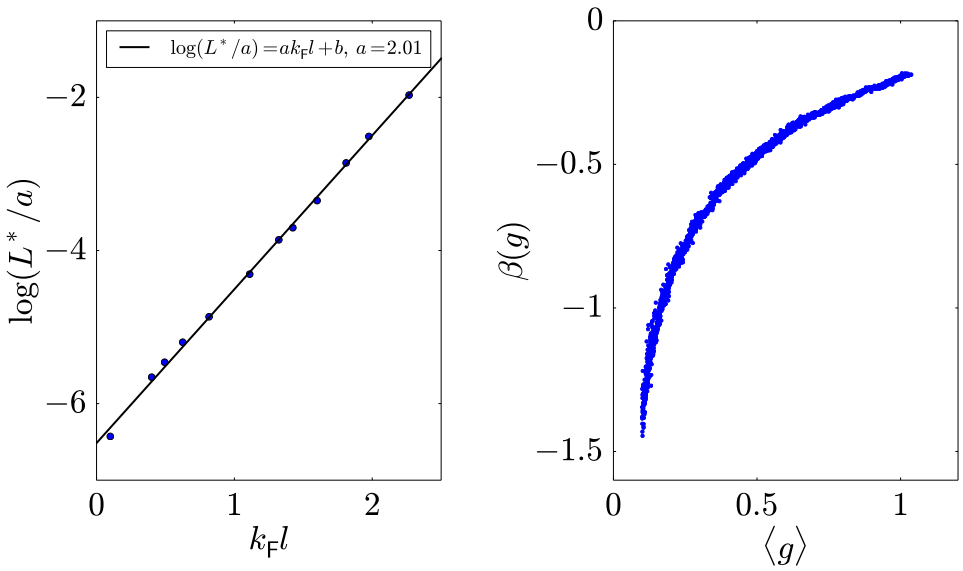

Figure 3.10.: The left panel shows the logarithm of the used scaling factors for the data from Fig. 3.9 as blue dots over $k_\mathrm{F}l$. We see that the scaling factors depend exponentially on $k_\mathrm{F}l$ as expected from the theory of weak localization, see Eq. (3.2.31). The black curve shows a linear fit, where we see that the fitted slope is again larger than the expected $\pi/2$. This is connected to the finite-size errors already visible in the raw data sets. The right panel finally shows the resulting β function. It was evaluated only for the data points with $g > 0.1$ due to the diverging nature. It shows the functional form expected from [22].

system. We see that the conductance rises to the diffusive value given by the Drude formula in Eq. (3.2.25), and decreases for increasing system size due to localization effects. In the right panel, the collapsed data is shown over the rescaled length on a logarithmic scale. From Eq. (3.2.29), we expect the data to follow the curve [23]

$$g = g_0 - \frac{1}{\pi} \log\left(\frac{L}{\tilde{l}}\right), \tag{3.2.30}$$

where g_0 is a large conductance value at length $\tilde{l}$. The slope of the expectation is shown as red dashed line in the right panel of Fig. 3.9. A deviation for the slope of the collapsed curve is visible due to two reasons. One reason are finite-size corrections in the system size, which is only limited due to limited computational power. Second, systems with even higher conductance and therefore smaller disorder need to be simulated, which again needs large systems to see localization effects.

From Eq. (3.2.30), the localization length in two dimensions can be estimated by setting $\tilde{l}$ to the mean free path, and g_0 to the diffusive conductance value from the Drude formula, which is given by Eq. (3.2.25) in units of the conductance quantum. Then, we can evaluate

at which length $L = \xi^{(2)}_{\mathsf{loc}}$, the weak-localization correction is of comparable size to g_0 by

$$\xi^{(2)}_{\mathsf{loc}} \approx l \exp\left(\frac{\pi}{2} k_{\mathsf{F}} l\right). \tag{3.2.31}$$

In the left panel of Fig. 3.10, we show the scaling factors used in the data collapse. The values follow up to corrections the functional form given by the two-dimensional localization length. Again the deviation can be accounted for by the finite-size deviation. Concludingly, the β function shown in Fig. 3.10 shows the same behaviour as the curve shown in the paper of Anderson et al. [22] for $d = 2$. The prefactor is in the same order and deviations are accounted to finite-size limitations.

We conclude that the presented form of implementing disorder reproduces the theoretical results in the right order. Using the Born approximation, we can estimate the mean free path from the applied variance in the disorder fluctuations at a given energy.

3.3. Magnetic Fields

Having simulated a 2DEG with disorder, we want to step ahead and look at how to include magnetic fields into the numerical simulation. This will give us for example the possibility to examine the famous quantum Hall effect. In 1975, Ando, Matsumoto and Uemura predicted the integer quantization of the Hall conductance in a two-dimensional electron system subjected to a magnetic field [26]. Five years later, Klaus von Klitzing discovered experimentally the exact quantization and was awarded the Nobel prize in physics in 1985. The extreme precision of the quantization of the Hall conductance can be used nowadays to measure integer or fractional multiples of e^2/h to about one part in a billion [27]. Therefore, the quantum Hall effect is used as a standard for high accuracy resistance measurements, defining the von Klitzing constant as $R_K = h/e^2 = 25812.807557(18)\Omega$.

The integer quantum Hall effect can be understood by looking at a non-interacting, two-dimensional electron gas, which is subjected to a strong magnetic field. It has been discussed thoroughly in the last decades, and one can quickly get lost in the literature concerning details of the quantum Hall effect [28, 29]. In the following, we will focus on the main aspects. We shortly remind of the classical Hall effect and show how to treat the system quantum mechanically. In a numerical simulation, we check the dispersion relation and whether the energy levels are quantized according to theory.

3.3.1. Classical Hall Effect

For the appreciation of the quantum Hall effect, we shortly remind of the classical Hall Effect. For this purpose, we consider a classical six terminal device, which is penetrated perpendicular to the plane by a magnetic field $\vec{B} = B\boldsymbol{e}_z$ as depicted in Fig. 3.11.

An electron current I is driven in x-direction of the system. The terminals allow to measure the longitudinal resistance $R_{xx} = V_{xx}/I$ and the transverse resistance $R_{xy} = V_{xy}/I$, also called the Hall resistance. The resistance is related to the resistivity by $R = \rho L/A$. For this

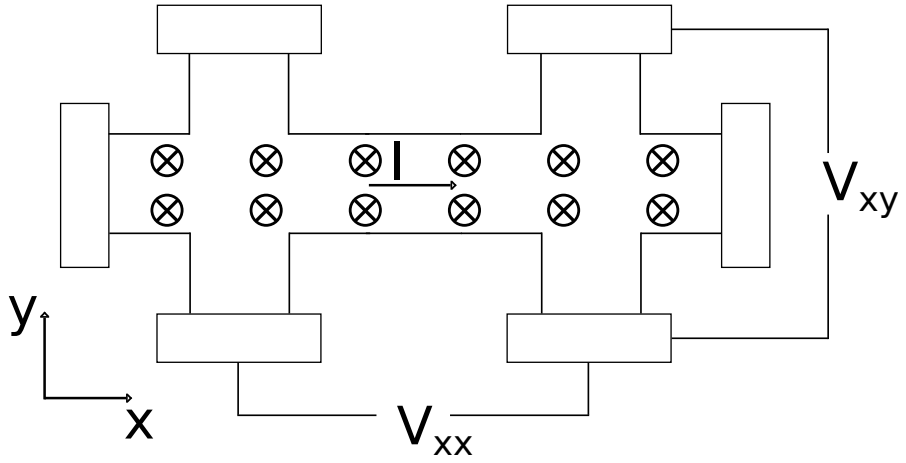

Figure 3.11.: Six terminal setup for a Hall measurement. The current is driven in the direction of the x-axis, while a magnetic field is applied perpendicular to the plane. The longitudinal resistance R_{xx} is given by measuring the voltage drop V_{xx} in longitudinal direction, whereas the transverse resistance R_{xy} is given by the transverse voltage drop V_{xy}.

2-dimensional setup the considered length of R_{xy} is just given by the width of the system and therefore $\rho_{xy} = R_{xy}$, whereas $\rho_{xx} = R_{xx}L/W$ is multiplied by an aspect ratio.

Classically, the magnetic field bends the electron trajectories through the Lorentz force $\vec{F_\mathsf{L}} = -e\vec{v} \times \vec{B}$. This amounts to a density gradient between the vertically opposing sites of the device and thus a compensating electric field $\vec{E}$, such that the resulting force on the electrons $\vec{F} = -e(\vec{E} + \vec{v} \times \vec{B}) = 0$ vanishes. Using Ohm's law $\vec{j} = \sigma\vec{E}$ and expressing the current density as $\vec{j} = -n_\mathsf{el}e\vec{v}$, where n_el is the electron density, we can calculate the resistivity tensor as the inverse of the conductivity tensor which results in

$$R_{xx} = 0, \tag{3.3.1}$$

$$R_{xy} = \frac{1}{en_\mathsf{el}}B. \tag{3.3.2}$$

In the case of a sample with generic impurities, we can use the Drude theory to model the diffusive transport, and to obtain the classical result for the resistivity in a straight forward calculation [28]. Defining the mobility of the electron gas μ, which is in the Drude theory connected by $\mu = e\tau/m$ to the mean free time between two ionic collisions τ, the result reads

$$\rho_{xx} = \frac{1}{n_\mathsf{el}e\mu}, \tag{3.3.3}$$

$$R_{xy} = \frac{1}{n_\mathsf{el}e}B. \tag{3.3.4}$$

The results coincide for $\tau \to \infty$. We note that the transverse resistivity is proportional to the magnetic field, while the longitudinal resistivity is independent of it. By using $n_\mathsf{el} = k_\mathsf{F}^2/4\pi$

as noted in A.4, $E_\mathsf{F} = \hbar^2 k_\mathsf{F}^2/2m$ and introducing the cyclotron frequency

$$\omega_c = \frac{eB}{m}, \tag{3.3.5}$$

we can furthermore write

$$R_{xy} = \frac{h}{e^2}\frac{\hbar\omega_c}{E_\mathsf{F}}. \tag{3.3.6}$$

3.3.2. Integer Quantum Hall Effect

In semiconductor layer systems with high mobilities in a 2DEG setup, which is subjected to a magnetic field, one observes a quantization of the transverse resistance in terms of the von Klitzing constant

$$R_{xy} = \frac{h}{e^2}\frac{1}{n}. \tag{3.3.7}$$

The Hall resistance increases stepwise for increasing magnetic fields, whereas the longitudinal resistance vanishes at the plateaus. This is especially true independent of the geometry of the system and the presence of disorder. For the latter statement, we will see that a magnetic length scale can be associated with the magnetic field, and the robustness against disorder is only given when this length scale is significantly smaller than the mean free path, which is given by the disorder.

To understand the observed quantization of the resistance, we start by first describing the Hamiltonian of a free two-dimensional electron gas, which is exposed to a magnetic field. Quantum mechanically the magnetic field can be included in the Hamiltonian by minimal coupling $\boldsymbol{p} \to \boldsymbol{p} - q\boldsymbol{A}$, which gives

$$H = \frac{(\boldsymbol{p} + e\boldsymbol{A})^2}{2m}. \tag{3.3.8}$$

The magnetic field is thus implemented via the vector potential $\mathrm{rot}\boldsymbol{A} = \boldsymbol{B}$. The gauge freedom of the vector potential can be used to adjust the vector potential according to the setup geometry. A good choice for our Hall bar system is the Landau gauge

$$\boldsymbol{A} = -By\boldsymbol{e}_x. \tag{3.3.9}$$

In this gauge the Hamiltonian remains translationally invariant with respect to the x-direction, and therefore we can use the Fourier transform of the wavefunction

$$\Psi(x, y) = \int \mathrm{d}k\, e^{ik_x x}\phi_k(y). \tag{3.3.10}$$

The Schrödinger equation $H\Psi_\nu(x, y) = E_\nu\Psi_\nu(x, y)$ reduces to an equation for $\phi_{k_x}(y)$. Defining the cyclotron frequency as in Eq. (3.3.5) and introducing the magnetic length scale

$$l_B = \sqrt{\frac{\hbar}{eB}}, \tag{3.3.11}$$

we need to solve

$$\left[\frac{p_y^2}{2m} + \tfrac{1}{2}m\omega_c^2\big(y - l_B^2 k_x\big)^2\right]\phi_{\nu k_x}(y) = E_\nu \phi_{\nu k_x}(y). \tag{3.3.12}$$

Without any additional boundary conditions, except that the solutions need to be square integrable and thus vanish at $\pm\infty$, this is just the Schrödinger equation of a harmonic oscillator shifted by $y_0 = l_B^2 k_x$. The shift does not affect the eigenenergies of the free harmonic oscillator, which are given by $\big(\nu = 0,\, 1,\, 2,\, \ldots\big)$

$$E_\nu = \hbar\omega_c\left(\nu + \tfrac{1}{2}\right). \tag{3.3.13}$$

We see that the energy levels (which are termed Landau levels) can be calculated independent of k_x. Furthermore, we note how the cyclotron frequency determines the scale for the energy of the system. Comparing with the classically obtained result in Eq. (3.3.6), we see how the quantum number ν, which determines the number of open channels below E_F, is the reason for the observed quantization in the quantum Hall effect.

The corresponding wavefunction of the system are those of the shifted quantum harmonic oscillator

$$\phi_{\nu k}(y) = \frac{1}{\sqrt{2^\nu \nu! l_B \sqrt{\pi}}} H_\nu(y l_B^{-1} - l_B k_x) e^{-\frac{1}{2}(y l_B^{-1} - l_B k_x)^2}, \tag{3.3.14}$$

where $H_\nu\big(x\big)$ are the Hermite polynomials.

From this simple analytic analysis, we get the discreteness of the energy levels of a clean bulk quantum Hall system. This ultimately results in the step wise increase of the conductance for decreasing magnetic fields. The model can be extended by some effort to analyze the effect of a hard wall in the system [30, 31]. The essential result is that the current in a quantum Hall system is carried over chiral edge states. Therefore, backscattering is suppressed, which results in the observed exact quantization even in the presence of disorder. In A.5, we show analytically how a single hard wall affects the energy levels of the system to give an insight to the calculations.

3.3.3. Numerical Simulation

To simulate the integer quantum Hall effect numerically, we take the Hamiltonian of (3.2.1), and add a magnetic field as described in Appendix A.3 using the Landau gauge of Eq. (3.3.9). The continuum Hamiltonian, which we simulate, is thus

$$H = \frac{(p_x - eBy)^2}{2m} + \frac{p_y^2}{2m} + V\big(x, y\big). \tag{3.3.15}$$

The Peierls substitution (A.3.2) for this vector potential leaves hopping between the lattice points (n, m) and $(n, m+1)$ in y-direction unchanged (as $A_y = 0$). Whereas, the nearest neighbor hopping between (n, m) and $(n+1, m)$ becomes

$$t^x_{nm} = -t\exp\left(i\frac{a^2}{l_B^2}m\right). \tag{3.3.16}$$

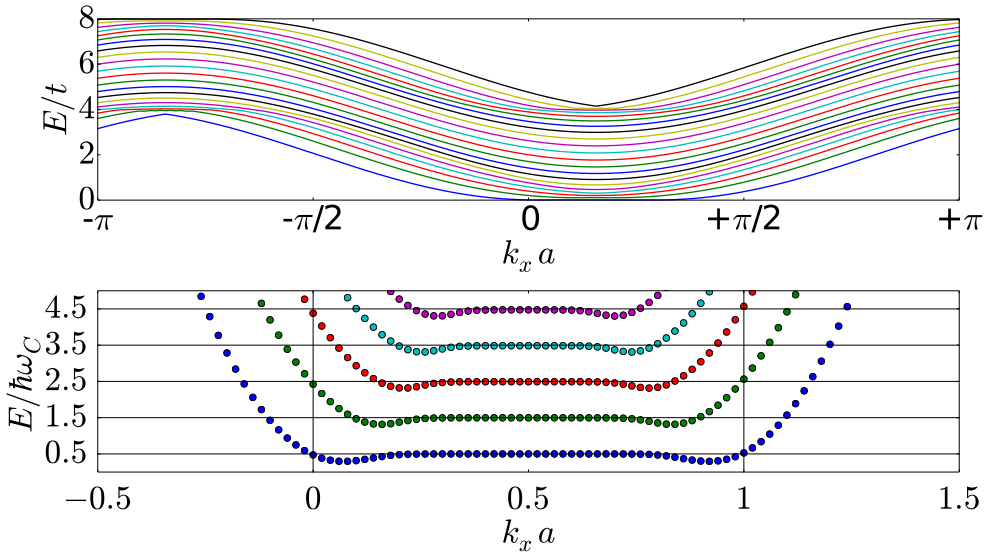

Figure 3.12.: The upper panel shows every 5$^{\text{th}}$ mode of the dispersion relation for an infinite lead of finite width $W = 100a$ in a magnetic field, which was implemented by the Peierl's substitution and corresponds to a magnetic length of $l_B = 10a$. In the lower panel, we zoom to the lowest energy modes. They correspond to the expectation from the calculations in Appendix A.5. The down bending at the edge is an additional artifact from the chosen discretization scheme.

Using the definition of the hopping parameter t from Eq. (A.2.4), the energy levels (3.3.13) are given by

$$E_\nu = \frac{2a^2 t}{l_B^2}\left(\nu + \tfrac{1}{2}\right). \tag{3.3.17}$$

Thus to have any transmitting channel in the system, we already note that

$$\frac{E_\mathsf{F}}{t} > \frac{a^2}{l_B^2}. \tag{3.3.18}$$

It is again crucial to discuss the parameter regime for the simulation. To simulate the magnetic system correctly, we have to add the condition that the magnetic length is simulated adequately by the lattice

$$l_B \gg a. \tag{3.3.19}$$

We want to make sure that the finite width restriction of the system does not overshadow the quantum Hall effect. Therefore we demand that we have for the N simulated quantum Hall levels M levels in the system without magnetic field and that $M > N$. The number of transmitting channels of a quantum Hall system at Fermi energy E_F is given by

$$N = \left\lfloor \tfrac{1}{2}\left(1 + \frac{E_\mathsf{F} l_B^2}{t a^2}\right)\right\rfloor. \tag{3.3.20}$$

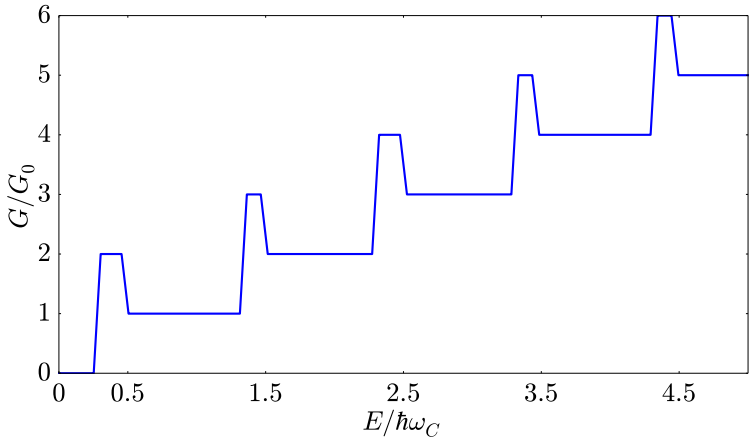

Figure 3.13.: The conductance steps associated with the dispersion relation of Fig. 3.12. The conductance is again given in units of the conductance quantum $G_0 = 2e^2/h$. The down bending of the Landau levels in the dispersion relation results in an overshoot before every quantum Hall step. For increasing width of the system the energy range of the peaks decreases. The plot also shows that a new quantum of conductance is added, whenever the energy passes another level given by Eq. (3.3.13).

Using the calculated number of channels in a constrained system without magnetic field from Eq. (3.1.4), we obtain the condition for the system parameters

$$\frac{\pi a}{2W}\left(\frac{l_B^2}{a^2}\sqrt{\frac{E_\mathsf{F}}{t}} - \sqrt{\frac{t}{E_\mathsf{F}}}\right) < 1. \tag{3.3.21}$$

The condition of Eq. (3.3.18) ensures that the left hand side is positive. In combination with the condition that E_F has to be small in the simulation (3.1.6) and the desire to simulate several quantum Hall levels correctly $N \gg 1$, we are quickly in the regime where we have to simulate large system sizes W.

By the way, we note another possibility to state how many lattice plaquettes fit into a magnetic length square l_B^2/a^2. By using the definition of the magnetic length from Eq. (3.3.11), the definition for the magnetic flux quantum $\Phi_0 = h/e$, and the definition of the flux for a single plaquette from the square lattice $\Phi = Ba^2$, we have the identity

$$\frac{l_B^2}{a^2} = \frac{1}{2\pi}\frac{\Phi_0}{\Phi}. \tag{3.3.22}$$

Equipped with the preliminary theoretical work, we can check whether a numerical simulation reproduces the quantum Hall effect characteristics in a finite-sized probe. It is interesting to look whether the right dispersion relation is simulated for a clean infinite magnetic lead. In the upper panel of Fig. 3.12, we clearly see a change in the overall dispersion relation, after

the Peierl's substitution, compared to the result shown in Fig. 3.3. The lower panel reveals that the low energy modes show flat energy bands. The dispersion relation shows most of the characteristics as expected from the calculations in the Appendix A.5. The energy levels bend upwards at $k_x = 0$ and $k_x = W/l_B^2$ having the energy value of the half harmonic oscillator at these points. As an artifact of the tight binding simulation, we see additionally that the energy levels overshoot when they bend down to the energy of the Landau levels. Due to this overshoot, the corresponding conductance plot for a clean system overshoots before every step as shown in Fig. 3.13. If we were to set the constant onsite terms not to the number of nearest neighbors, but set the edge sites also to $\epsilon_n = 4$, these dips would disappear. Therefore, the artifact stems from the discretization scheme and disappears in the limit of large systems.

4. Graphene

In the following section, we want to turn our focus of interest on the electronic transport properties of graphene. It is a crystalline allotrope of carbon with 2-dimensional properties. The lattice structure was known in theory for many decades, but yet it was just first produced in the laboratory in 2004 by Novoselov et al. [1]. The electronic configuration of atomic carbon is [He]$2s^2 2p^2$. In graphene, a 2s orbital is mixed with two of the three available 2p orbitals forming three sp^2 orbitals. The hybridized orbitals of carbon form three robust σ-bonds with other carbon atoms with a carbon-carbon bond length of about $a_0 = 1.42$Å. This results in a regular honeycomb lattice (see Fig. 4.1). The resulting σ-band has a filled shell and forms a deep valence band. It is responsible for the robustness of the carbon allotrope. The last remaining p-orbital is perpendicular to the planar structure and forms a covalent π-bond with the neighboring carbons atoms. The π-band is half-filled and is responsible for the conducting properties [32].

4.1. Tight Binding Model

The transport in graphene can be modeled to some extent by a tight binding Hamiltonian on a honeycomb lattice with only nearest neighbour interaction. We will focus on the low-energy states which are, as we will see, described by a massless Dirac Hamiltonian $H = v_\mathsf{F} \boldsymbol{p} \cdot \boldsymbol{\sigma}$. We will start with a description on the atomic level to derive the basic equations. Our honeycomb lattice is described as seen in Fig. 4.1, by using a lattice with unit cell vectors

$$\boldsymbol{a}_1 = a \begin{pmatrix} 1 \\ 0 \end{pmatrix}, \tag{4.1.1}$$

$$\boldsymbol{a}_2 = \frac{a}{2} \begin{pmatrix} 1 \\ \sqrt{3} \end{pmatrix}. \tag{4.1.2}$$

Each unit cell has two sites A and B in it that are positioned respectively at $(0, 0)$ and at $(0, a/\sqrt{3})$. The nearest neighbour vectors, pointing from the sites of sublattice A to the sites of sublattice B, are given by

$$\boldsymbol{\delta}_1 = \frac{a}{2\sqrt{3}} \begin{pmatrix} -\sqrt{3} \\ -1 \end{pmatrix}, \tag{4.1.3}$$

$$\boldsymbol{\delta}_2 = \frac{a}{2\sqrt{3}} \begin{pmatrix} \sqrt{3} \\ -1 \end{pmatrix}, \tag{4.1.4}$$

$$\boldsymbol{\delta}_3 = \frac{a}{\sqrt{3}} \begin{pmatrix} 0 \\ 1 \end{pmatrix}. \tag{4.1.5}$$

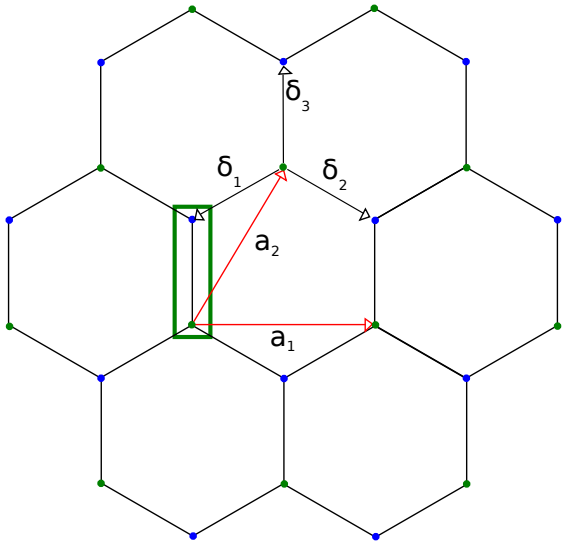

Figure 4.1.: The honeycomb lattice and the main lattice vectors. A unit cell contains two sites (grouped by green rectangle), one from sublattice A (green dots) and one from sublattice B (blue dots). The complete lattice can be spanned by $\boldsymbol{a}_1$ and $\boldsymbol{a}_2$ which are of length a, with atoms positioned in the unit cell at $(0,0)$ and $(0, a/\sqrt{3})$. The nearest neighbor vectors are defined from sublattice A to sublattice B by $\boldsymbol{\delta}_1$, $\boldsymbol{\delta}_2$, and $\boldsymbol{\delta}_3$.

The reciprocal lattice, which basis vectors satisfy $\boldsymbol{a}_i \boldsymbol{b}_j = 2\pi\delta_{ij}$, can be spanned by

$$\boldsymbol{b}_1 = \frac{2\pi}{a}\begin{pmatrix} 1 \\ -1/\sqrt{3} \end{pmatrix}, \tag{4.1.6}$$

$$\boldsymbol{b}_2 = \frac{2\pi}{a}\begin{pmatrix} 0 \\ 2/\sqrt{3} \end{pmatrix}. \tag{4.1.7}$$

The first Brillouin zone is shown in Fig. 4.2. Due to the lattice symmetry only two of the six corners of the Brillouin zone are independent. Conventionally, they are called K and K', and in our description they are positioned at

$$\boldsymbol{K} = \frac{4\pi}{3a}\begin{pmatrix} 1 \\ 0 \end{pmatrix}, \tag{4.1.8}$$

$$\boldsymbol{K'} = \frac{4\pi}{3a}\begin{pmatrix} -1 \\ 0 \end{pmatrix}. \tag{4.1.9}$$

In the simplest tight binding model on the honeycomb lattice, the onsite terms of the lattice are set to zero and a constant nearest neighbor hopping of $-t$ is considered. The Hamiltonian contains only terms for hopping from one sublattice to the other and is given by:

$$H = \begin{pmatrix} 0 & -tf^*(\boldsymbol{k}) \\ -tf(\boldsymbol{k}) & 0 \end{pmatrix}, \tag{4.1.10}$$

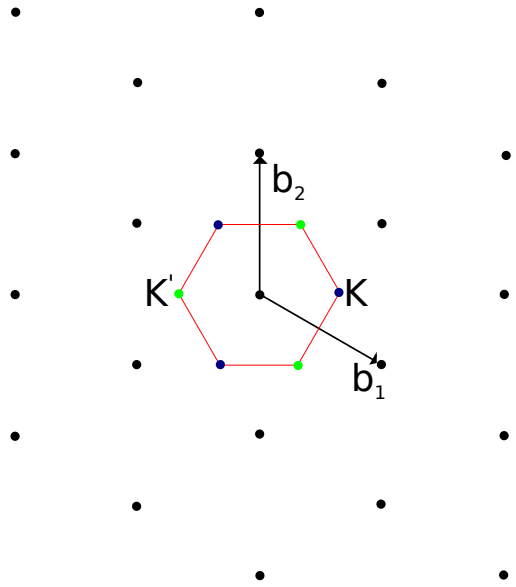

Figure 4.2.: First Brillouin zone constructed as the Wigner Seitz cell of the reciprocal lattice. The reciprocal lattice is spanned by $\boldsymbol{b}_1$ and $\boldsymbol{b}_2$, which satisfy $\boldsymbol{a}_i \cdot \boldsymbol{b}_j = 2\pi\delta_{ij}$. Due to the symmetry of the lattice, only the two corners K and K' of the first Brillouin zone are independent.

where $f(\boldsymbol{k}) = \sum_{\boldsymbol{\delta}_j} e^{-i\boldsymbol{k}\cdot\boldsymbol{\delta}_j}$ for the given lattice structure is

$$f(\boldsymbol{k}) = \exp\big(-i\frac{a}{\sqrt{3}}k_y\big) + 2\exp\big(i\frac{a}{2\sqrt{3}}k_y\big)\cos(\frac{a}{2}k_x). \tag{4.1.11}$$

The Hamiltonian acts on a spinor given by the wavefunction on the two sublattices

$$\Psi = \begin{pmatrix} \psi_A \\ \psi_B \end{pmatrix}. \tag{4.1.12}$$

The corresponding dispersion relation for the free bulk graphene system resulting from the tight binding Hamiltonian is given by

$$E = \pm t\sqrt{1 + 4\cos(\frac{a}{2}k_x)\cos(\frac{\sqrt{3}a}{2}k_y) + 4\cos^2(\frac{a}{2}k_x)}. \tag{4.1.13}$$

It is shown in Fig. 4.3, as well as the projections along the different axes. The low energy modes of the dispersion relation are found around the K or K' points. Here the dispersion shows a cone structure with a linear behavior. To see this, we develop the Hamiltonian around K with $\boldsymbol{k} = \boldsymbol{K} + \boldsymbol{q}$, where $|\boldsymbol{q}| \ll |\boldsymbol{K}|$ (the same can be done respectively for K'). This yields with $\xi = +1$ for K and $\xi = -1$ for K'

$$f(\boldsymbol{q}) = -\frac{\sqrt{3}}{2}a(\xi q_x + iq_y) + \mathcal{O}\big(q^2\big) \tag{4.1.14}$$

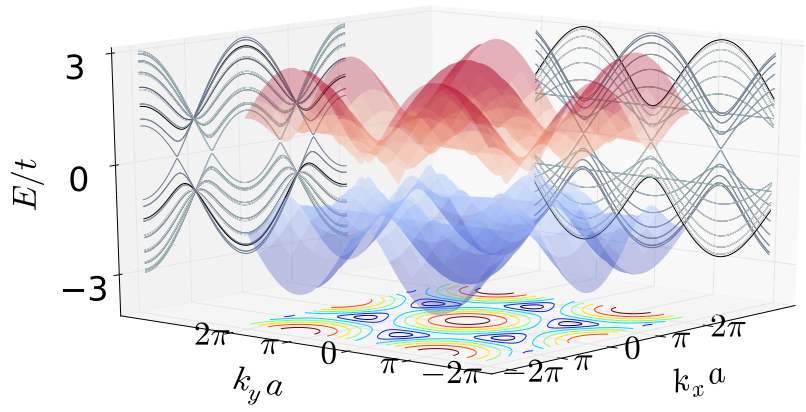

Figure 4.3.: Dispersion relation of the nearest neighbor tight bindinding model on the honeycomb lattice given by Eq.(4.1.13). We also show the respective projections onto the different axes. The projection along the k_x and k_y direction show the dispersion relations obtained for nanoribbons with different edges discussed in Sect. 4.2. The projection along the energy axis shows the hexagonal structure of the first Brillouin zone shown in Fig. 4.2. The shown dispersion is gapless (seemingly visible gaps are due to finite numerical resolution).

and therefore

$$H_\xi \approx \frac{\sqrt{3}}{2} at\xi \begin{pmatrix} 0 & q_x - \xi i q_y \\ q_x + \xi i q_y & 0 \end{pmatrix}, \tag{4.1.15}$$

where the spectrum is given independently of ξ by

$$E(\boldsymbol{q}) = \pm \frac{\sqrt{3}}{2} at \, |\boldsymbol{q}| \, . \tag{4.1.16}$$

The low-energy states can therefore also be modeled by the massless Dirac Hamiltonian. It can be written in shorthand notation by the use of Pauli matrices as

$$H_K = \hbar v_\mathsf{F} \boldsymbol{q} \cdot \boldsymbol{\sigma}. \tag{4.1.17}$$

For the K' valley one needs to interchange $\sigma_y \to -\sigma_y$. The dispersion relation of the massless Dirac Hamiltonian is given by

$$E(\boldsymbol{q}) = \pm \hbar v_\mathsf{F} \, |\boldsymbol{q}| \, . \tag{4.1.18}$$

Therefore, we identify

$$\hbar v_\mathsf{F} = \frac{\sqrt{3}}{2} at. \tag{4.1.19}$$

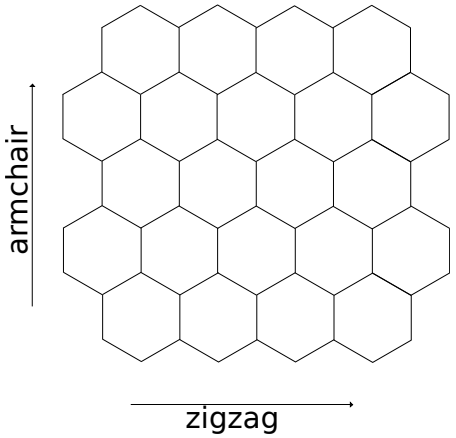

Figure 4.4.: Zigzag- and armchair-type edge of a graphene nanoribbon. The names stem from the respective form of the edges. The two different edge types show different transport properties for systems of finite width. The dispersion relation for ribbons with the respective edge along the transport direction are shown in Fig. 4.5 and Fig. 4.6.

For the graphene parameters $a \approx 2.46$Å and $t \approx 2.8$eV, we yield the Fermi velocity $v_\mathsf{F} \approx 10^6 \frac{m}{s}$.

4.2. Nanoribbons and Edge Types

As a first step for the simulation of graphene, we look into the dispersion relation of the leads, which we are using, like we did in the case of gallium arsenide in Sect. 3.1. We can only simulate leads of finite width in a numerical tight binding simulation, and it will be important to note which kind of edge the lead has. There are two extreme cases for the edges of the honeycomb lattice as depicted in Fig. 4.4. Edges of these types are called armchair or zigzag respectively. The energy spectra of these two types show some major differences at finite width, and are discussed in the following.

The dispersion relation in the case of a nanoribbon with zigzag edges is shown in Fig. 4.5. We note the two cone structures at $k_x = \pm 2\pi/3a$. The armchair edge case is shown in Fig. 4.6, where the two cones are located at the center. We can roughly understand the two dispersions by having sliced the bulk graphene spectrum, as shown in Fig. 4.3, along the k_x or k_y direction respectively. We remind here that the dispersion relation of Fig. 4.3 was obtained for a lattice with a zigzag direction along the x-axis and an armchair direction along the y-axis. Therefore the zigzag dispersion is obtained for slicing along k_x and the armchair dispersion by slicing along k_y.

To calculate the dispersion relations explicity, we would need to solve the Hamiltonian (4.1.10) with the respective boundary conditions. A detailed calculation can be found in [33]. For the energy modes of interest that are described by the Dirac Hamiltonian these calculations also can be found for example in [32, 34]. In these calculations special features

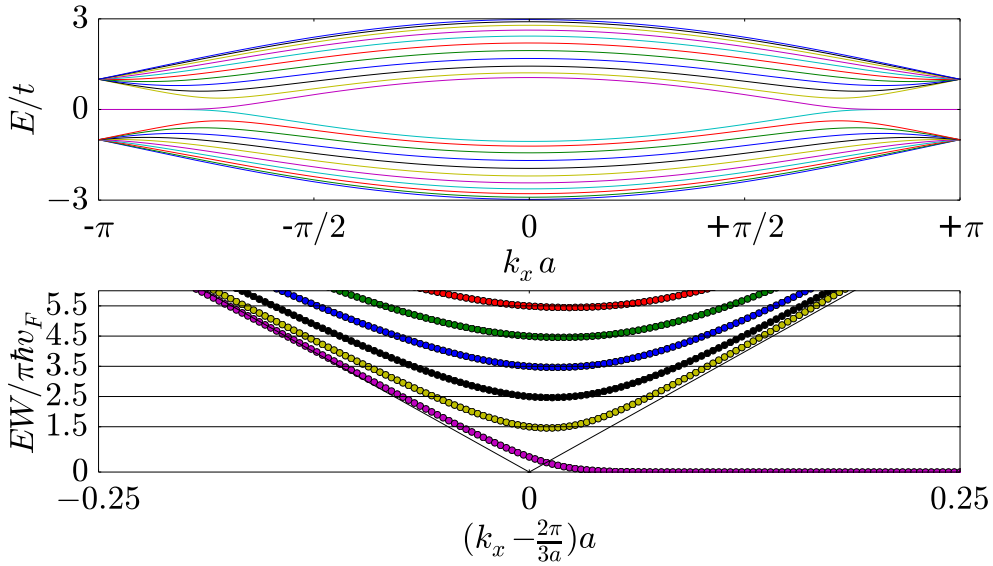

Figure 4.5.: Dispersion relation for a ribbon of width $W = 10a$ with zigzag edges (upper panel). Two cones are visible around $k_x = \pm 2\pi/3a$. The dispersion relation can be obtained by slicing the bulk graphene dispersion of Fig. 4.3 along the k_x direction. A zero-energy mode is visible connecting the two Dirac cones along a single direction. In the lower panel, a ribbon of width $W = 100a$ is simulated and we zoom to the momentum range around $k_x = 2\pi/3a$. The low-energy modes follow the dispersion of the Dirac Hamiltonian, which is shown as the black solid curve. New modes appear in a energy distance determined by the finite width constriction, see Eq. (4.2.1).

due to the edge structure, like a possible gap in the dispersion or zero energy modes, are derived. We will also observe these in the following results of numerical simulations.

In the lower panel of Fig. 4.5, we zoom to the positive energies of the cone from the zigzag edge ribbon at positive longitudinal momentum. We see that the different modes follow the linear dispersion asymptotically and that the energy difference between two modes is determined by the transverse constriction $\Delta E = \hbar v_{\mathsf{F}} \pi / W$. The zero energy mode corresponds to a surface state [32]. The band bottoms of the other modes are given by

$$E_n = \hbar v_{\mathsf{F}} \frac{\pi}{W} \left(n + \tfrac{1}{2}\right) \tag{4.2.1}$$

The zoomed dispersion relation of the ribbon with an armchair edge has more structure. For

$$W = (3r - 1)a, \tag{4.2.2}$$

where $r \in \mathbb{N}$, the armchair spectrum is gapless and otherwise gapped as seen in the lower panels of Fig. 4.6. Discussions on the details of the armchair dispersion can be found for

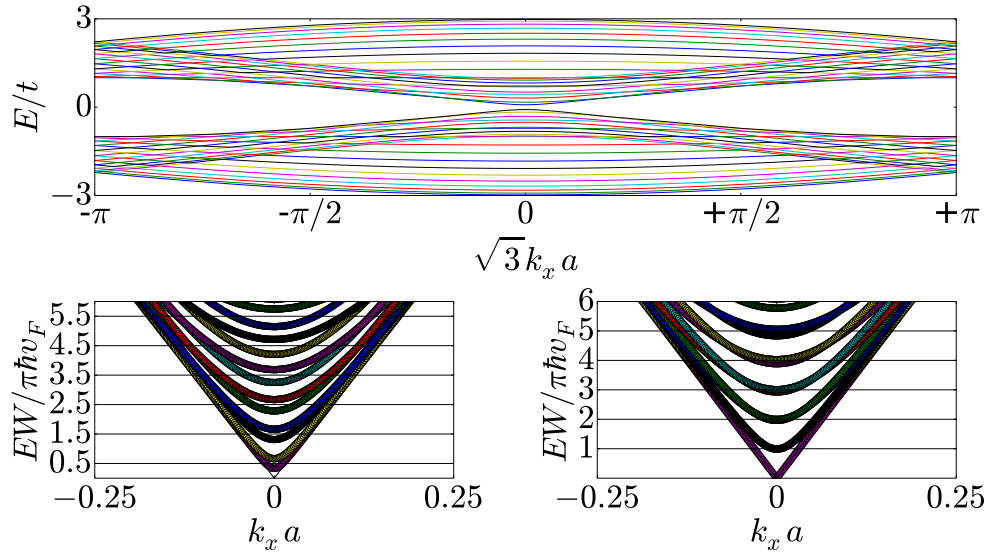

Figure 4.6.: Dispersion relation for a ribbon of width $W = 10a$ with armchair edges (upper panel). Only a single cone is visible at the center of the first Brillouin zone. The dispersion relation can be obtained by slicing the bulk graphene dispersion of Fig. 4.3 along the k_y direction. A closer look is shown in the lower left panel and reveals that every mode is nearly double degenerate. In the lower panels we show the low energy modes of an armchair ribbon with $W = 100a$ (left) and $W = 101a$ (right). Both follow asymptotically the dispersion relation of the Dirac Hamiltonian, as shown by the black solid curves. Only the lower right dispersion is gapless as the width of the system can be expressed by Eq. (4.2.2). The axis of the dispersion in the upper panel has an additional factor because the used unit cell in the simulation of the armchair lead is by a factor of $\sqrt{3}$ longer than the usual lattice constant a.

example in [32, 33, 34]. Most of the time, we will use only zigzag edges for our simulations of the leads as they are closer to the bulk properties of graphene and are always metallic. But still there are cases where we will use armchair edges. Sometimes it is unavoidable because of the lattice geometry (e.g. in the geometry used for the analysis of the Aharanov-Bohm effect in Sect. 4.6). And sometimes because the orientation of the lattice is demanded, as to see certain effects (e.g. a pseudo-magnetic field due to a changing strain field in a single direction as described in Sect. 4.7). Anyhow one should always be aware of the subtle differences one sees in the simulation due to the different edges.

4.3. System Size Scaling and Impedance Matching

To numerically simulate the electronic transport in graphene, we can implement the tight binding model on the honeycomb lattice in a similar fashion as to the square lattice model we used for gallium arsenide. Then, a scattering matrix can be calculated from which transmission amplitudes can be obtained.

Now in many cases, if we are only interested in the properties of the low-energy electrons, which are described by the Dirac Hamiltonian, it is not necessary to simulate in the atomic basis. We can simulate the tight binding honeycomb lattice with any lattice spacing $\tilde{a}$ and it's low energy states will always be given by a Dirac Hamiltonian. We see this from using the result of Sect. 4.1, where we expanded $\boldsymbol{k} = \boldsymbol{K} + \boldsymbol{q}$ with $|\boldsymbol{q}| \ll |\boldsymbol{K}|$ and showed that the low energy Hamiltonian of the honeycomb model for any lattice parameters is given by

$$H = \frac{\sqrt{3}}{2}\tilde{a}\tilde{t}\boldsymbol{q} \cdot \boldsymbol{\sigma}. \tag{4.3.1}$$

By scaling $\tilde{t}$ such that we have once again

$$\frac{\sqrt{3}}{2}\tilde{a}\tilde{t} = \hbar v_{\mathsf{F}} \tag{4.3.2}$$

we assure that the same physics is described as in the system calculated on the atomic length scale. By this knowledge we do not need to simulate the complete graphene lattice on an atomic basis but only have to simulate a lattice where any other relevant physical length scale is still greater than the used lattice spacing.

Another important point for the numerical simulation of an experiment in graphene is that the small scaled quantum devices of small widths are often connected to very wide leads. Having a constriction in the transversal structure leads to a quantization of the transverse momenta in the order of $k_n = n\pi/W$ (as shown in the previous Sect. 4.2). Therefore, we have the situation that we come from the wide leads, where there are many modes, down to only a few modes within the small device itself. If the change from one area to the other goes abrupt, we find a high impedance mismatch at the interface. This produces artifacts in the transmission like Fabry-Perot oscillations that depend on the distance of two interfaces. To avoid this impedance mismatch, the transition from the wide reservoir to the small quantum device needs to be smooth, such that the wavelength of the electrons changes only slowly

$$\frac{1}{2\pi}\frac{\mathrm{d}\lambda}{\mathrm{d}x} \ll 1. \tag{4.3.3}$$

In a simulation, wide leads which transit down to a small device are numerically unfavorable. As the part of the system, which represents the transition to the wide leads, would demand high computational power. Instead, we can simulate the many modes by doping the area outside of the system on a high energy level. Then, we can define an intermediate region of length L_{IM} where the high energy is tuned down to the energy of interest in the system. In this manner, the same situation is simulated with a much lower need of computational power. As we do not want to add additional symmetries into the setup, the profile of the

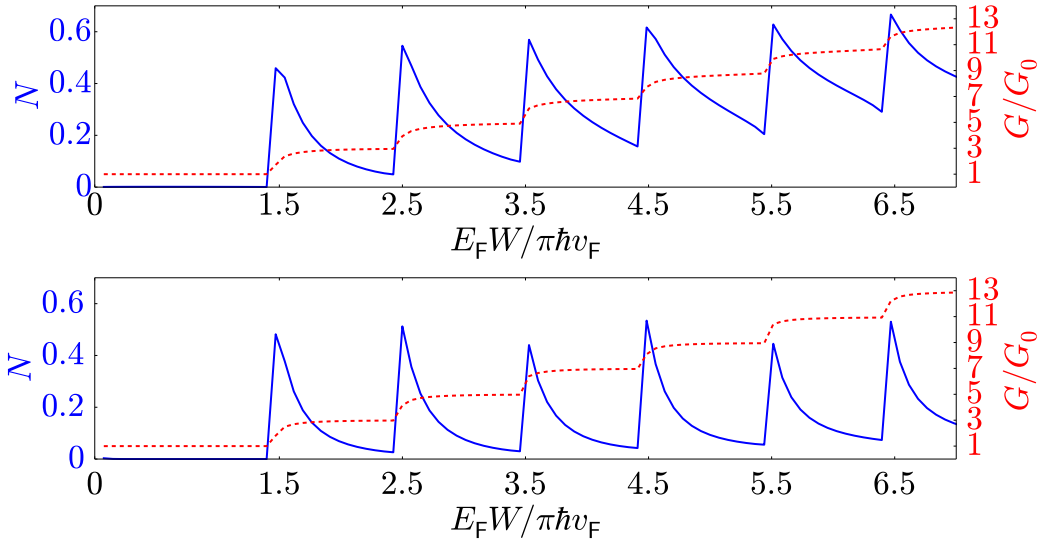

Figure 4.7.: We show the noise and conductance of a highly doped lead at $V_D = -1.1t$, which is connected by an impedance matching zone of length $L_{\mathsf{IM}} = 70a$ to a lead at energy E_{F}, whereas the width was chosen to $W = 100a$. The upper panel shows the results for a impedance matching profile, which drops linearly according to Eq. (4.3.9), whereas the lower panel shows the results for a profile following Eq. (4.3.6). The profile zone is tilted in the transversal dimension by an angle of $\pi/6$, to avoid the implementation of a transverse symmetry. The conductance steps in the transmission are due to the finite width, and are in accordance with Eq. (4.2.1). At every step, the noise increases drastically. However, for the reciprocal potential it reduces much quicker, and improves therefore the obtained conductance value in the simulation of high plateaus in accordance to the theoretically expected values.

intermediate region should sometimes be tilted by some angle with respect to the transport direction. Otherwise, the obtained conductance values might be wrong, as symmetry relations might suppress the propagation of some modes. We can use the condition (4.3.3) to derive a function for the transition from the high doping potential to the low energy potential of the system, which will reduce the impedance mismatch in an optimized way.

The doped potential is denoted by V_D and the energy within the system by V_E (both measured relative to the Dirac point). Using the dispersion relation between the energy and the wavelength, we obtain the relation

$$\frac{1}{2\pi}\lambda = \frac{\hbar v_{\mathsf{F}}}{V}. \tag{4.3.4}$$

We can solve the differential equation given by (4.3.3)

$$\frac{\mathrm{d}V}{\mathrm{d}x} = -\frac{\epsilon}{\hbar v_\mathsf{F}} V^2, \tag{4.3.5}$$

where we use $\epsilon \ll 1$. With the boundary conditions $V(0) = V_E$ and $V(L) = V_D$, we get

$$V(x) = \frac{V_E V_D L}{(V_E - V_D)x + V_D L}. \tag{4.3.6}$$

The condition (4.3.3) can be expressed in these parameters and states the length which should be chosen for a given potential difference, such that we have a good impedance matching

$$L \gg \frac{(V_E - V_D)\hbar v_\mathsf{F}}{V_E V_D}. \tag{4.3.7}$$

To estimate the quality of the impedance matching function, we can evaluate a clean two-terminal system, where the left lead is set at a high doping potential, and the right lead is set to energy E_F of the system. The leads are connected by a matching zone, where the potential drops from the doping down to the level of the system. We show in Fig. 4.7, the conductance of the system and the noise, which is defined by

$$N = \sum_n T_n(1 - T_n), \tag{4.3.8}$$

where T_n are the transmission probabilities of every mode. The potential of the lower panel follows Eq. (4.3.6) and the upper panel shows the simulated values for a linearly dropping potential

$$V(x) = V_E + (V_L - V_E)\frac{x}{L}. \tag{4.3.9}$$

The linear potential shows a worse behavior in the transmission of the modes compared to the more optimized reciprocal potential. The sixth mode does not reach the expected conductance value of $G = 13G_0$, which it does for the reciprocal profile. In following implementations with impedance matching zones, we will always use the reciprocal potential profile for the implementation.

4.4. Quantum Point Contact

As an example, we will discuss in a first step the transport simulation in a graphene quantum point contact (QPC) of width W simulated on a honeycomb lattice of spacing a. We additionally attach leads at a high doping with many propagating modes. In between the discussed system and the leads, we simulate an intermediate impedance matching region of length L_IM as described in Sect. 4.3. The lattice structure of the system is shown in Fig. 4.8. We cut out a part of a rectangular ribbon with zigzag edges in form of Gaussian functions to create the QPC. The standard deviation of the used Gaussian function is denoted by L_QPC and the minimum width is denoted by W_QPC. The constriction in the middle will determine

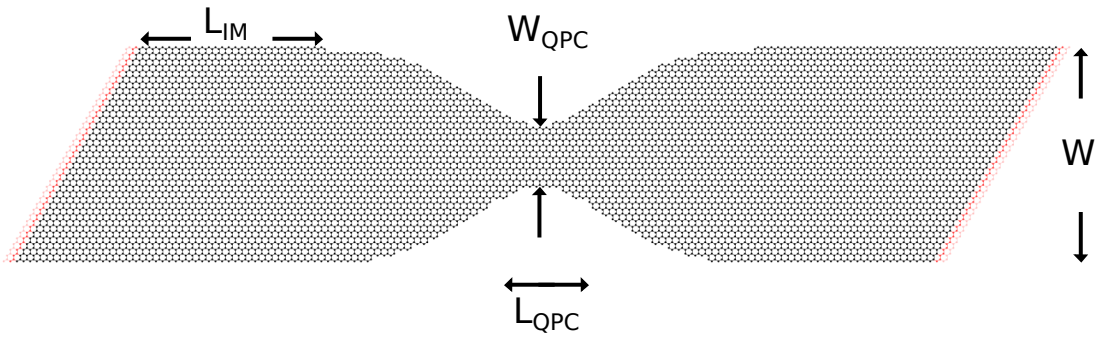

Figure 4.8.: Structure of the simulated quantum point contact. The structure is created by cutting out parts in form of a Gaussian functions from a rectangular piece. L_{QPC} corresponds to the standard deviation used for the Gaussian functions. The contact is connected to the highly doped leads by intermediate regions of length L_{IM} used for impedance matching. In the presented simulation we choose $W = 100a$, $W_{\mathrm{QPC}} = 20a$, $L_{\mathrm{QPC}} = 90a$ and $L_{\mathrm{IM}} = 50a$.

the number of modes that can pass the device. The length of the QPC needs to be chosen long enough such that restricted modes decay and can not pass it. Therefore, it should be longer than the corresponding Fermi wavelength of the propagating electrons. A good rule of thumb is to consider the wavelength of the first mode of the QPC using Eq. (4.2.1) and demanding that the length of the QPC is at least three times longer, which results in

$$L_{\mathrm{QPC}} > 4W_{\mathrm{QPC}}. \tag{4.4.1}$$

In Fig. 4.9, we see the calculated conductance for different Fermi energies of the system. For low energies, the simulated conductance rises stepwise at the values determined by Eq. (4.2.1). But this time with the width determined by the constriction of the contact. For higher energies the nice steps are not clearly simulated. The second step corresponds to an energy of $E_2 \approx 0.34t$ and therefore, we leave the low energy region of the tight binding dispersion. If we want to simulate more steps, the constriction needs to be simulated by more lattice points, which demands overall a larger system and thus more computational power.

4.5. Magnetic Fields

For further use, we want to discuss in this section which results are obtained if the methods of Sect. 3.2.2 and Sect. 3.3 are applied to the graphene system. We start with the analytical expectation for a constant magnetic field, which is added into the Hamiltonian of the Dirac equation via minimal coupling. The low energy dispersion relation of bulk graphene subjected to a magnetic field can be described by the Dirac equation

$$H = v_{\mathrm{F}}(\boldsymbol{p} + e\boldsymbol{A}) \cdot \boldsymbol{\sigma}. \tag{4.5.1}$$

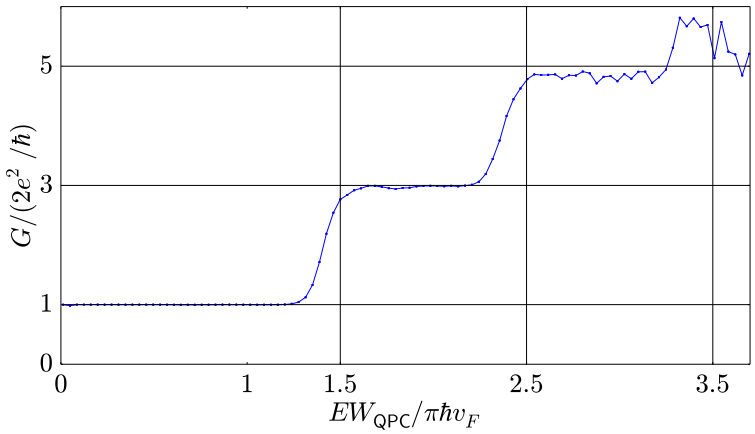

Figure 4.9.: Conductance of a quantum point contact system as described in Fig. 4.8. The system is connected to doped leads at a potential of $V_D = -1.1t$. The energy value of the simulated conductance steps can be clearly associated to the width of the constriction according to Eq. (4.2.1). The third step can no longer be well simulated as the corresponding energy becomes too large.

We can calculcate the spectrum of eigenvalues by squaring the Hamiltonian. Using that $\big(\boldsymbol{O}\cdot\boldsymbol{\sigma}\big)^2 = O^2$, for any operator $\boldsymbol{O}$ with $\big[O_i, O_j\big] = 0$, we can directly write

$$H^2 = v_{\mathrm{F}}^2(p^2 + e^2A^2 + ep_iA_j\sigma_i\sigma_j + eA_jp_i\sigma_j\sigma_i). \tag{4.5.2}$$

We choose for simplicity the Landau gauge $\boldsymbol{A} = -By\boldsymbol{e}_x$ to calculate the spectrum. Using $\sigma_i\sigma_j = i\epsilon_{ijk}\sigma_k$ the squared Hamiltonian reads

$$H^2 = v_{\mathrm{F}}^2\big[p_y^2 + \big(p_x - eBy\big)^2 - ieB\big(yp_y - p_yy\big)\sigma_z\big] \tag{4.5.3}$$

and results with $\big[y, p_y\big] = i\hbar$ in

$$H^2 = v_{\mathrm{F}}^2\big[p_y^2 + (p_x - eBy)^2 + e\hbar B\sigma_z\big]. \tag{4.5.4}$$

The first two terms correspond to the harmonic oscillator Hamiltonian (3.3.12), which was discussed for GaAs subjected to a magnetic field in Sect. 3.3. We only need to identify $v_{\mathrm{F}}^2 \leftrightarrow 1/2m$ and can copy the result, where we explicitly plug in the definition of the cyclotron frequency from Eq. (3.3.5). The additional constant Zeeman term in the Hamiltonian is of the same order in energy and we can summarize

$$H^2 = \hbar v_{\mathrm{F}}^2 eB\big(2n + 1 + \sigma_z\big). \tag{4.5.5}$$

Therefore, the energy levels of our free Dirac electrons in a magnetic field are given by

$$E_n = \hbar v_{\mathrm{F}}\sqrt{\frac{eB}{\hbar}2n}. \tag{4.5.6}$$

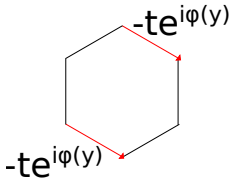

Figure 4.10.: Peierls substitution used on the honeycomb lattice that is in accordance with the translational for leads in the horizontal direction.

In contrast to the result of GaAs, we obtain a zero energy mode and the energy levels are proportional to the square root of the magnetic field.

In our numerical simulation we can implement the magnetic field again on the links of the lattice like we did in the case of GaAs. One difference is that the area enclosed by one plaquette of the honeycomb lattice is no longer $A = a^2$ like in the case of a square lattice, but $A_{\text{hex}} = \sqrt{3}a^2/2$ for a hexagon. Therefore the enclosed flux is given by $\Phi = \sqrt{3}Ba^2/2$. If we use the relation $\hbar v_{\text{F}} = \sqrt{3}at/2$ of our tight binding model for the Landau levels, we will expect them in the simulation at

$$E_n = t\sqrt{\sqrt{3}\frac{e}{\hbar}\Phi n}. \tag{4.5.7}$$

The flux can be implemented on the links via a Peierls substitution procedure as described in the Appendix A.3. In a practical implementation one can set the magnetic flux quantum to $\Phi_0 = 2\pi$ and thus $e/\hbar = 1$. To implement the constant magnetic field in a translational invariant manner for magnetic leads, which have a zigzag edge along the horizontal axis, we choose to modify only the hopping terms of the falling diagonals of one plaquette by $t \to te^{i\varphi(y)}$, as shown in Fig. 4.10. By choosing $\varphi(y) = 2\Phi ye/\sqrt{3}\hbar a$, where y is for example always the lower site of a link, an electron that hops around the plaquette one time will pick up a phase difference of $\Delta\varphi = \Phi e/\hbar$. The resulting dispersion relation is shown in Fig. 4.11. The magnetic length is defined as in Eq. (3.3.11) and is thus essentially given by

$$\frac{l_B^2}{A_{\text{hex}}} = \frac{1}{\Phi}\frac{\hbar}{e}. \tag{4.5.8}$$

If we zoom into the low energy region of the simulated dispersion relation, as shown in lower panel of Fig. 4.11, we can see that the appearance of new modes follow the expectation from Eq.(4.5.7). We trust the magnetic field to be simulated correctly as long $l_B \gg a$, which demands small fluxes Φ.

4.6. Aharonov-Bohm Effect

To simulate geometries that are more complex, we wrote a code with which we could read in arbitrary image files as blueprints and use the Python package kwant [8] to put a lattice model on top of it. We use it to analyze the Aharonov-Bohm effect in a graphene system.

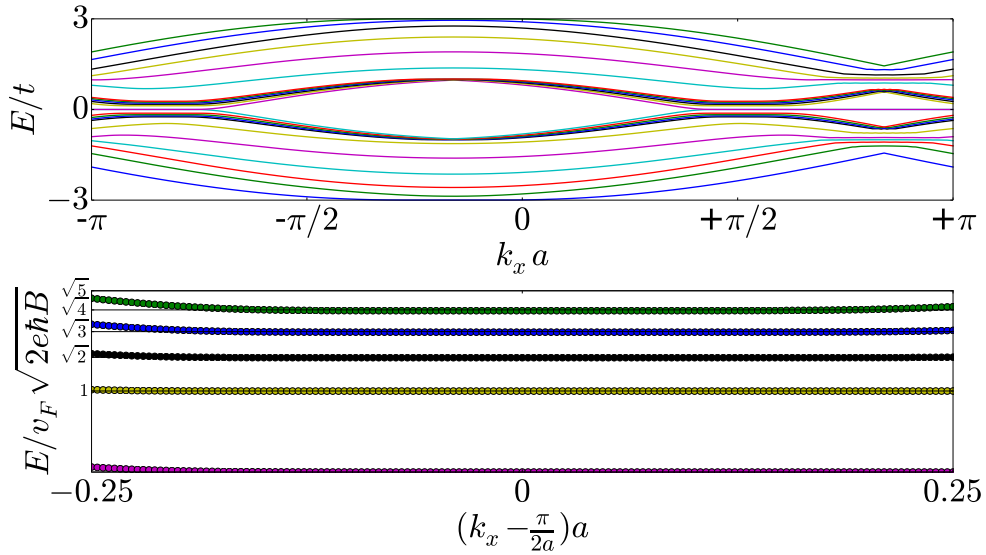

Figure 4.11.: Dispersion relation for a honeycomb tight binding model with an additional magnetic field. We simulate a system with zigzag edges, which has a width of $W = 100a$ and the magnetic field is characterized by $l_B = 10a$. The upper panel shows that the low energy modes follow a constant dispersion and that there are two regions with low energy modes resulting from the two cones. We show only every 20$^{\text{th}}$ higher energy mode for clarity. In the lower panel we zoom in around the middle of the low energy modes around $k_x = \pi/2a$. The appearance of new modes follows the expectation from Eq. (4.5.6).

For this purpose, we simulate a tight binding honeycomb lattice in a ring structure, as shown in Fig. 4.12. We measure the conductance in a four-terminal setup, which is explained in Sect. 2.7. In the Aharonov-Bohm setup, the electrons can travel either on the upper or lower path of the ring from one side to the other. As the device is subjected to a constant magnetic field B, a phase φ is acquired along each path, which is given by the line integral of the vector potential along the path

$$\varphi = \frac{e}{\hbar}\int_P \boldsymbol{A}\cdot \mathrm{d}\boldsymbol{x}. \tag{4.6.1}$$

The phase difference of the two paths corresponds to the flux enclosed by the ring (where we can use that $\mathrm{rot}\boldsymbol{A} = B$)

$$\Delta\varphi = \frac{e}{\hbar}BA_{\text{ring}}. \tag{4.6.2}$$

The acquired phase influences the transmission probability due to interference of the two paths, and therefore alter the measured conductance (for a detailed discussion see Ref. [7]). Thus, tuning the magnetic field will lead to observing an oscillatory behavior of the conductance. This has already been observed experimentally in ring structures made in metallic

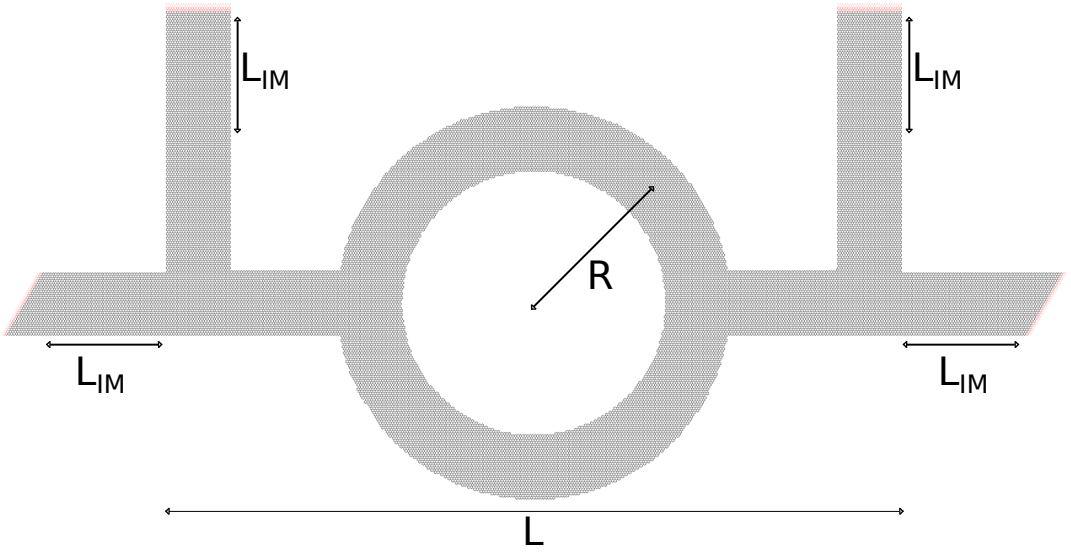

Figure 4.12.: Structure of the simulated Aharonov-Bohm ring in a four-terminal structure. A honeycomb lattice is used to simulate the graphene setup. The horizontal length of the system is set to $L = 300a$. This results in the geometry in an inner radius of $r_i = 54a$ and an outer radius of $r_o = 80a$. The mean radius from the center to the middle of the enclosing lead is therefore given by $R = 67a$. The leads are attached by impedance matching zones of length $L_{\mathsf{IM}} = 50a$. The width of the leads in this setup is $W = 26a$.

films, semiconducting heterostructures, or as well in graphene [35].

We measure the four-terminal conductance for a ring, which is enclosed by leads of finite-sized width, as we vary the magnetic field. Following the procedure of Sect. 2.7, the current is driven through the horizontal leads and the voltage difference is measured over the vertical leads. In the upper panel of Fig. 4.13, we see the simulated four-terminal conductance of the structure of Fig. 4.12 in units of $G_0 = 2e^2/\hbar$. The magnetic field was installed in the system and on the horizontal leads, as described in Sect. 4.5, on the falling diagonals of the honeycomb plaquettes. For the vertical leads, we need to put the acquired phase on the vertical links of the hexagons, to preserve the translational invariance. We can glue the area with the Peierls phase on the falling diagonals and the area with the phase on the vertical links, by inserting a transitional slice. Here, the phase coming from the the upper falling diagonal link is shifted on the vertical links. Any closed loop will therefore remain to give the right flux.

From the structure of Fig. 4.12, where we set the horizontal length to L, we read the mean radius of the ring R. Using that the corresponding enclosed area is given by $A_{\mathsf{ring}} = \pi R^2$,

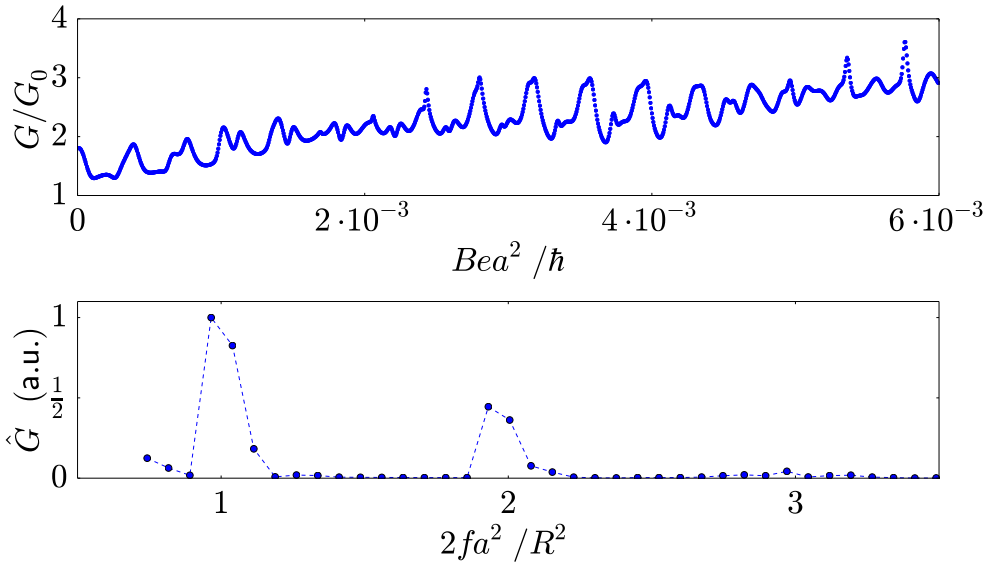

Figure 4.13.: The upper panel shows the conductance for the structure of Fig. 4.12 simulated for a range of magnetic field strenghs at $E_F = 0.3t$. Oscillations are visible, which show in the lower panel a distinct peak in the Fourier spectrum at the frequency associated to the area of the ring structure. Higher harmonics are also visible with lower amplitude. The transmission of $T \approx 2$–3 is due to the finite size constriction of the leads. To improve the visibility of the peaks in the spectrum, we cut off the lower frequencies.

we can write the phase difference along the upper and lower path as

$$\Delta\varphi = 2\pi\frac{e}{\hbar}a^2 B\frac{R^2}{2a^2}. \tag{4.6.3}$$

Therefore, if we vary B in units of $ea^2/\hbar$, we will expect a visible frequency in the Fourier spectrum at

$$f_0 = \frac{R^2}{2a^2}. \tag{4.6.4}$$

In a practical numerical implementation, we will set $e/\hbar = 1$ and $a = 1$. The lower panel of Fig. 4.13 shows the calculated Fourier spectrum of the conductance given in the upper panel in arbitrary units. It shows a peak around the frequency, corresponding to the mean radius of the lead. Furthermore, higher harmonics of the frequency are visible in the spectrum that decrease in intensity.

In a second study, we can modify the geometry to analyze a more complex device. We want to push the device into the quantum Hall regime, and still observe the Aharonov Bohm oscillations. As the current is carried over chiral edge modes, we have to add constrictions into the ring structure, such that interference paths become possible. For this purpose, we

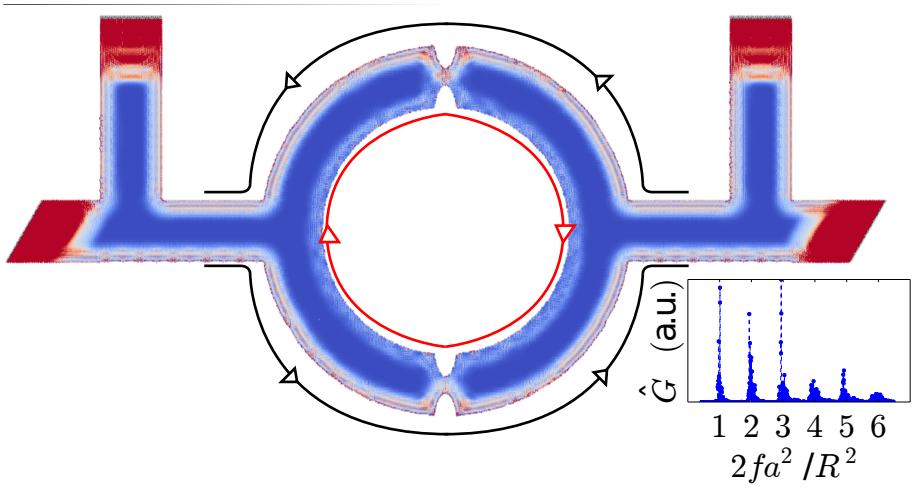

Figure 4.14.: We double the geometric parameters of the device in Fig. 4.12, and extend the structure by adding two sharp dents in the ring structure, such that edge modes can scatter from the outer to the inner ring and back. The electrons can either travel directly along the outer ring from one lead to the other (black curve), or they can perform loops along the inner ring inbetween (red curve). In the Fourier spectrum of the conductance (inset) distinct peaks are visible. The frequencies are determined by Eq. (4.6.4) by the inner ring radius plus a term in the order of the magnetic length, due to the finite extension of the edge states.

modeled a ring structure device, which has a sharp constriction in the upper and lower part of the ring. This means, we give the incoming edge states from the lead the possibility to scatter from the outer onto the inner ring, perform loops here and then scatter back onto the outer ring, and the possibilty to pass the constriction along the outer ring. Therefore, the paths can differ by multiple circumferences, which are determined by the inner ring radius plus the extension of the edge mode (essentially the magnetic length). Due to the suppressed backscattering in the edge modes of the quantum Hall effect, two constrictions are necessary, such that the transmission can be lowered in the quantum Hall regime.

In Fig. 4.14, we show the resulting total LDOS (as discussed in Sect. 2.9) for a device that is set onto the quantum Hall plateau corresponding to $\nu = 1$. The conductance, measured over a varied magnetic field on the said plateau, shows distinct oscillations, which can be characterized by the Fourier spectrum given in the inset of Fig. 4.14. We can again identify from the spectrum distinct peaks at a fundamental frequency $f_0 = r^2/2a^2$ and its higher harmonics. The obtained radius r from the fundamental frequency, is essentially given by the inner ring radius r_i of the device. Additionally, we have to account in r for the finite

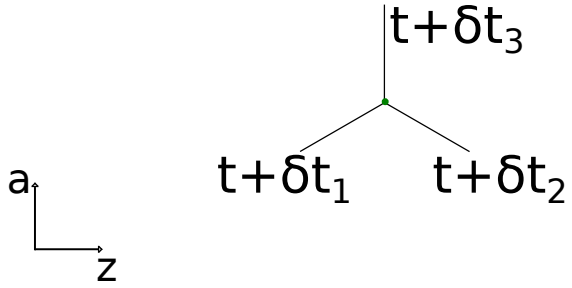

Figure 4.15.: To see the effect of strain on the transport for the low energy electrons, we change every particular hopping of the honeycomb lattice by δt_i. The three links for every respective site of sublattice A are enumerated as shown in the picture. The horizontal direction corresponds to a zigzag direction in the honeycomb lattice, whereas the vertical corresponds to a direction with an armchair edge.

extension of the edge states, which are in the order of the the magnetic length, as defined in Eq. (3.3.11).

The peaks in the Fourier spectrum of the conductance, which was measured in the quantum Hall regime, are less broad than the peaks obtained at lower magnetic fields (compare Fig 4.13), and we can resolve the higher harmonics with a much higher intensity. The first observation can be ascribed to the the fact that the magnetic length in this regime is much smaller than the width of the lead, and therefore the radius is essentially well determined by the inner ring radius. The second observation is due to the suppressed backscattering in the quantum Hall effect, and therefore the possibility to perform several loops before the disorder in the edge structure lowers the transmission.

4.7. Strain

In real experiments for graphene, one never deals with a perfect honeycomb lattice. Due to various reasons, one finds that the lattice sites may be displaced. For example, in experiments with suspended graphene (see Fig. 4.17) the lattice gets stretched due to an applied voltage between the sheet and the backgate. Or another example are ripples in the structure, which give rise to long-range disorder and also distort the lattice. In this section we want to discuss which effects deformations in the lattice have on the Dirac Hamiltonian and thus on the transport of the low-energy electrons.

Due to the deformation, the overlap of the p-orbital wavefunctions is changed. This results in a change of the individual hoppings in the honeycomb lattice by δt_i. This may be different for every respective link. The change can be estimated [36] by

$$\delta t_i = \frac{\beta t}{a_0^2} \boldsymbol{\delta}_i \cdot \big(\boldsymbol{u}_i - \boldsymbol{u}_0\big), \tag{4.7.1}$$

where $\boldsymbol{\delta}_i$ is defined in Eq. (4.1.3)–(4.1.5). In this linear approximation, we take the relative component of the displacement of the lattice site from the original position in direction of

the original link. The Grüneisen parameter

$$\beta \equiv \frac{\partial \log t}{\partial \log a_i} \tag{4.7.2}$$

relates the change of the nearest neighbor distance with the hopping parameter. It is approximately given in the linear regime by $\beta \approx 2$ [36]. We can relate the change of the hoppings to the components of the symmetric strain tensor from elasticity theory. For small displacements it is given by [37]

$$u_{ik} = \frac{1}{2}\left(\frac{\partial u_i}{\partial x_k} + \frac{\partial u_k}{\partial x_i}\right), \tag{4.7.3}$$

for the displacements u_z, u_a along the respective zigzag or armchair direction. For this purpose, we use the chain rule on the definition of the Grüneisen parameter given in Eq. (4.7.2). This can be written as[1]

$$\beta = \frac{\partial \log t}{\partial s_i}\frac{\partial s_i}{\partial \log a_i}, \tag{4.7.4}$$

where we introduced the differentials along the path of the links s_i, which are related to the armchair and zigzag directional derivatives in our lattice by

$$\frac{\partial}{\partial s_{1,2}} = \mp\frac{\sqrt{3}}{2}\frac{\partial}{\partial z} - \frac{1}{2}\frac{\partial}{\partial a}, \tag{4.7.5}$$

$$\frac{\partial}{\partial s_3} = \frac{\partial}{\partial a}. \tag{4.7.6}$$

The two derivatives for β can be evaluated separately. The paths are of length a_0 and therefore, we find in linear approximation for the first term that

$$\frac{\partial \log t}{\partial s_i} \approx \frac{1}{t a_0}\delta t_i. \tag{4.7.7}$$

For the second term, we have to evaluate the three possible displacements separately. We can write the displaced lattice vectors as

$$\boldsymbol{a}_{1,2} = a_0 \begin{pmatrix} \mp\sqrt{3}/2 \\ 1/2 \end{pmatrix} + \begin{pmatrix} u_z \\ u_a \end{pmatrix}, \tag{4.7.8}$$

$$\boldsymbol{a}_3 = a_0 \begin{pmatrix} 0 \\ 1 \end{pmatrix} + \begin{pmatrix} u_z \\ u_a \end{pmatrix}. \tag{4.7.9}$$

Their magnitudes are in linear approximation given by

$$a_{1,2} \approx a_0 \mp \tfrac{\sqrt{3}}{2}u_z - \tfrac{1}{2}u_a, \tag{4.7.10}$$

$$a_3 \approx a_0 + u_a. \tag{4.7.11}$$

[1] in this specific case no sum convention of any kind is implied, but three different possible forms are intended

Therefore, we can use the directional derivative along the links and the calculated magnitude of the displaced lattice vectors to evaluate the second term for β. Finally, we can solve for δt_i and get the relations

$$\delta t_{1,2} = \beta t\big(\tfrac{3}{4}u_{zz} + \tfrac{1}{4}u_{aa} \pm \tfrac{\sqrt{3}}{2}u_{za}\big), \tag{4.7.12}$$

$$\delta t_3 = \beta t u_{aa}, \tag{4.7.13}$$

where we used the definition of the strain tensor elements.

Furthermore, we can write the Hamiltonian from Eq. (4.1.10) for the changed hopping parameters as

$$H = \begin{pmatrix} 0 & -\sum_i t_i \exp\big(i\boldsymbol{k}\cdot\boldsymbol{\delta}_i\big) \\ -\sum_i t_i \exp\big(-i\boldsymbol{k}\cdot\boldsymbol{\delta}_i\big) & 0 \end{pmatrix}, \tag{4.7.14}$$

where $t_i = t + \delta t_i$. The first part of the three t_i terms results in the Dirac Hamiltonian of the unstrained lattice. The additional terms can be expanded around the K (or respective K') valley like in Sect. 4.1 with $\boldsymbol{k} = \boldsymbol{K} + \boldsymbol{q}$. We assume terms of order $\mathcal{O}\big(q\,\delta t\big)$ and $\mathcal{O}\big(q^2\big)$ to be negligible. This results in

$$-\sum_i \delta t_i \exp\big(i\boldsymbol{k}\cdot\boldsymbol{\delta}_i\big) \approx -\delta t_1\big(-\tfrac{1}{2} - i\tfrac{\sqrt{3}}{2}\big) - \delta t_2\big(-\tfrac{1}{2} + i\tfrac{\sqrt{3}}{2}\big) - \delta t_3 \equiv -\big(\tilde{A}_z - i\tilde{A}_a\big), \tag{4.7.15}$$

where we defined the pseudo-vector potential $\tilde{\boldsymbol{A}}$ by

$$\tilde{A}_z = \delta t_3 - \tfrac{1}{2}\big(\delta t_1 + \delta t_2\big), \tag{4.7.16}$$

$$\tilde{A}_a = \tfrac{\sqrt{3}}{2}\big(\delta t_1 - \delta t_2\big). \tag{4.7.17}$$

Using the relations for the hopping changes with the strain tensor given in Eq. (4.7.12) and Eq. (4.7.13), we obtain

$$\tilde{A}_z = \frac{\beta}{2a_0}\big(u_{aa} - u_{zz}\big), \tag{4.7.18}$$

$$\tilde{A}_a = -\frac{\beta}{a_0}u_{za}. \tag{4.7.19}$$

A pseudo-magnetic field can be associated with the pseudo-vector potential and is given by

$$\tilde{B} = \frac{\mathrm{d}}{\mathrm{d}z}\tilde{A}_a - \frac{\mathrm{d}}{\mathrm{d}a}\tilde{A}_z. \tag{4.7.20}$$

From these formulas, we can translate the strain of a lattice to a pseudo-vector potential. This can be used to perform transport simulations to analyze the expected effect in experiments.

For our discussion, the honeycomb lattice was fixed in a specific way in the lattice, having set the zigzag direction along the horizontal direction and the armchair along the vertical direction. In a next step we ask how the associated vector potential changes if the lattice is rotated. Meaning, we rotate the zigzag z- and armchair a-axis with respect to the horizontal

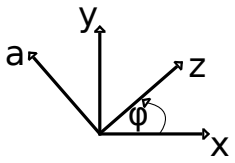

Figure 4.16.: For our discussion of the pseudo-vector potential, we always set the zigzag-direction of the lattice along the horizontal axis. We want to discuss how the pseudo-vector potential changes if the lattice is rotated by an angle ϕ.

x- and vertical y-direction, where the strain tensor is evaluated in, by some angle φ (see Fig. 4.16). This can be expressed by the rotation matrix

$$\boldsymbol{R} = \begin{pmatrix} \cos\varphi & \sin\varphi \\ -\sin\varphi & \cos\varphi \end{pmatrix}, \tag{4.7.21}$$

with which we get the strain tensor of the za-coordinate system from the xy-coordinate system via the transformation

$$\boldsymbol{u}^{(za)} = \boldsymbol{R}\boldsymbol{u}^{(xy)}\boldsymbol{R}^T. \tag{4.7.22}$$

Explicitly, this gives us the three equations

$$u_{zz} = u_{xx}\cos^2(\varphi) + u_{yy}\sin^2(\varphi) + u_{xy}\sin(2\varphi), \tag{4.7.23}$$
$$u_{aa} = u_{xx}\sin^2(\varphi) + u_{yy}\cos^2(\varphi) - u_{xy}\sin(2\varphi), \tag{4.7.24}$$
$$u_{za} = \tfrac{1}{2}\big(u_{yy} - u_{xx}\big)\sin(2\varphi) + u_{xy}\cos(2\varphi). \tag{4.7.25}$$

We can use the strain tensor in the za-coordinates to evaluate the vector potential in this system by Eq. (4.7.18) and (4.7.19), which results in

$$A_z = \frac{\beta}{2a_0}\Big[\big(u_{yy} - u_{xx}\big)\cos(2\varphi) - 2u_{xy}\sin(2\varphi)\Big], \tag{4.7.26}$$
$$A_a = \frac{\beta}{2a_0}\Big[\big(u_{xx} - u_{yy}\big)\sin(2\varphi) - 2u_{xy}\cos(2\varphi)\Big]. \tag{4.7.27}$$

This vector potential can now be rotated back into the xy-coordinate system, where we have to remember that the vector potential has to be rotated like the momentum

$$\boldsymbol{A}^{(xy)} = \boldsymbol{R}\boldsymbol{A}^{(za)}. \tag{4.7.28}$$

This results finally in

$$A_x = \frac{\beta}{2a_0}\Big[\big(u_{yy} - u_{xx}\big)\cos(3\varphi) - 2u_{xy}\sin(3\varphi)\Big], \tag{4.7.29}$$
$$A_y = \frac{\beta}{2a_0}\Big[-\big(u_{yy} - u_{xx}\big)\sin(3\varphi) - 2u_{xy}\cos(3\varphi)\Big]. \tag{4.7.30}$$

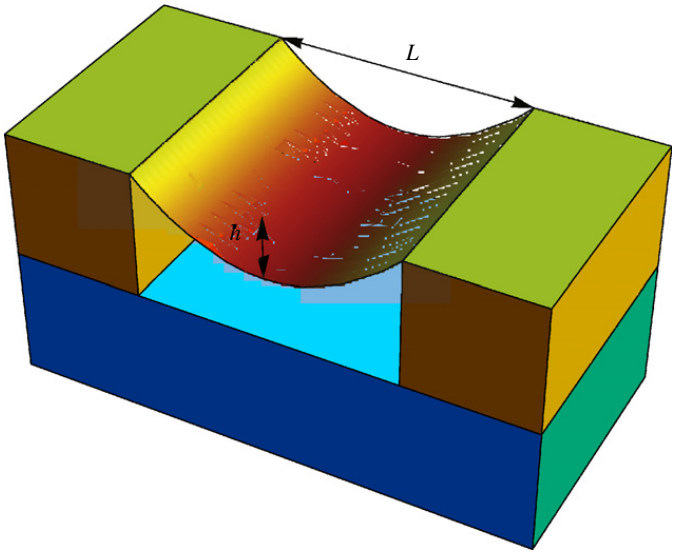

Figure 4.17.: Sketch of a suspended rectangular flake taken from [36]. Graphene sheets can be suspended by etching away the underlying substrate after having contacted the graphene sheet. We want to focus on the kinks at the interface to the contacts and estimate their effect on the transport properties.

The result we obtain is rotated by an angle of 3φ to the result we would expect if the honeycomb lattice is aligned with the zigzag direction along the x-direction. We can use this to consider for example a stretched system, which is translational invariant along y. Here the strain tensor has only a non-vanishing component in u_{xx}, which can be a function of x. In this case, we should put armchair edges (e.g. $\varphi = 30°$) along the x-direction to maximize the effect of the pseudo-potential. In this case, the cosine vanishes, whereas the sine is equal to one. Therefore, the calculated pseudo-magnetic field obtained by taking the curl of the pseudo-vector potential, which means that we have to take the derivative of A_y with respect to x, will be maximized. In contrast to this, a zigzag direction along the x-axis will result in a vanishing pseudo-magnetic field and the strain should show no effect.

4.8. Effect of a Kink

When we do an experiment with suspended graphene (Fig. 4.17), we notice that kinks are formed at the contact points. The kink in the lattice structure will result in a high strain at this contact point. In this section, we want to estimate the order of the pseudo-magnetic field associated with this kink. Using this estimation, we perform numerical simulations of the transport in a tight binding model, which contains the effect of the kink. We can ask whether in any real experiment, the kink should have a significant effect on the quantum Hall plateaus. We will also give a model to estimate the order of the pseudo-magnetic field in the suspended graphene sheet itself, and show that it is relatively small compared to the magnetic field induced by the kink. As a result, we will neglect in the simulation the pseudo magnetic

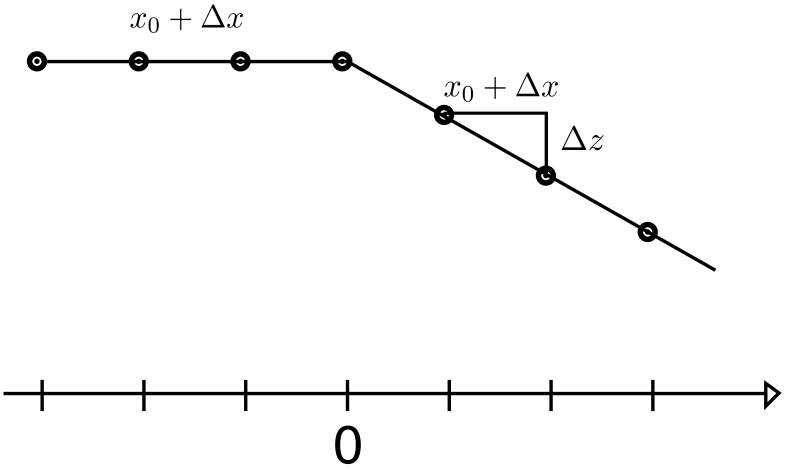

Figure 4.18.: To estimate the order of the pseudo-magnetic field associated with a kink in the structure, we suppose for simplicity that the lattice is translationally invariant in one dimension. Then, we suppose that somewhere in the one dimensional lattice chain there is a kink, which is given by some displacement Δz. The lattice is supposed to be homogenously prestretched by Δx in the model.

field in the sheet, and see that the angle corresponding to the kink that is needed to break the quantum Hall effect is out of a realistic physical range. From this, we will conclude that the kink has no major effect in the observation of the quantum Hall effect.

In the following, we look at a suspended sheet, which has a kink at the edge, which could be due to some applied voltage between a backgate and the sheet. For simplicity, the sheet is supposed to be invariant in the transversal y-direction. Thus, we start from a one-dimensional chain on discretized lattice sites in the x-direction. Every lattice site should already be homogenously displaced by Δx beforehand to account for some prestretching from the clamping. Now, we implement a kink on the lattice site by giving the sites some displacement Δz after $x = 0$ as displayed in Fig. 4.18.

The displacement coefficients in the transverse direction are all $u_y = 0$ due to the assumed symmetry. In the longitudinal direction they are given in front of the kink by the prestreching of the lattice

$$u_{\mathsf{fK}} = \Delta x, \tag{4.8.1}$$

and after the kink there is an additional streching in the z direction

$$u_{\mathsf{aK}} = \sqrt{(a_0 + \Delta x)^2 + \Delta z^2} - a_0 \approx \Delta x + \frac{a_0}{2}\frac{\Delta z^2}{a_0^2}. \tag{4.8.2}$$

We assume that $\Delta x, \Delta z \ll a_0$, where a_0 is the lattice constant. The angle of the kink is given by $\alpha = \Delta z / a_0$. For small angles, it can also be expressed by the length L of the sheet and the sagitta h of the bended curve by $\alpha \approx 2h/L$. In our kink model, the displacements in front of the kink are all the same, aswell as after the kink. Therefore, we obtain for the

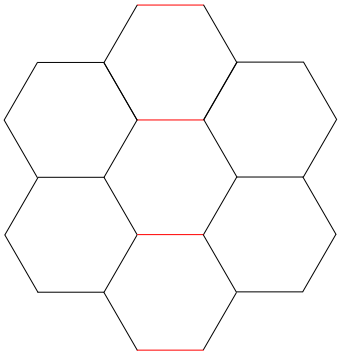

Figure 4.19.: To simulate the kink in the structure, we implement in the tight binding a pseudo-magnetic field only at a single strip of the structure. This is done by modifying the hopping on the red links by some value $\Delta t = \gamma t$

strain from the discretized derivative in between the lattice points only a result for the link right after the kink by

$$u_{xx} = \frac{u_{\mathsf{aK}} - u_{\mathsf{fK}}}{a_0} = \tfrac{1}{2}\alpha^2. \tag{4.8.3}$$

Consider x to be an armchair direction of graphene. Then, this strain at a single link will induce a pseudo-vector potential along this single link pointing into the zigzag-direction, as discussed in Sect. 4.7. From Eq. (4.7.18), we get

$$\tilde{A}_z = \frac{\beta}{4a_0}\alpha^2. \tag{4.8.4}$$

As the pseudo-vector potential is only nonzero in between the first grid points after the kink, the derivative with respect to x will give a pseudo-magnetic field contribution right at the kink, and a negative contribution of the same magnitude on the site right after the kink. The magnitude of the pseudo-magnetic field would be in the order

$$B = \frac{\mathrm{d}}{\mathrm{d}a}A_z = \frac{\beta}{4a_0^2}\alpha^2. \tag{4.8.5}$$

We can model this pseudo-magnetic field on a single link at the edge of a ribbon as indicated in Fig. 4.19. The scaled lattice is simulated with effective parameters $\tilde{a}$, $\tilde{t}$, where we demand

$$\hbar v_{\mathsf{F}} = \frac{3}{2}a_0 t = \frac{3}{2}\tilde{x}_0\tilde{t} \tag{4.8.6}$$

with $a_0 = 1.46\,\text{Å}$, $t = 2.8$ eV (see Sect. 4.3). We change the horizontal hoppings along a transverse slice by

$$\tilde{t} \to \tilde{t} + \gamma\tilde{t}. \tag{4.8.7}$$

Then, the pseudo-magnetic potential, which is connected to the changed horizontal hopping of the armchair plaquette, is in zigzag direction and given by

$$\tilde{A}_z = \frac{2}{3a_0}\gamma. \tag{4.8.8}$$

The generated pseudo-magnetic field around the kink would be given by

$$\tilde{B} = \frac{2}{3a_0^2}\gamma. \tag{4.8.9}$$

Comparing this with the result from (4.8.5), we obtain

$$\gamma = \tfrac{3}{8}\beta\alpha^2. \tag{4.8.10}$$

Now due to computational power restrictions, we can only simulate ribbons of finite width. To see how γ scales in the simulations, when the lattice discretization is changed, we numerically simulate the same physical system on two lattices, where the lattice constant of one is related to the other by $\tilde{a}' = 5\tilde{a}$. The simulations show that the effect of γ does not scale with the lattice size as can be seen in Fig. 4.20, and therefore $\tilde{A}_z$ scales only with the hopping $\tilde{t}$. This is not advantageous for our case. The γ values we obtain for our simulations are thus directly related to the value range of γ in the atomic basis, and therefore to the order of the angle.

This means for small physical angles $\alpha = \mathcal{O}(10^{-2})$ that we have to look at the results, which we obtain in our simulations for $\gamma = \mathcal{O}(10^{-4})$. Numerical simulations, which are also visible from Fig. 4.20, show that such a small γ has no effect, it would need to be in the order of $\gamma \approx \mathcal{O}(10^{-1})$ to break the quantum Hall effect. This is unphysical, as it would correspond to angles $\alpha \approx \mathcal{O}(20°)$, which is beyond any physical range for a atomic kink in a material.

We neglected in the simulation the pseudo-magnetic field, which is induced in the interior range due to the bending of the suspended graphene sheet. To justify this, we estimate the magnitude of this field, by extending the model to that of a hanging lattice chain. The total energy of the chain can be expressed by

$$E = \frac{k}{2}\sum_n u_{a,n}^2 + \sum_n V(z_n). \tag{4.8.11}$$

Here, $u_{s,n}$ is the displacement of the lattice sites along the direction of the sheet, which we assume further to be an armchair direction. It is essentially given by Eq. (4.8.2) with the addition that Δz depends now on s. Furthermore, we add some height dependent potential $V(z_n)$ (e.g. an applied electric field between the sheet and a backgate). Now, we make the continuum limit $a_0 \to 0$, and can rewrite the energy as

$$E = \int \mathrm{d}s\, \mathcal{L} + \text{const}, \tag{4.8.12}$$

where we defined

$$\mathcal{L} = \tfrac{1}{2}\tilde{k}\left(\frac{\mathrm{d}z}{\mathrm{d}s}\right)^2 + \tilde{V}(z). \tag{4.8.13}$$

The new coefficient for the spring constant relates to the old ones by $\tilde{k} = k\Delta s$ and the potentials are related by $\tilde{V} = V/a_0$. Stating that the energy should be stationary for a stable configuration implies that $\mathcal{L}$ fulfills the Euler-Lagrange equation

$$\frac{\mathrm{d}}{\mathrm{d}s}\frac{\partial \mathcal{L}}{\partial z'} = \frac{\partial \mathcal{L}}{\partial z}. \tag{4.8.14}$$

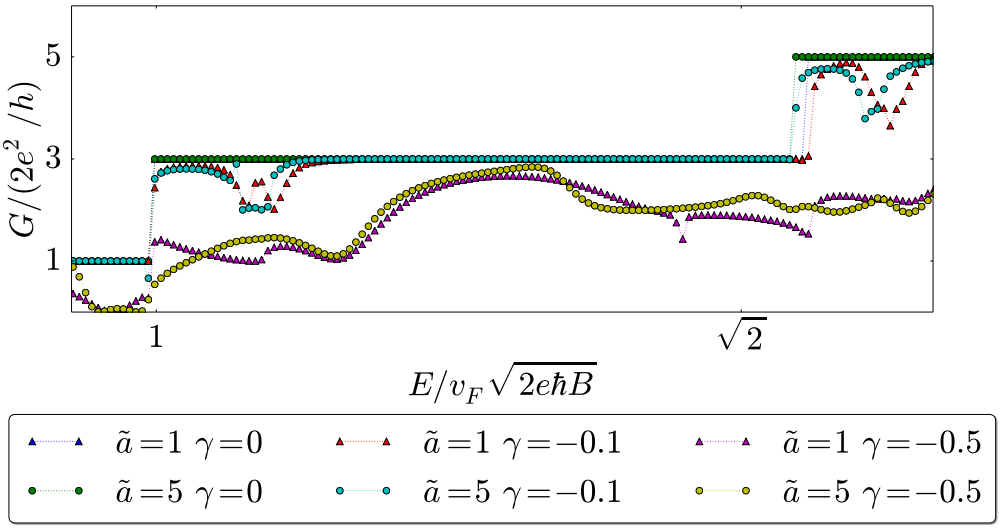

Figure 4.20.: Effect of γ simulated on two equivalent systems with different lattice constants $\tilde{a} = 1$ and $\tilde{a} = 5$. The numerical lattice constants remain fixed to $a = 1$ for both lattices, whereas we scaled the hopping t and applied magnetic flux Φ accordingly in the simulation. For $\tilde{a} = 1$, we choose $W = 200a$, $t = 1$ and $\Phi = 10^{-3}$. For $\tilde{a} = 5$ these correspond to $W = 40a$, $t = 0.2$ and $\Phi = 2.5 \cdot 10^{-2}$. The effect on the quantum Hall plateaus is approximately the same for both lattice constants and we conclude therefore that γ does not scale with a. The plot shows furthermore the first and second step of the QHE. We see that γ needs to be larger than $\gamma > 10^{-1}$ to break the QHE, which corresponds to angles in the kink which are unphysical, see Eq. (4.8.10). The higher steps for zero γ are shifted to the theoretical expectations due to the use of armchair edges in this case, see Sect. 4.2.

Which gives us the equation of motion

$$\tilde{k}z'' = \tilde{V}'. \tag{4.8.15}$$

For our case where $V(z)$ is independent of s, we get the conserved quantity

$$\epsilon = \tfrac{1}{2}\tilde{k}z'^{\,2} - \tilde{V}(z). \tag{4.8.16}$$

This can be solved for $z'^{\,2}$ and thus gives us an expression for the displacement using Eq. (4.8.2)

$$u_s = \Delta s + \frac{a_0}{\tilde{k}}\big(\epsilon + \tilde{V}\big). \tag{4.8.17}$$

The first two terms are independent of z. Therefore, we obtain for the strain along the sheet direction of the lattice

$$u_{ss} = \frac{a_0}{\tilde{k}}\tilde{V}'(z)\, z'(s). \tag{4.8.18}$$

As we assume that the sheet direction s is an armchair direction, the pseudo-magnetic field is only given in the zigzag direction by

$$\tilde{A}_z = \frac{\beta}{2\tilde{k}} \tilde{V}' \, z'. \tag{4.8.19}$$

The corresponding pseudo-magnetic field of the bulk is therefore given by

$$\tilde{B}_{\text{bulk}} = \frac{\beta}{2\tilde{k}^2} \Big(2\epsilon \tilde{V}'' + (\tilde{V}^2)'' - \tilde{V}' \Big). \tag{4.8.20}$$

Let us assume for example that $\tilde{V}(z) \sim z$. In this case the bulk magnetic field is simply given by the constant term

$$\tilde{B}_{\text{bulk}} = \frac{\beta}{2\tilde{k}^2} \left(\frac{\tilde{V}(z)}{z} \right)^2. \tag{4.8.21}$$

Using the conserved quantity ϵ, this can be rewritten in terms of the angle α of the sheet and the sagitta h. In this form, we have

$$\tilde{B}_{\text{bulk}} = \frac{\beta \alpha^4}{8h^2}. \tag{4.8.22}$$

Compared to the result, which we got for the estimation of the pseudo-magnetic field at the kink in Eq. (4.8.5), we see that

$$\frac{\tilde{B}_{\text{bulk}}}{\tilde{B}_{\text{kink}}} = \frac{a_0^2 \alpha^2}{2h^2}. \tag{4.8.23}$$

Now as the sagitta $h > a_0$ and especially $\alpha \ll 1$, we see that the pseudo-magnetic field in the bulk should be orders of magnitude smaller than the one generated at the kink. This justifies, why we neglected it completely in the simulation of the quantum Hall effect in the system with a kink.

4.9. Staggered Fermion Model

Another source for strain in the lattice could be due to long-range disorder. A source for the disorder might be ripples in the structure. To describe the effect of long-range disorder on the electronic transport of graphene, we have to choose another model. We can not use the described onsite disorder in the nearest neighbor model of the honeycomb lattice as it couples the two corners of the Brillouin zone via intervalley scattering. In the case of long-range disorder, the scattering processes should only couple by small k values, and therefore we only want to describe intravalley scattering within a single Dirac cone. One way to achieve this would be by simulating very large lattice structures and simulating explicitly long-range correlated disorder. This is highly expensive on the side of computational power. Another way, which we intend to pursue, is to choose a model that simulates only a single Dirac cone. Therefore, onsite disorder will couple only the states within the single cone and the model should represent the effects of long-range scattering.

For this, we will use the staggered fermion model, which is presented in Ref. [38]. Here, the Dirac Hamiltonian is discretized explicitly and solved directly for an transfer matrix. Special care is necessary in the discretization, as a naive approach leads either to a non Hermitian Hamiltonian or fermion doubling [39]. Furthermore, we will extend the model of Ref. [38] by adding a vector potential. As we show in A.6, the standard approach of introducing the magnetic field by a gauge transformation fails at this point. Therefore, we resort to explicitly discretizing also the vector potential, which is introduced via minimal coupling substitution. This approach was also presented in a different way in [40]. But the presented current operator in this approach is not suitable to rotate the transfer matrix into the basis of modes carrying unit flux, and to evaluate the associated scattering matrix.

The complete Hamiltonian, which we want to discuss, is given by

$$H = -i\hbar v_{\mathsf{F}} \left[\sigma_x \left(\partial_x - i\frac{e}{\hbar} A_x \right) + \sigma_y \left(\partial_y - i\frac{e}{\hbar} A_y \right) \right] + U(\boldsymbol{r}). \tag{4.9.1}$$

In the same manner as described in Ch. 2, we want to solve the eigenvalue equation $H\Psi = E\Psi$, and obtain the solution in form of a scattering matrix to discuss the transport properties. In the presented scheme, this will be achieved by slicing the system, calculating the transfer matrices for each slice, transforming these to scattering matrices, and finally composing them to the complete system scattering matrix. From this matrix, we can extract the transmission probability, and therefore calculate the conductance of the system.

We can rewrite the eigenvalue equation as

$$\partial_x \Psi = \left(-i\sigma_z \partial_y - i\sigma_x V(\boldsymbol{r}) + i\frac{e}{\hbar} \mathbb{1} A_x - \frac{e}{\hbar} \sigma_z A_y \right) \Psi, \tag{4.9.2}$$

where we introduced $V(\boldsymbol{r}) = (U(\boldsymbol{r}) - E)/\hbar v_{\mathsf{F}}$. We evaluate the derivatives by finite differences on a lattice that is displaced symmetrically from the original lattice as depicted in Fig. 4.21. This discretization procedure avoids fermion doubling, which normally results from the doubling of the lattice spacing in finite differences [39]. The differential operators are thus discretized on the spots marked by the crosses in Fig. 4.21 by

$$(\partial_x \Psi)_\times \to \frac{1}{2\Delta} (\Psi_{m+1,n} + \Psi_{m+1,n+1} - \Psi_{m,n} - \Psi_{m,n+1}), \tag{4.9.3}$$

$$(\partial_y \Psi)_\times \to \frac{1}{2\Delta} (\Psi_{m,n+1} + \Psi_{m+1,n+1} - \Psi_{m,n} - \Psi_{m+1,n}). \tag{4.9.4}$$

Furthermore the potential terms are also evaluated on the crosses by taking the mean value

$$(V\Psi)_\times \to \frac{1}{4} V_{m,n} (\Psi_{m+1,n} + \Psi_{m+1,n+1} + \Psi_{m,n} + \Psi_{m,n+1}), \tag{4.9.5}$$

where $V_{m,n} = V(x_m + \Delta/2, y_n + \Delta/2)$ is the potential value at the crossed position. Taking the same potential value for all four points is necessary to ensure that the following corresponding matrix is Hermitian, which will help to find the current operator of the model. The analogue of $V\Psi$ is done for $A_x\Psi$ and $A_y\Psi$.

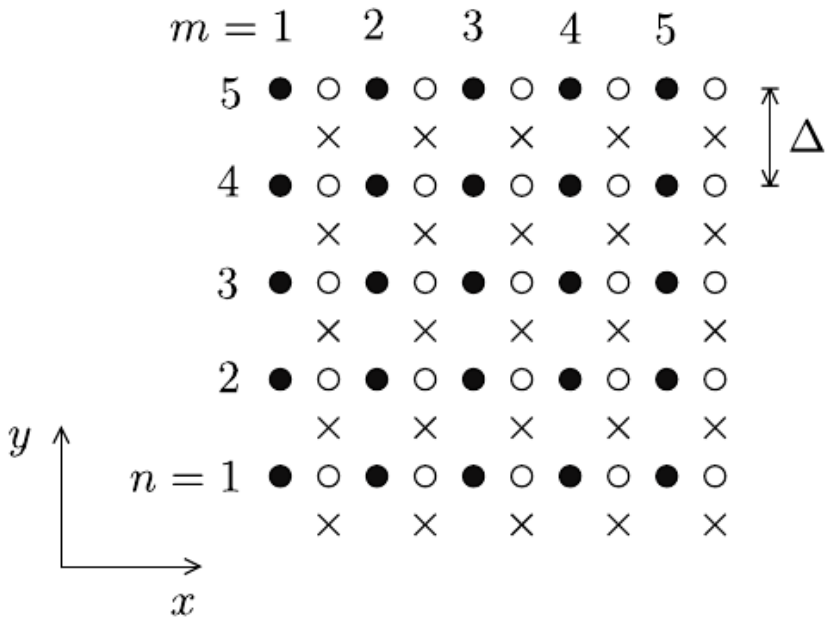

Figure 4.21.: The wavefunction $\Psi_{m,n}$ is evaluated on discretized lattice sites, which are noted by filled circles. The finite differences are evaluated on the crosses as denoted by Eq. (4.9.3) and Eq. (4.9.3). The Dirac equation is finally evaluated on the empty cirlces by taking the mean of the adjacent sites. This discretization procedure avoids fermion double by paying the price that the model becomes non-local. The figure is taken from Ref. [38].

The Dirac equation is evaluated at the empty circles in between the crosses by taking the mean value of adjacent sites. With Ψ_m, a vector containing N spinors for the slice at position m, we obtain for the derivatives at the position of the empty circles

$$(\partial_x \Psi)_\circ \to \frac{1}{2\Delta} \mathcal{J}(\Psi_{m+1} - \Psi_m), \tag{4.9.6}$$

$$(\partial_y \Psi)_\circ \to \frac{1}{2\Delta} \mathcal{K}(\Psi_{m+1} + \Psi_m). \tag{4.9.7}$$

The tridiagonal $N \times N$ matrices $\mathcal{J}, \mathcal{K}$ have the non-zero elements

$$\begin{aligned} \mathcal{J}_{n,n} &= 1, && (4.9.8)\\ \mathcal{J}_{n,n+1} &= \tfrac{1}{2}, && (4.9.9)\\ \mathcal{J}_{n,n-1} &= \tfrac{1}{2}, && (4.9.10)\\ \mathcal{K}_{n,n+1} &= \tfrac{1}{2}, && (4.9.11)\\ \mathcal{K}_{n,n-1} &= -\tfrac{1}{2}. && (4.9.12)\\ & && (4.9.13) \end{aligned}$$

For the potential on the empty circles

$$(V\Psi)_\circ \to \frac{1}{4}\mathcal{V}^{(m)}(\Psi_{m+1}+\Psi_m), \tag{4.9.14}$$

we have the matrix structure

$$\begin{aligned}
\mathcal{V}^{(m)}_{n,n} &= \tfrac{1}{2}(V_{m,n}+V_{m,n-1}), && (4.9.15)\\
\mathcal{V}^{(m)}_{n,n+1} &= \tfrac{1}{2}V_{m,n}, && (4.9.16)\\
\mathcal{V}^{(m)}_{n,n-1} &= \tfrac{1}{2}V_{m,n-1}. && (4.9.17)\\
& && (4.9.18)
\end{aligned}$$

Analogously, we define the matrices $\mathcal{A}_x^{(m)}$ and $\mathcal{A}_y^{(m)}$. If we apply periodic boundary conditions in the y-direction, the indices $n\pm1$ have to be evaluated modulo N. We notice that the matrices $\mathcal{J},\mathcal{V}^{(m)},\mathcal{A}_x^{(m)},\mathcal{A}_y^{(m)}$ are Hermitian and $\mathcal{K}^\dagger=-\mathcal{K}$. The eigenvalues of $\mathcal{J}$ and $\mathcal{K}$ are given in [38]. They suggest that the number of lattice sites N in the transverse direction should be odd, such that $\mathcal{J}$ is always invertible. The discretized Dirac equation evaluated on the empty circles reads

$$\frac{1}{2\Delta}\mathcal{J}\Big(\Psi_{m+1}-\Psi_m\Big)=\left(-\frac{i}{2\Delta}\sigma_z\mathcal{K}-\frac{i}{4}\sigma_x\mathcal{V}^{(m)}+i\frac{q}{4\hbar}\Big[\mathcal{A}_x^{(m)}+i\sigma_z\mathcal{A}_y^{(m)}\Big]\right)\Big(\Psi_{m+1}+\Psi_m\Big). \tag{4.9.19}$$

Rearranging this equation gives

$$\begin{aligned}
&\left(\mathcal{J}+i\sigma_z\mathcal{K}+i\frac{\Delta}{2}\sigma_x\mathcal{V}^{(m)}-i\frac{e\Delta}{2\hbar}\Big[\mathcal{A}_x^{(m)}+i\sigma_z\mathcal{A}_y^{(m)}\Big]\right)\Psi_{m+1}= && (4.9.20)\\
&\qquad\left(\mathcal{J}-i\sigma_z\mathcal{K}-i\frac{\Delta}{2}\sigma_x\mathcal{V}^{(m)}+i\frac{e\Delta}{2\hbar}\Big[\mathcal{A}_x^{(m)}+i\sigma_z\mathcal{A}_y^{(m)}\Big)\right)\Psi_m.
\end{aligned}$$

By defining

$$X_m=\sigma_z\mathcal{K}+\frac{\Delta}{2}\sigma_x\mathcal{V}^{(m)}-\frac{e\Delta}{2\hbar}\Big(\mathcal{A}_x^{(m)}+i\sigma_z\mathcal{A}_y^{(m)}\Big), \tag{4.9.21}$$

the equation shortens to

$$(\mathcal{J}+iX_m)\Psi_{m+1}=(\mathcal{J}-iX_m)\Psi_m. \tag{4.9.22}$$

The transfer matrix of a slice, which relates $\Psi_{m+1}=M_m\Psi_m$, is then given by

$$M_m=(\mathcal{J}+iX_m)^{-1}(\mathcal{J}-iX_m), \tag{4.9.23}$$

which can be calculated numerically. As we already noted in Sect. 2.4 the composition of transfer matrices is numerically unstable. Therefore, we calculate for each slice the associated scattering matrix. Before we can do this, we need to make sure that the given transfer matrix is given within the basis of wavefunctions that are normalized to unit flux. Thus, we need the current operator of the model. The yet to determined current operator J_x should fulfill the current conservation condition

$$\langle\Psi_{m+1}|\,J_x^{(m+1)}\,|\Psi_{m+1}\rangle=\langle\Psi_m|\,J_x^{(m)}\,|\Psi_m\rangle\,. \tag{4.9.24}$$

In general the current operator could be different for every slice and could just be calculated consecutively from this condition. But for a true increase in numerical accuracy, the current operator should be of a known form and thus more simple. Therefore, we demand that the current operator is the same for all slices. The current conservation condition

$$M_m^\dagger J_x M_m = J_x \tag{4.9.25}$$

can be rewritten, by using the form of the transfer matrix from Eq. (4.9.23), to

$$J_x^{-1} X_m^\dagger \mathcal{J}^{-1} J_x = \mathcal{J}^{-1} X_m. \tag{4.9.26}$$

Moreover, we can use that $\sigma_x\sigma_z\sigma_x = -\sigma_z$ and $\sigma_x^2 = \mathbb{1}$ to find $X_m^\dagger = \sigma_x X_m \sigma_x$. Thus,

$$\mathcal{J} J_x^{-1} \sigma_x X_m \sigma_x \mathcal{J}^{-1} J_x = X_m. \tag{4.9.27}$$

Using this equation, we see that the current conservation is always given for $J_x = \alpha\sigma_x\mathcal{J}$. The constant is fixed from the continuum limit of the current operator $(j_x, j_y) = v(\sigma_x, \sigma_y)$ [38]. Therefore, the current operator is given by

$$J_x = \tfrac{1}{2} v \sigma_x \mathcal{J}. \tag{4.9.28}$$

To obtain the unitary scattering matrix from the transfer matrix, we need to transform the transfer matrix, such that the currents are just ± 1. This means, we need to calculate

$$\tilde{M}_m = R M_m R^{-1}, \tag{4.9.29}$$

such that

$$\tilde{M}_m^\dagger \begin{pmatrix} \mathbb{1} & 0 \\ 0 & -\mathbb{1} \end{pmatrix} \tilde{M}_m = \begin{pmatrix} \mathbb{1} & 0 \\ 0 & -\mathbb{1} \end{pmatrix}. \tag{4.9.30}$$

Therefore, the transformation matrix R should fulfill the equation

$$R^\dagger \begin{pmatrix} \mathbb{1} & 0 \\ 0 & -\mathbb{1} \end{pmatrix} R = \sigma_x \mathcal{J}. \tag{4.9.31}$$

This can be satisfied by

$$R = \sigma_H \mathcal{J}^{1/2}, \tag{4.9.32}$$

where σ_H is the Hadamard matrix

$$\sigma_H = \frac{1}{\sqrt{2}} \begin{pmatrix} 1 & 1 \\ 1 & -1 \end{pmatrix}. \tag{4.9.33}$$

For numerical evaluations, it is advised to use the Cholesky decomposition of J for the calculation of R.

Using the transformed transfer matrix of Eq. (4.9.29) for each slice, we can calculate the respective scattering matrices by Eq. (2.4.11)–(2.4.14). The unitary matrices of the slices can be added via the composition rules, as noted in A.1.9, to the scattering matrix of the complete system. From this, we obtain the transmission probabilities, which relate to the

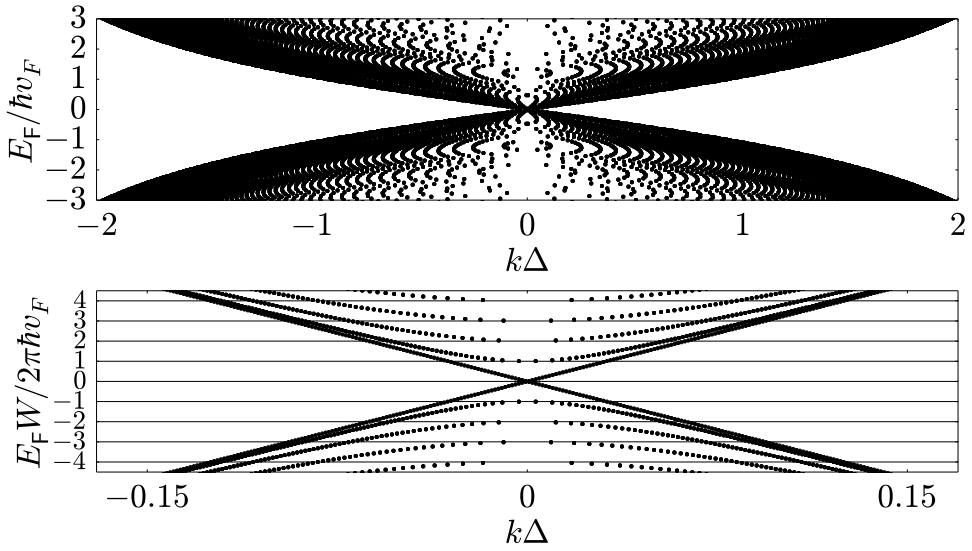

Figure 4.22.: The upper panel shows the dispersion relation of a clean system simulated in the staggered fermion model. Herefore, we show the phase of the propagating modes for different energy values. The width of the system with periodic boundary conditions was chosen to be $W = 201\Delta$. In the lower panel, we zoom to the low energy modes. We see that they asymptotically follow the Dirac dispersion. New modes appear whenever the energy is greater than the levels determined due to the periodic boundary conditions from Eq. (4.9.34). An inspection of the data shows furthermore that every mode $|n| > 0$ is doubly degenerate. .

conductance, as described in 2.7. As described in [38], a filter zone in front and after the system should be added, which lies at a high energy, to eradicate spurious evanescent modes.

For a first check, we show that the model really simulates the single Dirac cone. For this purpose, we do not include any magnetic field or any kind of disorder. The potential is held at a constant value within the system $U(\boldsymbol{r}) = E_\mathsf{F}$, which determines the Fermi energy relative to the Dirac point. For the numerical implementation, we set $\Delta = 1$ and $\hbar v_\mathsf{F} = 1$ to determine the length and energy scale.

From the transfer matrix of a single slice of the system, we can plot the dispersion relation of the propagating modes. Therefore, we evaluate the phase k of the propagating eigenvalues $\lambda = \exp(ik\Delta)$ from the transfer matrix for different energies. As we see in Fig. 4.22, the modes follow asymptotically the dispersion of a single Dirac cone. New modes appear due to the periodic boundary conditions, whenever the energy is greater than

$$E_n = \hbar v_\mathsf{F} \frac{2\pi}{W} n \tag{4.9.34}$$

for an integer n. Furthermore, the data shows that every mode $|n| > 0$ is doubly degenerate, which is also due to the periodic boundary conditions. This degeneracy can also be seen

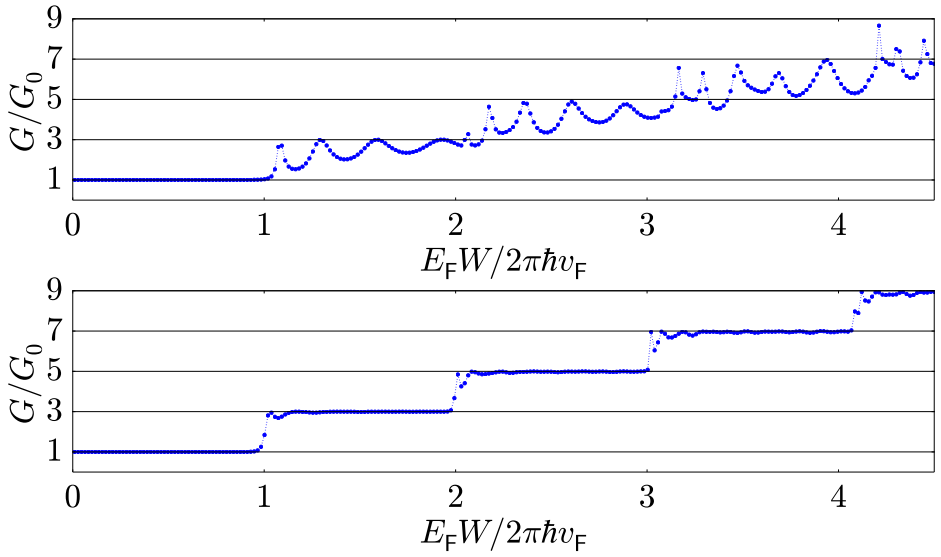

Figure 4.23.: The upper panel shows the conductance of clean system of length $L = 50\Delta$ and width $W = 41\Delta$, which is directly connected to the leads. The Fabry-Perot like oscillations are due to the high impedance mismatch between the system and the leads. In the lower panel, we added additional impedance matching zones of length $L_{\mathrm{IM}} = 50\Delta$ in front and after the same system, which effectively reduces the Fabry-Perot oscillations. The high doping potential is set to $V_{\mathrm{D}} = 3\hbar v_{\mathrm{F}}/\Delta$. Due to the periodic boundary conditions the conductance rises stepwise by two conductance quanta $G_0 = 4e^2/h$.

in Fig. 4.23, where we show the corresponding simulated conductance of a clean staggered fermion system. Here the quantum of conductance is $G_0 = 4e^2/h$ to account for the valley and spin degeneracy, which is not actively simulated. At every step the conductance jumps by two quanta of conductance, due to the double degeneracy of the modes.

In the upper panel of Fig. 4.23, we notice at first glance oscillations in the transmission. These are Fabry-Perot oscillations that are due to the high impedance mismatch between the system and the leads, therefore the oscillation frequency also increases with the length of the system. The mismatch is a result from the construction of the model, where the leads are set to a very high doping relative to the Dirac point, whereas the simulated system itself is set at a relatively low energy. To get rid of these oscillations, we insert in front and after the system impedance matching zones, which we described in Sect. 4.3. In the lower panel of Fig. 4.23, we show the same system with the additional impedance matching zones.

In the next step we include a constant magnetic field perpendicular to the lattice. For this purpose, we choose the Landau gauge $A_x = -By$, $A_y = 0$. Using $y_n = n \cdot \Delta$, the evaluation of the vector potential A_x at the crossed positions of the lattice is given by $(A_x)_{m,n} = -B\Delta(n + \frac{1}{2})$. The matrix used to implement the constant magnetic field in the

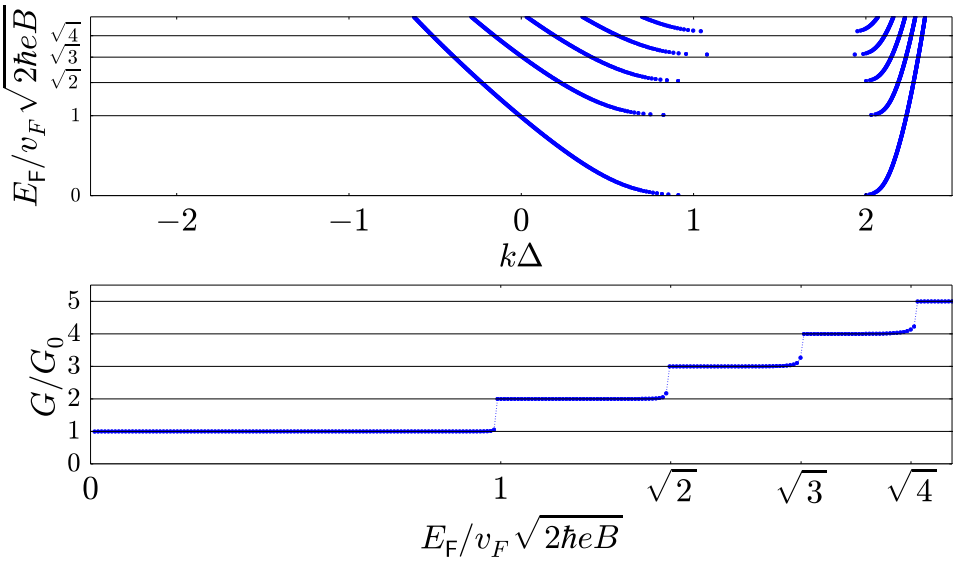

Figure 4.24.: The upper panel shows the dispersion relation for a staggered fermion model of width $W = 41\Delta$ subjected to a magnetic field of $B = 0.1\hbar/e\Delta^2$. As far as our numerical resolution allows it, we see the constant dispersion due to the quantum Hall effect and the typical upbending of the dispersion due to the boundary. The lower panel shows the associated conductance calculated in a system oflength $L = 50\Delta$. Additionally, impedance matching zones of length $L_{\mathsf{IM}} = 50\Delta$ were added in front and after the system.

numerical evaluation of the Dirac equation is therefore given by

$$\mathcal{A}_x^{(m)} = -B\Delta \begin{pmatrix} 0 & \frac{1}{4} & & & \\ \frac{1}{4} & 1 & \frac{3}{4} & & \\ & \frac{3}{4} & 2 & \frac{5}{4} & \\ & & \frac{5}{4} & 3 & \ddots \\ & & & \ddots & \ddots \end{pmatrix}. \tag{4.9.35}$$

The resulting dispersion relation and conductance for the system, which is subjected to a constant magnetic field, is shown in Fig. 4.24. For the numerical evaluation, we set $e/\hbar = 1$, which corresponds to setting the magnetic flux quantum to $\Phi_0 = 2\pi$. We can clearly see the conductance steps at the energies of the anomalous quantum hall effect, which were given by Eq. (4.5.6). In the system used to simulate the conductance, we again implemented impedance matching zones at the boundaries of the system to reduce Fabry-Perot oscillations. Furthermore, we chose the magnetic field again large enough such that the number of modes due to the boundary constrictions is always higher than the number of modes due to the quantum Hall effect.

Now it is necessary for our analysis of the effect of long-range disorder on the quantum Hall plateaus of graphene to actually implement disorder in the model. For example, a substrate which supports a graphene layer could induce forces on the carbon atoms, which results in strains and deformations. We can thus assume a random distribution of forces within the graphene layer, that varies only slowly over the long distance ξ. We assume that the lattice site distant Δ of the staggered fermion model is given by the correlation length of the long-range disorder $\Delta \approx \xi$. For the numerical evaluation this length scale will be set to $\Delta = 1$. According to Sect. 4.7, the random distribution of strains and displacement should result in a randomly distributed pseudo vector potential. We choose the distribution to be gaussian with a variance of α^2, and therefore

$$\langle \tilde{A}^{(x)}_{m,n} \tilde{A}^{(x)}_{m',n'} \rangle = \alpha^2 \delta_{m,m'} \delta_{n,n'}, \tag{4.9.36}$$

$$\langle \tilde{A}^{(y)}_{m,n} \tilde{A}^{(y)}_{m',n'} \rangle = \alpha^2 \delta_{m,m'} \delta_{n,n'}. \tag{4.9.37}$$

As the disorder is implemented on the onsite terms, we can use the results from Sect. 3.2.1 to estimate the corresponding mean free path. Using $\hbar v_\mathsf{F} = 1$ in the density of states from Eq. (A.4.5), the Born approximation result gives for the onsite disorder in the staggered fermion model

$$l = \frac{1}{\alpha^2 k_\mathsf{F}}, \tag{4.9.38}$$

where the mean free path is measured in units of Δ. This on the other hand means that the conductivity in the diffusive limit, which was given by Eq. (3.2.25), is determined independent of the Fermi energy by

$$\sigma = G_0 \frac{1}{2\alpha^2}. \tag{4.9.39}$$

In Fig. 4.25, we show ensemble averaged data for the conductivity of systems simulated at different disorder strengths α. The two-dimensional conductivity is equal to the conductance, as the shown conductance is simulated for systems with fixed aspect ratio $W/L = 1$. We see that for increasing system size, the conductivity approaches for systems with $k_\mathsf{F} l \gg 1$ the diffusive value estimated by the Born approximation in Eq. (4.9.39).

From the number of propagating modes N, which can be estimated from Eq. (4.9.34) as $N = 2n + 1$ by

$$N \leq 1 + \frac{k_\mathsf{F} W}{\pi} \tag{4.9.40}$$

and the mean free path in Eq. (4.9.38), we can estimate which disorder strengh has to be implemented such that the system should be localizing for great lengths. The condition $L > Nl$ results in the condition

$$\frac{l}{L} + \frac{W}{\pi L} k_\mathsf{F} l < 1. \tag{4.9.41}$$

In our simulation, we set the aspect ratio $W/L = 1$ and for any long enough system, the first term should become negligible. Therefore, the condition that the system localizes at large L is given for a quadratic system by

$$k_\mathsf{F} l < \pi. \tag{4.9.42}$$

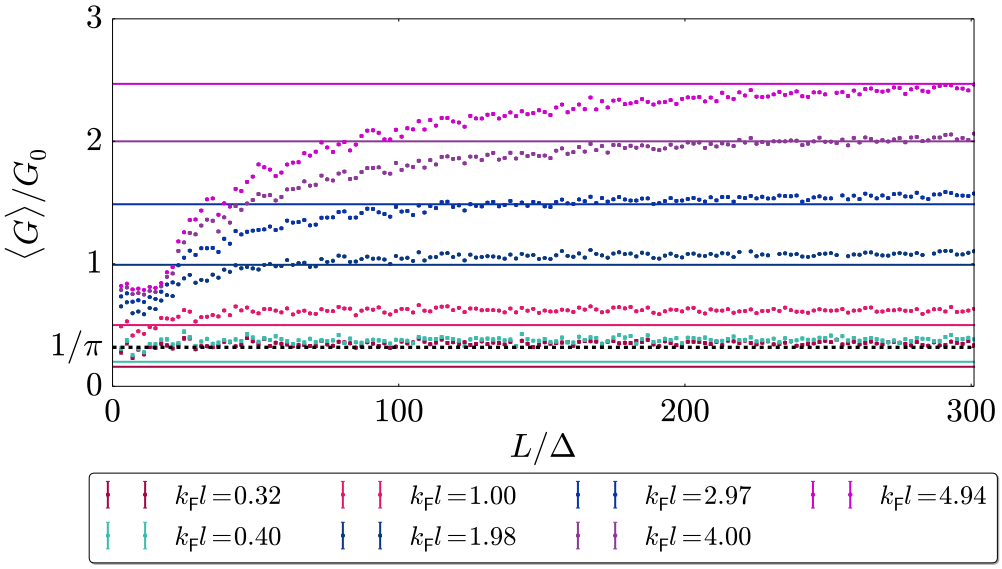

Figure 4.25.: The figure shows the simulated conductance in units of $G_0 = 4e^2/h$ for systems with different disorder strength in the vector potential at energy $E_F = 0.3\hbar v_F/\Delta$. The systems were simulated at fixed aspect ratio $W/L = 1$, and we averaged over 1000 disorder configurations. We see that with increasing system size, the conductivity approaches for systems with $k_F l \gg 1$ the diffusive value of Eq. (4.9.39). The diffusive conductivity is cutoff for small values by $\sigma_0 = 1/\pi$ [38]. .

The five lowest data sets of Fig. 4.25 fulfill this condition, where the mean free path of these systems, which were simulated at $k_F = 0.3/\Delta$ can be estimated to $l \leq 10\Delta$. Still it remains a hard task to evaluate a non-vanishing $\beta(g)$ function for the disordered system as in Sect. 3.2.2 (here $g = G/G_0$). The results of [25] suggest that the magnitude of the β function is very small for the most part. This is in agreement with the given data, and our lack of computational power to simulate larger systems might be the reason as to why we can not resolute the β function with higher accuracy.

We finish this chapter with the simulation of a quantum Hall system in the staggered fermion model, where we add additionally disorder in the vector potential. The resulting conductance values for different disorder strengths is shown in Fig. 4.26. We show the conductance over $k_F l_B$. From Eq. (4.5.6), we expect and see the n^{th} quantum Hall step at

$$k_F l_B = \sqrt{2n}. \tag{4.9.43}$$

In the case of $l \gg l_B$, the quantum Hall plateaus are not affected by the disorder. For increasing disorder, the higher modes start to break down. For l in the order of l_B, we no longer see quantum Hall steps due to the disorder. To explain whether the simulation in the staggered fermion model really reproduces the results from an experiment, further analysis

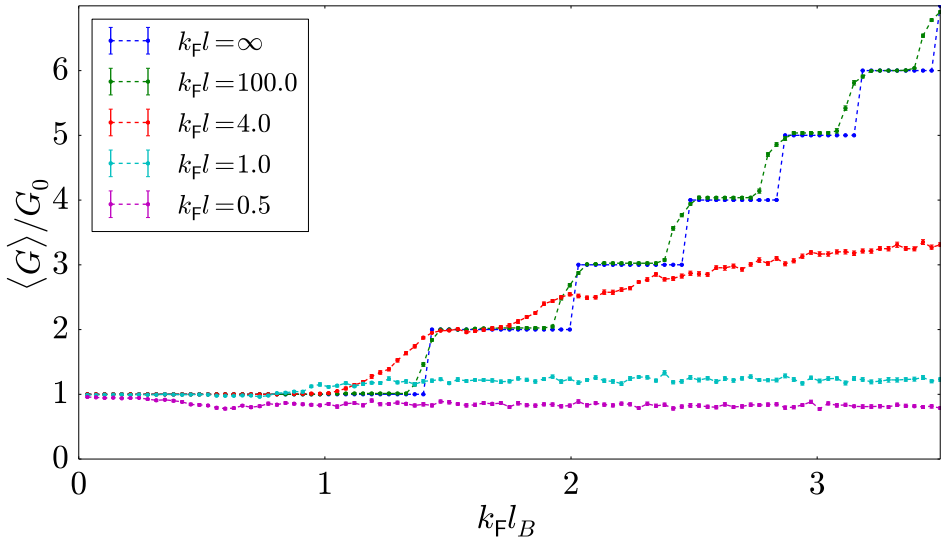

Figure 4.26.: We show the conductance steps for a quantum Hall system simulated in the staggered fermion model, with additionally implemented disorder in the vector potential, over the Fermi wavevector in units of the magnetic length. The disorder is characterized by the $k_F l$ values which are determined by Eq. (4.9.38). The width and length of the system is set to $W = L = 201\Delta$. The constant magnetic field is given by $B = 0.01\hbar/e\Delta^2$, which corresponds to a magnetic length of $l_B = 10\Delta$. The simulated values were averaged over 100 disorder configurations. We see the breakdown of the quantum Hall effect for l in the order of l_B. .

need to be performed in the characterization of the disorder. We leave this question open at this point for future studies.

5. Summary

In this thesis, we have given an introduction to the scattering formalism, which we have employed for describing transport properties of systems, characterized by a single-particle Hamiltonian. Using the scattering matrix formalism of Ch. 2, we have shown a connection of the scattering matrix to transport quantities, such as the conductance and the local density of states. We have given simple examples of the general formulas to deepen the intuitive understanding of the formalism. Furthermore, the equivalence to the Fisher-Lee relation has been shown. Thus, the connection to an alternative approach, the non-equilibrium Green's function formalism, has been given.

In Ch. 3, we have introduced a simple model, which can be used to describe many transport properties observed in two-dimensional electron gases of GaAs heterostructures. Special interest has been given to the implementation of magnetic fields and disorder. We have reconciled the implementation with the theoretical results obtained from the integer quantum Hall effect and for disordered systems. Furthermore, we have evaluated the localization scaling function $\beta(\sigma)$, and have been able to reproduce the functional form, which is given from the theory of weak localization. Some deviations in the obtained values to the theory have been observed, and traced back due to finite-size corrections.

Finally, we have used the introduced concepts in Ch. 4 to discuss topics of interest in models of graphene. For this purpose, we have presented the commonly used tight-binding model from the atomic basis of the honeycomb lattice, and we have discussed why our simulation on a coarser lattice should reproduce the same transport results for low-energy electrons. Furthermore, we have introduced a method that attaches a system to leads with many transmission channels, but introduces only a low contact resistance and avoids simulating very large leads. The different edge types have been discussed, and we have checked whether the implementation yields the estimated results in the simulated conductance for the simple setup of a quantum point contact. We have also discussed the same concepts for magnetic fields and disorder as in GaAs, and explained how we have implemented them in the tight-binding model of graphene.

The Aharonov-Bohm setup has been simulated for possible comparison with present day experiments. We have observed oscillations in the conductance, and have connected the frequency and its higher harmonics to the ring structure of the device. Furthermore, we have presented a device geometry, which can be used to observe Aharonov-Bohm oscillations in the quantum Hall regime. Due to the chiral edge states of the quantum Hall effect, we have observed sharper peaks and even higher harmonics in the simulation. In the sections following Sect. 4.7, we have focused on the effect of strain on transport properties. Starting from, how strain in the lattice should affect the transport properties by introducing a pseudo-magnetic field into the system, we have questioned which effects kinks at the edge and long-range disorder in the sample have. For the kinks, we have setup a simple model with only little

assumptions and found that the necessary angles for an observable effect on the quantum Hall plateaus are out of a realistic range. For the long-range disorder, we have introduced the staggered fermion model, and have extended it by a magnetic field. We have used the model to simulate the effect of a random strain field, and we have observed in the model the breakdown of the quantum Hall effect, once the mean free path of the disorder is in the order of the magnetic length.

As an outlook, we propose that the discussion of the effects of long-range disorder on graphene can be continued. Furthermore, as experiments with more complex structures become possible, the presented methods can help to estimate which setups should result in interesting results before the fabrication process has even started.

A. Appendix

A.1. Calculations for the Scattering Matrix

A.1.1. Normalization of the Propagating Modes

The condition for the scattering matrix to be unitary in Sect. 2.3 is that each propagating mode is normalized such that it carries unit flux. We want to obtain an explicit expression for the particle flux, which was given in Sect. 2.2 by

$$j_m = \rho_m v_m = \chi_m^\dagger \chi_m \frac{1}{\hbar} \frac{\mathrm{d}E}{\mathrm{d}k_m}, \tag{A.1.1}$$

without having to calculate the derivative. To this end, we want to employ the Hellman-Feynman theorem. For a given Hermitian operator H_α, which depends on a parameter α, with eigenvalues E_α and corresponding eigenstates ψ_α, which also may depend on the parameter α the Hellman-Feynman theorem states

$$\psi_\alpha^\dagger \psi_\alpha \frac{\mathrm{d}E_\alpha}{\mathrm{d}\alpha} = \psi_\alpha^\dagger \frac{\mathrm{d}H_\alpha}{\mathrm{d}\alpha} \psi_\alpha. \tag{A.1.2}$$

The proof of the theorem is straightforward by calculating $\partial_\alpha\big(\psi_\alpha^\dagger H_\alpha \psi_\alpha\big)$ and using $H_\alpha \psi_\alpha = E_\alpha \psi_\alpha$. In our case, the states are given by χ_m and the operator in question is given for the parameter E in Eq. (2.2.4) by

$$H_E = \lambda_m T_\mathsf{L}^\dagger + H_\mathsf{L} + \lambda_m^{-1} T_\mathsf{L}. \tag{A.1.3}$$

Then, with the Hellmann-Feynman theorem for $\alpha = E$, $\psi_\alpha = \chi_m$ and the eigenvalue equation $H_E \chi_m = E \chi_m$, we conclude

$$\chi_m^\dagger \chi_m 1 = \chi_m^\dagger \left(\frac{\mathrm{d}\lambda_m}{\mathrm{d}E} T_\mathsf{L}^\dagger + \frac{\mathrm{d}\lambda_m^{-1}}{\mathrm{d}E} T_\mathsf{L} \right) \chi_m, \tag{A.1.4}$$

$$= \frac{1}{\lambda_m} \frac{\mathrm{d}\lambda_m}{\mathrm{d}E} \chi_m^\dagger \Big(\lambda_m T_\mathsf{L}^\dagger - \lambda_m^{-1} T_\mathsf{L} \Big) \chi_m, \tag{A.1.5}$$

and thus

$$\chi_m^\dagger \chi_m \frac{\mathrm{d}E}{\mathrm{d}\log\big(\lambda_m\big)} = \chi_m^\dagger \Big(\lambda_m T_\mathsf{L}^\dagger - \lambda_m^{-1} T_\mathsf{L} \Big) \chi_m. \tag{A.1.6}$$

For a propagating mode with $\lambda_m = \exp\big(i k_m a\big)$ and $\lambda_m^{-1} = \lambda_m^*$, we finally obtain

$$j_m = \chi_m^\dagger \chi_m v_m = \frac{2a}{\hbar} \chi_m^\dagger \, \mathsf{Im}\Big(\lambda_m^* T_\mathsf{L} \Big) \chi_m, \tag{A.1.7}$$

with $dE/dk = \hbar v$.

Therefore in a practical implementation, we have essentially to calculate for all propagating modes the imaginary party of the expectation value $\langle \lambda_m^* T_\mathsf{L} \rangle$. If this results in a positive value, we denote the mode as outgoing, and if it is negative, we denote it as incoming. To normalize the propagating modes, we calculate

$$\tilde{\chi}_m = \sqrt{\frac{1}{|j_m|}} \chi_m. \tag{A.1.8}$$

Thus, the calculation of $\tilde{j}_m$ according to (A.1.7) with the renormalized propagating states yields $\tilde{j}_m = \pm 1$. We drop the tilde again, as we will consider the propagating states always under this normalization condition.

A.1.2. Simplify the System of Equations for the Scattering Matrix

Using the Schrödinger equation, we obtained the linear system of equations for the scattering matrix in Eq. (2.5.6), which read

$$\begin{pmatrix} T_\mathsf{L} U_\mathsf{o} & T_\mathsf{L} U_\mathsf{e} & -T_\mathsf{LS} \\ T_\mathsf{LS}^\dagger U_\mathsf{o} \Lambda_\mathsf{o} & T_\mathsf{LS}^\dagger U_\mathsf{e} \Lambda_\mathsf{e} & H_\mathsf{S} - E \end{pmatrix} \begin{pmatrix} S \\ \tilde{S} \\ \phi_\mathsf{S} \end{pmatrix} = \begin{pmatrix} -T_\mathsf{L} U_\mathsf{i} \\ -T_\mathsf{LS}^\dagger U_\mathsf{i} \Lambda_\mathsf{i} \end{pmatrix}. \tag{A.1.9}$$

We want to eliminate $\tilde{S}$ from these equations. It is not needed to calculate any transport properties, and only important for the mode matching procedure. We transform the system of equations by multiplying both sides from the left with the same matrix

$$A = \begin{pmatrix} \Lambda_\mathsf{o}^\dagger U_\mathsf{o}^\dagger & 0 \\ \Lambda_\mathsf{e}^\dagger U_\mathsf{e}^\dagger & 0 \\ 0 & -\mathbb{1} \end{pmatrix}. \tag{A.1.10}$$

This will yield the equation

$$\begin{pmatrix} \Lambda_\mathsf{o}^\dagger U_\mathsf{o}^\dagger T_\mathsf{L} U_\mathsf{o} & \Lambda_\mathsf{o}^\dagger U_\mathsf{o}^\dagger T_\mathsf{L} U_\mathsf{e} & -\Lambda_\mathsf{o}^\dagger U_\mathsf{o}^\dagger T_\mathsf{LS} \\ \Lambda_\mathsf{e}^\dagger U_\mathsf{e}^\dagger T_\mathsf{L} U_\mathsf{o} & \Lambda_\mathsf{e}^\dagger U_\mathsf{e}^\dagger T_\mathsf{L} U_\mathsf{e} & -\Lambda_\mathsf{e}^\dagger U_\mathsf{e}^\dagger T_\mathsf{LS} \\ -T_\mathsf{LS}^\dagger U_\mathsf{o} \Lambda_\mathsf{o} & -T_\mathsf{LS}^\dagger U_\mathsf{e} \Lambda_\mathsf{e} & E - H_\mathsf{S} \end{pmatrix} \begin{pmatrix} S \\ \tilde{S} \\ \phi_\mathsf{S} \end{pmatrix} = \begin{pmatrix} -\Lambda_\mathsf{o}^\dagger U_\mathsf{o}^\dagger T_\mathsf{L} U_\mathsf{i} \\ -\Lambda_\mathsf{e}^\dagger U_\mathsf{e}^\dagger T_\mathsf{L} U_\mathsf{i} \\ T_\mathsf{LS}^\dagger U_\mathsf{i} \Lambda_\mathsf{i} \end{pmatrix}. \tag{A.1.11}$$

We require for a equivalence that the matrix A and thus $U_< \Lambda_< \equiv (U_\mathsf{o} \Lambda_\mathsf{o}, U_\mathsf{e} \Lambda_\mathsf{e})$ is invertible. Even more precise, as $\Lambda_<$ is always invertible, $U_< \equiv (U_\mathsf{o}, U_\mathsf{e})$ needs to be invertible. This requirement is discussed in more detail in Appendix A.1.7.

For a shorter notation, we define for $a, b \in \{\mathsf{i}, \mathsf{o}, \mathsf{e}\}$

$$\begin{aligned} T_{ab} &\equiv \Lambda_a^\dagger U_a^\dagger T_\mathsf{L} U_b, \\ T_{a\mathsf{s}} &\equiv \Lambda_a^\dagger U_a^\dagger T_\mathsf{LS}, \\ T_{\mathsf{s}a} &\equiv T_{a\mathsf{s}}^\dagger. \end{aligned} \tag{A.1.12}$$

The matrices T_{ab} are effectively given by the matrix elements of T_{L} between the states χ_b and $\lambda_a\chi_a$, and thus represent the hopping of the modes from one site of the lead into the various modes of the next site of the lead. By these definitions, we rewrite Eq. (A.1.11) to

$$\begin{pmatrix} T_{\mathsf{oo}} & T_{\mathsf{oe}} & -T_{\mathsf{os}} \\ T_{\mathsf{eo}} & T_{\mathsf{ee}} & -T_{\mathsf{es}} \\ -T_{\mathsf{so}} & -T_{\mathsf{se}} & E - H_{\mathsf{S}} \end{pmatrix} \begin{pmatrix} S \\ \tilde{S} \\ \phi_{\mathsf{S}} \end{pmatrix} = \begin{pmatrix} -T_{\mathsf{oi}} \\ -T_{\mathsf{ei}} \\ T_{\mathsf{si}} \end{pmatrix}. \tag{A.1.13}$$

In A.1.3, we proof that T_{ee} is Hermitian. We assume T_{ee} to be invertible, as should be the generic case, and thus can eliminate $\tilde{S}$ from the equations by

$$\tilde{S} = -\frac{1}{T_{\mathsf{ee}}} T_{ei} - \frac{1}{T_{\mathsf{ee}}} T_{\mathsf{eo}} S + \frac{1}{T_{\mathsf{ee}}} T_{\mathsf{es}} \phi_{\mathsf{S}}. \tag{A.1.14}$$

Then, the system of equations reads

$$\begin{pmatrix} T_{\mathsf{oo}} - T_{\mathsf{oe}} \frac{1}{T_{\mathsf{ee}}} T_{\mathsf{eo}} & -T_{\mathsf{os}} + T_{\mathsf{oe}} \frac{1}{T_{\mathsf{ee}}} T_{\mathsf{es}} \\ -T_{\mathsf{so}} + T_{\mathsf{se}} \frac{1}{T_{\mathsf{ee}}} T_{\mathsf{eo}} & E - H_{\mathsf{S}} - T_{\mathsf{se}} \frac{1}{T_{\mathsf{ee}}} T_{\mathsf{es}} \end{pmatrix} \begin{pmatrix} S \\ \phi_{\mathsf{S}} \end{pmatrix} = \begin{pmatrix} -T_{\mathsf{oi}} + T_{\mathsf{oe}} \frac{1}{T_{\mathsf{ee}}} T_{\mathsf{ei}} \\ T_{\mathsf{si}} - T_{\mathsf{se}} \frac{1}{T_{\mathsf{ee}}} T_{\mathsf{ei}} \end{pmatrix}. \tag{A.1.15}$$

We will shorten the notation even further by introducing for $a, b \in \{\mathsf{i}, \mathsf{o}, \mathsf{s}\}$ the matrices

$$K_{ab} \equiv T_{ab} - T_{a\mathsf{e}} \frac{1}{T_{\mathsf{ee}}} T_{\mathsf{e}b}. \tag{A.1.16}$$

The matrices describe the hopping of the propagating mode from one lead site into the various propagating modes of the next lead site, where it is included that the mode can turn into an evanescent mode in an intermediate step and return afterwards. With these matrices Eq. (A.1.15) reads in a compact way

$$\begin{pmatrix} K_{\mathsf{oo}} & -K_{\mathsf{os}} \\ -K_{\mathsf{so}} & E - H - T_{\mathsf{se}} \frac{1}{T_{\mathsf{ee}}} T_{\mathsf{es}} \end{pmatrix} \begin{pmatrix} S \\ \phi_{\mathsf{S}} \end{pmatrix} = \begin{pmatrix} -K_{\mathsf{oi}} \\ K_{\mathsf{si}} \end{pmatrix}, \tag{A.1.17}$$

with which we continue in Sect. 2.5.

A.1.3. Generalized Orthogonality

In [9], generalized orthogonality relations are derived for the lead modes. We can use these to derive properties of the T, and thus the K matrices, which are defined in A.1.2. Furthermore, we will introduce analogue to [9] another useful matrix that we denote by Γ, and which will be useful in the basis transformation of incoming and outgoing states.

By taking Eq. (2.2.4) and subtracting the Hermitian conjugate of the equation, we obtain the relation

$$\chi_n^\dagger \left(\lambda_n^* T_{\mathsf{L}} - \lambda_m T_{\mathsf{L}}^\dagger \right) \chi_m \left(1 - \lambda_m \lambda_n^* \right) = 0. \tag{A.1.18}$$

For a set of different modes, this equation can also be written in terms of the matrix equation

$$\left(\Lambda_n^\dagger U_n^\dagger T_{\mathsf{L}} U_m - U_n^\dagger T_{\mathsf{L}}^\dagger U_m \Lambda_m \right) \left(\mathbb{1} - \Lambda_m \Lambda_n^\dagger \right) = 0. \tag{A.1.19}$$

In the case where one matrix group is set by the evanescent modes, the first term has to be zero, because the evanescent eigenvalues are restricted by $|\lambda| < 1$.

Therefore, we can write for $a, b \in \{\mathsf{i}, \mathsf{o}, \mathsf{e}\}$, but without pairs $(a, b) = (\mathsf{i},\mathsf{i})$ or $(a, b) = (\mathsf{o},\mathsf{o})$

$$\Lambda_a^\dagger U_a^\dagger T_\mathsf{L} U_b - U_a^\dagger T_\mathsf{L}^\dagger U_b \Lambda_b = 0. \tag{A.1.20}$$

Expressed with the T matrices from Eq. (A.1.12), we get the relation

$$T_{ab} = T_{ba}^\dagger. \tag{A.1.21}$$

This already proves that T_{ee} is Hermitian. From the property of Eq. (A.1.21), we directly see from the definition in Eq. (A.1.16) that

$$K_{ab} = K_{ba}^\dagger. \tag{A.1.22}$$

For the special case of T_{oo} and T_{ii}, the matrix equation of Eq. (A.1.20) can be evaluated with the Hellman-Feynman Theorem like done in Appendix A.1.1. As we normalized the transverse modes with respect to their velocity, we yield (having $v = 1$ for outgoing modes, and $v = -1$ for incoming modes)

$$T_{\mathsf{oo}} - T_{\mathsf{oo}}^\dagger = i\mathbb{1}, \tag{A.1.23}$$

$$T_{\mathsf{ii}} - T_{\mathsf{ii}}^\dagger = -i\mathbb{1}, \tag{A.1.24}$$

and thus follow

$$K_{\mathsf{oo}} - K_{\mathsf{oo}}^\dagger = i\mathbb{1}, \tag{A.1.25}$$

$$K_{\mathsf{ii}} - K_{\mathsf{ii}}^\dagger = -i\mathbb{1}. \tag{A.1.26}$$

We can summarize nearly all of the generalized orthogonality relations by introducing the matrix $U_<$ and adequately $\Lambda_<$:

$$U_< \equiv (U_\mathsf{o}, U_\mathsf{e}), \tag{A.1.27}$$

$$\Lambda_< \equiv \begin{pmatrix} \Lambda_\mathsf{o} & \\ & \Lambda_\mathsf{e} \end{pmatrix}. \tag{A.1.28}$$

For these matrices, the generalized orthogonality relations result in

$$-i\left(\Lambda_<^\dagger U_<^\dagger T_\mathsf{L} U_< - U_<^\dagger T_\mathsf{L}^\dagger U_< \Lambda_<\right) = \left(\begin{array}{c|c} \mathbb{1} & 0 \\ \hline 0 & 0 \end{array}\right) \equiv 1_p, \tag{A.1.29}$$

where 1_p is a $d_\mathsf{L} \times d_\mathsf{L}$ block matrix with a $N_p \times N_p$ identity matrix in the upper left block. Now, we multiply this equation by $U_<^{-1\,\dagger}$ from the left and by $U_<^{-1}$ from the right, where we discuss the existence of $U_<^{-1}$ in A.1.7. For practical reasons, we define the left hand side as

$$\Gamma \equiv i\Big(T_\mathsf{L}^\dagger U_< \Lambda_< U_<^{-1} - U_<^{-1\,\dagger} \Lambda_<^\dagger U_<^\dagger T_\mathsf{L}\Big), \tag{A.1.30}$$

and obtain

$$\Gamma = U_<^{-1\,\dagger} 1_p U_<^{-1}. \tag{A.1.31}$$

The matrix Γ is obviously Hermitian. In [9], it is shown that the retarded Green's function g of the lead is given by the equation

$$gT_L = U_< \Lambda_< U_<^{-1}. \tag{A.1.32}$$

Therefore, we can also write the matrix Γ in terms of the leads Green's function via

$$\Gamma = iT_{\mathsf{L}}^{\dagger}\Big(g - g^{\dagger}\Big)T_{\mathsf{L}}. \tag{A.1.33}$$

If we denote the inverse matrix $U_<^{-1}$ as

$$U_<^{-1} \equiv \begin{pmatrix} \Upsilon_{\mathsf{o}}^{\dagger} \\ \Upsilon_{\mathsf{e}}^{\dagger} \end{pmatrix}, \tag{A.1.34}$$

we can define a general $d_{\mathsf{L}} \times d_{\mathsf{L}}$ identity from $U_< U_<^{-1}$ as

$$U_{\mathsf{o}}\Upsilon_{\mathsf{o}}^{\dagger} + U_{\mathsf{e}}\Upsilon_{\mathsf{e}}^{\dagger} = \mathbb{1}. \tag{A.1.35}$$

By looking at $\Gamma U_<$, we get the relations

$$\Gamma U_{\mathsf{o}} = \Upsilon_{\mathsf{o}}, \tag{A.1.36}$$
$$\Gamma U_{\mathsf{e}} = 0. \tag{A.1.37}$$

Therefore, we can write the relations from $U_<^{-1}U_<$ as

$$\mathbb{1} = U_{\mathsf{o}}^{\dagger}\Gamma U_{\mathsf{o}}, \tag{A.1.38}$$
$$0 = U_{\mathsf{o}}^{\dagger}\Gamma U_{\mathsf{e}}, \tag{A.1.39}$$
$$\mathbb{1} = \Upsilon_{\mathsf{e}}^{\dagger} U_{\mathsf{e}}, \tag{A.1.40}$$
$$0 = \Upsilon_{\mathsf{e}}^{\dagger} U_{\mathsf{o}}. \tag{A.1.41}$$

Using (A.1.31) and the above identities, we can also write for Γ

$$\Gamma = \Gamma U_{\mathsf{o}} U_{\mathsf{o}}^{\dagger}\Gamma. \tag{A.1.42}$$

A.1.4. Basis Transform

The expressions of Appendix A.1.3 can be used to set up equations to transform between the basis of the incoming and outgoing modes. For this reason, we use the Γ matrix to define the unitary transformation matrices

$$C_{\mathsf{io}} \equiv U_{\mathsf{i}}^{\dagger}\Gamma U_{\mathsf{o}}, \tag{A.1.43}$$
$$C_{\mathsf{oi}} \equiv C_{\mathsf{io}}^{\dagger} = U_{\mathsf{o}}^{\dagger}\Gamma U_{\mathsf{i}}. \tag{A.1.44}$$

Using Eq. (A.1.35), we get the relations

$$U_{\mathsf{i}} = U_{\mathsf{o}} C_{\mathsf{oi}} + U_{\mathsf{e}} \Upsilon_{\mathsf{e}}^{\dagger} U_{\mathsf{i}}, \tag{A.1.45}$$

$$U_{\mathsf{i}} \Lambda_{\mathsf{i}} = U_{\mathsf{o}} \Lambda_{\mathsf{o}} \Lambda_{\mathsf{o}}^{\dagger} C_{\mathsf{oi}} \Lambda_{\mathsf{i}} + U_{\mathsf{e}} \Lambda_{\mathsf{e}} \Lambda_{\mathsf{e}}^{-1} \Upsilon_{\mathsf{e}}^{\dagger} U_{\mathsf{i}} \Lambda_{\mathsf{i}}. \tag{A.1.46}$$

Then, it follows by inserting the first relation into the definition of $T_{a\mathsf{i}}$ for $a \in \{\mathsf{o}, \mathsf{e}\}$ (given in Eq. (A.1.12)) that

$$T_{a\mathsf{i}} = T_{a\mathsf{o}} C_{\mathsf{oi}} + T_{a\mathsf{e}} \Upsilon_{\mathsf{e}}^{\dagger} U_{\mathsf{i}}. \tag{A.1.47}$$

Now, if we evaluate K_{oi} (which is defined in Eq. (A.1.16)) that the additional term generated by the evanescent modes in T_{oi} and T_{ei} neatly cancels, and thus we have

$$K_{\mathsf{oi}} = K_{\mathsf{oo}} C_{\mathsf{oi}}. \tag{A.1.48}$$

In analogue calculations, we obtain the transformation equations listed in Glossary (G.27)–(G.30). We can therefore use C_{oi} to switch the index of the K matrix and thus understand it as a matrix, which transforms between the basis sets of the incoming and outgoing modes. The Eq. (A.1.48) gives also an equation for calculating C_{oi}, which avoids the calculation of the Γ matrix explicitly.

Furthermore, we can proof the unitarity of the transformation matrices

$$C_{\mathsf{io}} C_{\mathsf{oi}} = \mathbb{1}. \tag{A.1.49}$$

Using Eq. (A.1.42), we only need to show

$$U_{\mathsf{i}}^{\dagger} \Gamma U_{\mathsf{i}} = \mathbb{1}. \tag{A.1.50}$$

We use the generalized orthogonality of the incoming modes on the outgoing and evanescent modes

$$U_{\mathsf{i}}^{\dagger} T_{\mathsf{L}}^{\dagger} U_{<} \Lambda_{<} = \Lambda_{\mathsf{i}}^{\dagger} U_{\mathsf{i}}^{\dagger} T_{\mathsf{L}} U_{<}, \tag{A.1.51}$$

and the Hermitian conjugate of the equation

$$\Lambda_{<}^{\dagger} U_{<}^{\dagger} T_{\mathsf{L}} U_{\mathsf{i}} = U_{<}^{\dagger} T_{\mathsf{L}}^{\dagger} U_{\mathsf{i}} \Lambda_{\mathsf{i}}. \tag{A.1.52}$$

Thus, $U_{\mathsf{i}}^{\dagger} \Gamma U_{\mathsf{i}}$ is given by inserting the definition of Γ from Eq. (A.1.30) as

$$U_{\mathsf{i}}^{\dagger} \Gamma U_{\mathsf{i}} = i \Big(\Lambda_{\mathsf{i}}^{\dagger} U_{\mathsf{i}}^{\dagger} T_{\mathsf{L}} U_{\mathsf{i}} - U_{\mathsf{i}}^{\dagger} T_{\mathsf{L}}^{\dagger} U_{\mathsf{i}} \Lambda_{\mathsf{i}} \Big). \tag{A.1.53}$$

From the normalization condition of the incoming modes

$$\Lambda_{\mathsf{i}}^{\dagger} U_{\mathsf{i}}^{\dagger} T_{\mathsf{L}} U_{\mathsf{i}} - U_{\mathsf{i}}^{\dagger} T_{\mathsf{L}}^{\dagger} U_{\mathsf{i}} \Lambda_{\mathsf{i}} = T_{\mathsf{ii}} - T_{\mathsf{ii}}^{\dagger} = -i\mathbb{1}, \tag{A.1.54}$$

we see that Eq. (A.1.53) just equals to one and therefore proof Eq. (A.1.50). Consequently, the unitarity of C_{io} is shown.

A.1.5. Unitarity of the Scattering Matrix

We can explicitly show that the expression for S is always unitary in our chosen normalization of the modes, using the results from Sect. A.1.4. We start from the scattering matrix given in Eq. (2.5.12). We can either transform it into the following form by terms of linear algebra, or make use of the fact that this formula was obtained from the blockwise inversion formula Eq. (2.5.11). Equivalently, we could have used another blockwise inversion formula

$$\begin{pmatrix} A & B \\ C & D \end{pmatrix}^{-1} = \begin{pmatrix} (A-BD^{-1}C)^{-1} & -(A-BD^{-1}C)^{-1}BD^{-1} \\ -D^{-1}C(A-BD^{-1}C)^{-1} & D^{-1}+D^{-1}C(A-BD^{-1}C)^{-1}BD^{-1} \end{pmatrix} \tag{A.1.55}$$

to obtain directly

$$S_{\mathsf{io}} = -\left(K_{\mathsf{oo}} - K_{\mathsf{os}}\frac{1}{E-H_{\mathsf{eff}}}K_{\mathsf{so}}\right)^{-1}\left(K_{\mathsf{oi}} - K_{\mathsf{os}}\frac{1}{E-H_{\mathsf{eff}}}K_{\mathsf{si}}\right). \tag{A.1.56}$$

This is equivalent to (using Eq. (G.28) and Eq. (G.31))

$$S_{\mathsf{io}} = -\left(K_{\mathsf{oo}} - K_{\mathsf{os}}\frac{1}{E-H_{\mathsf{eff}}}K_{\mathsf{so}}\right)^{-1}\left(K_{\mathsf{oo}}^{\dagger} - K_{\mathsf{os}}\frac{1}{E-H_{\mathsf{eff}}}K_{\mathsf{so}}\right)\Lambda_{\mathsf{o}}^{\dagger}C_{\mathsf{oi}}\Lambda_{\mathsf{i}}. \tag{A.1.57}$$

For $S_{\mathsf{io}}^{\dagger}$, we read

$$S_{\mathsf{io}}^{\dagger} = -\Lambda_{\mathsf{i}}^{\dagger}C_{\mathsf{io}}\Lambda_{\mathsf{o}}\left(K_{\mathsf{oo}} - K_{\mathsf{os}}\frac{1}{E-H_{\mathsf{eff}}}K_{\mathsf{so}}\right)\left(K_{\mathsf{oo}}^{\dagger} - K_{\mathsf{os}}\frac{1}{E-H_{\mathsf{eff}}}K_{\mathsf{so}}\right)^{-1}. \tag{A.1.58}$$

The terms in the parentheses commute, and as we already showed that $C_{\mathsf{io}}^{-1} = C_{\mathsf{oi}}$ in Sect. A.1.4, we directly see the unitarity of the scattering matrix

$$SS^{\dagger} = S^{\dagger}S = \mathbb{1}. \tag{A.1.59}$$

A.1.6. Invertibility of K_{oo} and K_{ii}

From the properties $K_{\mathsf{oo}} - K_{\mathsf{oo}}^{\dagger} = i\mathbb{1}$ and $K_{\mathsf{ii}} - K_{\mathsf{ii}}^{\dagger} = -i\mathbb{1}$, which were given in Appendix A.1.3, we can show that both matrices are always invertible. For K_{oo} we show it by defining the matrix

$$\tilde{K}_{\mathsf{oo}} = K_{\mathsf{oo}} - \frac{i}{2}\mathbb{1}. \tag{A.1.60}$$

The defined matrix $\tilde{K}_{\mathsf{oo}}$ is Hermitian and thus its spectrum is real. Therefore, we see by Eq. (A.1.60) that the spectrum of K_{oo} has always a non vanishing imaginary part of $\frac{1}{2}$. As the imaginary part never vanishes, we always have $\det(K_{\mathsf{oo}}) \neq 0$, which consequently means that K_{oo}^{-1} always exists. The same arguments can be given for the existence of the inverse of K_{ii}.

A.1.7. Invertibility of $U_<$

In the presented derivation of the Weidenmüller formula, we needed the matrix built up by the eigenvectors of the outgoing and evanescent modes to be invertible. In [9] it is assumed without proof. We are also not able to give a general proof for this to be always true, as there are non-generic cases when the matrix is no longer invertible.

We want to construct such a non-generic case to get a better understanding of the problem. The matrix $U_<$ is build up by the outgoing and evanescent eigenvectors, which are a solution to the quadratic eigenvalue problem of Eq. (2.2.5)

$$\Big[T_\mathsf{L}^\dagger \lambda_m^2 + \big(H_\mathsf{L} - E\mathbb{1}\big)\lambda_m + T_\mathsf{L}\Big]\chi_m = 0. \tag{A.1.61}$$

The evanescent modes are the modes, which correspond to eigenvalues $\big|\lambda_m\big| < 1$, and outgoing modes are characterized by checking for $\big|\lambda_m\big| = 1$ whether the velocity $v = \mathrm{Im}\langle \lambda_m T_\mathsf{L}^\dagger\rangle > 0$. In the case where one eigenvector χ_m of the set of outgoing and evanescent modes is linearly dependent of a subset M of the other eigenvectors, meaning

$$\chi_m = \sum_{n\in M} c_n \chi_n \tag{A.1.62}$$

the matrix $U_<$ is no longer invertible. Let us construct such a case for a system with two modes where two different eigenvalues $\lambda_1 \neq \lambda_2$ are associated with the same eigenvector χ up to some normalization factor, which we drop for the further discussion. Then, the matrix will certainly be no longer invertible. From this case follows the condition (by taking the difference of both equations)

$$\Big[T_\mathsf{L}^\dagger\big(\lambda_1 + \lambda_2\big) + \big(H_\mathsf{L} - E\mathbb{1}\big)\Big]\chi = 0. \tag{A.1.63}$$

This is a quite special case which desires fine-tuning and is not an obstacle in any generic calculation. But still the possibility to find such solutions is a reason, as to why we fail to give a proof that $U_<$ is invertible in any case.

A.1.8. Simple Leads

To discuss the electronic transport properties of a system, we need to attach it via leads to a reservoir. To get an intuitive feeling for the formulas that are used, we want to consider leads which have a very simple structure. We fix them at $E = 0$, and set the onsite terms $H_\mathsf{L} = 0$. The lead hoppings are set to $T_\mathsf{L} = -t\mathbb{1}$, where $t \in \mathbb{R}^+$. These leads have a very simple structure and the quadratic eigenvalue problem of Eq. (2.2.5) for the effective lead reads

$$(\lambda_m^2 + 1)\chi_m = 0. \tag{A.1.64}$$

It is solved by $\lambda_m = \pm i$. Therefore, every mode of the lead is propagating and there are no evanescent modes. In the next step, we can calculate the velocity (as described in A.1.1) and normalize the transverse modes χ_m with respect to it. We note that $\lambda_m = i$ corresponds to a positive velocity and is thus outgoing, whereas $\lambda_m = -i$ denotes the incoming mode.

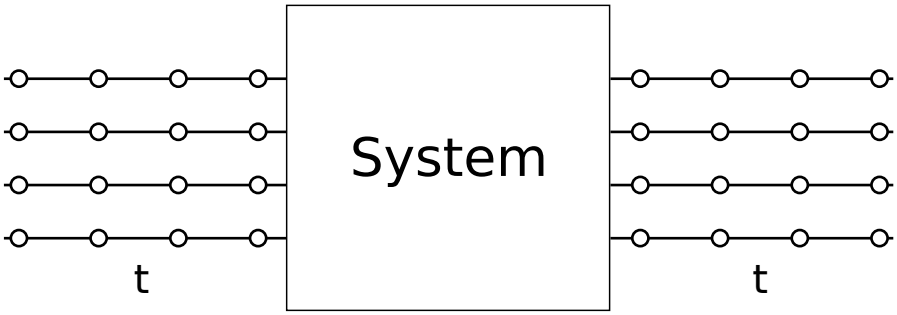

Figure A.1.: Structure of simple leads are just independent linear chains.

After the normalization, the matrix spanned by the transverse eigenstates is just the identity matrix times a constant and is naturally the same for the incoming and outgoing modes

$$U_{\mathsf{o}} = U_{\mathsf{i}} = \sqrt{\frac{1}{2t}}\mathbb{1}. \tag{A.1.65}$$

As there are no evanescent modes, we have the identity $K_{ab} = T_{ab}$ for the K and the T matrices. Therefore, we can evaluate the matrices easily and obtain

$$K_{\mathsf{ii}} = -\frac{i}{2}\mathbb{1}, \tag{A.1.66}$$

$$K_{\mathsf{is}} = \frac{i}{2}T_{\mathsf{LS}}. \tag{A.1.67}$$

As additionally K_{ii} is purely imaginary, we obtain from the definition of the energy shift Δ given in Eq. (2.6.11) that for the simple lead case we have

$$\Delta = 0. \tag{A.1.68}$$

For the effective coupling of the system to the leads, we obtain

$$W = -\frac{1}{\sqrt{2\pi}}\sqrt{\frac{2}{t}}T_{\mathsf{LS}}. \tag{A.1.69}$$

Therefore, the Weidenmüller formula for a simple lead is given by

$$S = -\mathbb{1} + i2\frac{1}{t}T_{\mathsf{LS}}\frac{1}{E - H_{\mathsf{S}} + i\frac{1}{t}T_{\mathsf{LS}}^{\dagger}T_{\mathsf{LS}}}T_{\mathsf{LS}}^{\dagger}. \tag{A.1.70}$$

We do not need to differentiate between S_{io}, S_{ii}, S_{oo}, as incoming and outgoing states are given within the same basis and thus $C_{\mathsf{io}} = \mathbb{1}$.

We can interpret the simple lead as in the following. The unit cell Hamiltonian and hopping describe independent linear chains that are connected to the scattering system as depicted in Fig. A.1. The dispersion relation, which follows from Eq. (2.2.4) fits into this picture, as it is

just the dispersion of a tight binding chain

$$E = -2t\cos(k). \tag{A.1.71}$$

We can also understand now, why a factor of π is included in the definition of the Weidenmüller formula. Like described in Sect. 2.9, we can calculate the local density of states directly from the Green's function of a system

$$d(E) = -\frac{1}{\pi}\,\mathrm{tr}\Big(\mathrm{Im}\,G^R\Big). \tag{A.1.72}$$

As we got the eigenmodes and the eigenvalues of the lead, we can use Eq. (A.1.32) to calculate the surface Green's function of the simple semi-infinite lead. This yields $g^R = -i/t$ and therefore, we obtain for a single chain

$$d(E) = \frac{1}{\pi t}. \tag{A.1.73}$$

Thus, if we have normalized the density of states to $d(E) = 1$, the Weidenmüller formula reads like the formula from nuclear physics given in Eq. (2.6.14) with a global phase factor of -1

$$S = -\mathbb{1} + 2\pi i T_{\mathsf{LS}} \frac{1}{E - H_{\mathsf{S}} + i\pi T_{\mathsf{LS}}^\dagger T_{\mathsf{LS}}} T_{\mathsf{LS}}^\dagger. \tag{A.1.74}$$

A.1.9. Transfer and Scattering Matrices

We described the structure of the scattering matrix for a two-terminal system in Sect. 2.4. In this section, we list the formulas that follow for this structure from the unitarity of the scattering matrix and how to connect the scattering matrices of two systems that are connected via an intermediate lead. The formulas also apply for systems with more than two-terminals. The leads, which are not participating in the connection, have to be summarized as an effective lead in this case. Following from the four block structure in Eq. (2.4.6) and the unitarity given in Eq. (2.3.3), we get the relations

$$rr^\dagger + t't'^\dagger = \mathbb{1}, \tag{A.1.75}$$
$$r'r'^\dagger + tt^\dagger = \mathbb{1}, \tag{A.1.76}$$
$$r^\dagger r + t^\dagger t = \mathbb{1}, \tag{A.1.77}$$
$$r'^\dagger r' + t'^\dagger t' = \mathbb{1}, \tag{A.1.78}$$
$$rt^\dagger + t'r'^\dagger = 0, \tag{A.1.79}$$
$$r^\dagger t' + t^\dagger r' = 0. \tag{A.1.80}$$

In Sect. 2.4, we introduced the transfer matrix M. To calculate the transfer matrix from the scattering matrix, we simply have to take the equations from Eq. (2.4.5) and Eq. (2.4.2),

which read explicitly

$$c^{\mathsf{oL}} = rc^{\mathsf{iL}} + t'c^{\mathsf{iR}}, \tag{A.1.81}$$
$$c^{\mathsf{oR}} = tc^{\mathsf{iL}} + r'c^{\mathsf{iR}}, \tag{A.1.82}$$
$$c^{\mathsf{oR}} = m_{11}c^{\mathsf{iL}} + m_{12}c^{\mathsf{oL}}, \tag{A.1.83}$$
$$c^{\mathsf{iR}} = m_{21}c^{\mathsf{iL}} + m_{22}c^{\mathsf{oL}}. \tag{A.1.84}$$

Thus, by solving this system of equations appropriately, we get

$$m_{11} = t^{\dagger-1}, \tag{A.1.85}$$
$$m_{12} = r't'^{-1}, \tag{A.1.86}$$
$$m_{21} = -t'^{-1}r, \tag{A.1.87}$$
$$m_{22} = t'^{-1}, \tag{A.1.88}$$

$$r = -m_{22}^{-1}m_{21}, \tag{A.1.89}$$
$$t = m_{11}^{\dagger-1}, \tag{A.1.90}$$
$$t' = m_{22}^{-1}, \tag{A.1.91}$$
$$r' = m_{12}m_{22}^{-1}. \tag{A.1.92}$$

For m_{11}, we used that we can follow from Eq. (A.1.75)–(A.1.80) the equivalence of $t - r't'^{-1}r = t^{\dagger-1}$.

An advantage of the transfer matrix is that it is often quite easy to calculate it from the Hamiltonian of a system. Furthermore, the composition of transfer matrices is quite simple. If we have two systems, we can calculate the transfer matrix of the combined system by just multiplying both transfer matrices

$$M = M_2M_1. \tag{A.1.93}$$

But a problem is that transfer matrices are not unitary like scattering matrices. The eigenvalues tend to become exponentially large and exponentially small. When we start to perform a numerical matrix multiplication, this is a bad condition. Due to numerical inaccuracies information gets lost and the calculations become unstable.

We can deduce the rules for calculating the composition of two scattering matrices $S = S_1 \circ S_2$ from the transfer matrix composition. The composition of scattering matrices is numerically robust due to the unitarity property. To obtain the rules, we first connect two transfer matrices by simple matrix multiplication, as stated in Eq. (A.1.93). Second, we transform the resulting transfer matrix to a scattering matrix built up by the components of the two sub-transfer matrices via Eq. (A.1.89)–(A.1.92). And at last, we give the resulting scattering matrix in terms of the scattering matrix components of the two subsystems by using Eq. (A.1.85)–(A.1.88). This straight forward calculation yields, by also using the unitarity

relations of Eq. (A.1.75)–(A.1.80), the following composition rules for scattering matrices

$$r = r_1 + t_1' r_2 \left(1 - r_1' r_2\right)^{-1} t_1, \tag{A.1.94}$$

$$t = t_2 \left(1 - r_1' r_2\right)^{-1} t_1, \tag{A.1.95}$$

$$t' = t_1' \left(1 - r_2 r_1'\right)^{-1} t_2', \tag{A.1.96}$$

$$r' = r_2' + t_2 r_1' \left(1 - r_2 r_1'\right)^{-1} t_2'. \tag{A.1.97}$$

The rules are intuitive if one uses the geometric series for $(1-x)^{-1}$ and thinks of the result in terms of Feynman paths. Then, the equations state that we have to consider every possible path in between to get the reflection and transmission amplitudes.

A.2. Discretization of the Continuous Schrödinger equation

For numerical purposes, we often consider only discrete points in real space instead of the continuum. This way a single particle Hamiltonian system can be solved within a numerical simulation of a tight binding model. This section shall motivate the discretization procedure for the continuous Schrödinger equation in one dimension

$$-\frac{\hbar^2}{2m}\frac{\mathrm{d}^2}{\mathrm{d}x^2}\psi(x) + V(x)\psi(x) = E\psi(x), \tag{A.2.1}$$

where $V(x)$ describes the potential of the scattering region or the leads. We can discretize the problem by only allowing discrete space values $x = na$ with the lattice spacing a. $\psi(x)$ then becomes a vector ψ, where the components ψ_n give the wavefunction at the n-th lattice position. The differential operator can be discretized in various ways. We choose to evaluate it in a symmetric manner around the point x by

$$\frac{\mathrm{d}\psi_n}{\mathrm{d}x} = \frac{1}{a}\Big(\psi_{n+\frac{1}{2}} - \psi_{n+\frac{1}{2}}\Big). \tag{A.2.2}$$

Subsequently, the discretized Schrödinger equation at a point n reads

$$-\frac{\hbar^2}{2ma^2}\Big(\psi_{n+1} + \psi_{n-1} - 2\psi_n\Big) + V_n\psi_n = E\psi_n. \tag{A.2.3}$$

For brevity, we define

$$\begin{aligned} t &\equiv \frac{\hbar^2}{2ma^2}, \\ \epsilon_n &\equiv 2t + V_n, \end{aligned} \tag{A.2.4}$$

where t is called the hopping parameter and ϵ_n denotes the onsite terms. The constant shift of $2t$ in ϵ_n is connected to the number of nearest neighbors in this one dimensional model.

With this notation the Schrödinger equation shortens, and is given by a nearest neighbor tight binding system of equations for ψ. We can write it as a matrix equation

$$\begin{pmatrix} \ddots & -t & & & \\ -t & \epsilon_{n-1} & -t & & \\ & -t & \epsilon_n & -t & \\ & & -t & \epsilon_{n+1} & -t \\ & & & & \ddots \end{pmatrix} \begin{pmatrix} \vdots \\ \psi_{n-1} \\ \psi_n \\ \psi_{n+1} \\ \vdots \end{pmatrix} = E \begin{pmatrix} \vdots \\ \psi_{n-1} \\ \psi_n \\ \psi_{n+1} \\ \vdots \end{pmatrix}, \tag{A.2.5}$$

which can be evaluated numerically for arbitrary potential functions. In braket notation, the Hamiltonian reads

$$\mathcal{H} = \sum_{n=-\infty}^{\infty} \Big(-t \left|n\right\rangle \left\langle n+1\right| - t \left|n+1\right\rangle \left\langle n\right| + \epsilon_n \left|n\right\rangle \left\langle n\right| \Big). \tag{A.2.6}$$

This discretization procedure of the continuous Schrödinger equation can naturally be generalized for higher dimensions. In two dimensions, it leads to a nearest neighbor tight binding model on a square lattice. Therefore, the onsite term for a lattice site with four neighboring sites are given by $\epsilon_n = 4t + V_n$.

We further note that the dispersion relation of a free particle can be expressed in terms of the lattice parameters of Eq. (A.2.4) via

$$E = \frac{\hbar^2 k^2}{2m} = t a^2 k^2. \tag{A.2.7}$$

In Ch. 2, we start from the most general form of a tight binding model, which includes this discretization scheme. For more details on the 2-dimensional tight binding model on the square lattice see Ch. 3.

A.3. Incorporating Magnetic Fields: Peierls substitution

To introduce a magnetic field to a system on a lattice, we can make use of the $\mathrm{U}(1)$ gauge invariance of quantum mechanics. Some arbitrary phase factor can be assigned to the wavefunction of the system at every lattice site

$$\psi(x) \to e^{i\varphi(x)} \psi(x). \tag{A.3.1}$$

This should not change anything physical if the operators acting on the system are transformed accordingly. Let us consider the example of a model on a square lattice, which we use for the simulation of GaAs in Ch. 3. If we implement this transformation into the extension in 2-dimensions of the discretization procedure, which is shown in A.2, we can already notice from Eq. (A.2.5) that essentially only the hopping terms from one site to another are changed by the phase difference of the two sites. This acquired phase can be reinterpreted as the vector potential picked up along the hopping path. Renaming the differences to the corresponding vector potentials A_x, A_y on the links doubles effectively the degree of freedoms, as there

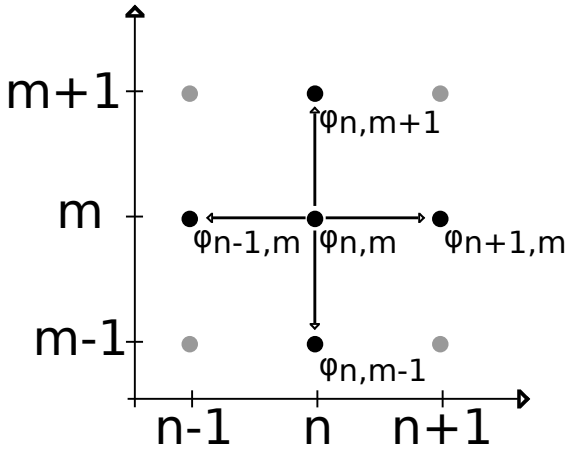

Figure A.2.: We can change the wave funtion on every lattice site by some arbitrary phase φ. The resulting physics will remain unchanged as quantum mechanics is invariant under a U(1) transformation.

are $2N^2$ links to N^2 lattice sites on a square lattice. One half of the degrees of freedom corresponds to the gauge freedom, which we have in the choice of the vector potential. The other half, we added by the reinterpretation implements the magnetic field now.

This procedure is known as the Peierls substitution, named after Rudolf Peierls [41] (some discussion can be found for example in [42]). The substitution practically means that we can add a magnetic field to a model without magnetic field by changing the hopping values on the link from site j to site i via

$$t_{ij} \to t_{ij} \exp\left(i\frac{e}{\hbar} \int_j^i \boldsymbol{A}(r)\mathrm{d}\boldsymbol{r} \right). \tag{A.3.2}$$

The line integral accounts for the picked up phase along the hopping path. This way, when we hop on the lattice in any closed loop ∂P, we yield essentially the number of magnetic flux quanta $\Phi_0 = h/e$ enclosed by the loop, corresponding to the magnetic field $\boldsymbol{B} = \mathrm{rot}\boldsymbol{A}$ that is perpendicular to the plane P

$$\frac{e}{\hbar} \oint_{\partial \mathrm{P}} \boldsymbol{A}(r)\mathrm{d}\boldsymbol{r} = \frac{e}{\hbar} \int_{\mathrm{P}} \boldsymbol{B}(r)\mathrm{d}\boldsymbol{f} = 2\pi \frac{\Phi}{\Phi_0}. \tag{A.3.3}$$

Note however that the Peierls substitution correctly implements the magnetic field within a model, only when the magnetic flux through a single plaquette of the lattice is small $\Phi \ll \Phi_0$. Otherwise effects of the Hofstadter butterfly become visible [43].

The Peierls substitution is not restricted to the square lattice model, but can be performed in the same way for any other tight binding model. In Ch. 4, we use it for example to add a magnetic field on a honeycomb lattice.

A.4. Density of States for a 2D System

We give the formulas for the density of states in 2-dimensional systems, which we will use in the Born approximation calculations of Sect. 3.2.1. For a periodic system which extends into each direction with length L, we have a discrete k-space with equidistant points, where each point takes a volume of $(L/2\pi)^d$. In two dimensions, the number of occupied states per volume up to the value k in k-space is calculated as

$$n = \int \frac{\mathrm{d}^2 k}{(2\pi)^2} = \frac{k^2}{4\pi}. \tag{A.4.1}$$

The density of states $D_{2d}(E)$ gives the number per volume of energy levels in the range $[E, \mathrm{d}E]$. Therefore, it can be calculated by taking the derivative of Eq. (A.4.1)

$$D_{2d}(E) = \frac{\mathrm{d}}{\mathrm{d}E} \frac{k^2}{4\pi} \tag{A.4.2}$$

For a system with a parabolic dispersion relation $E = \hbar^2 k^2 / 2m$ follows a constant density of states in two dimensions

$$D_{2d}^{\text{para.}}(E) = \frac{m}{2\pi\hbar^2}. \tag{A.4.3}$$

We can express it with the parameters of the tight binding model on a square lattice, which has a lattice spacing a and hopping $t = \hbar^2/2ma^2$ (see Sect. 3.1). We obtain

$$D_{2d}^{\text{para.}}(E) = \frac{1}{4\pi t a^2}, \tag{A.4.4}$$

which is used in Sect. 3.2.1. For a system with linear dispersion relation $E = \hbar v_{\mathsf{F}} k$ follows a linear density of states

$$D_{2d}^{\text{lin.}}(E) = \frac{1}{2\pi\hbar^2 v_{\mathsf{F}}^2} E. \tag{A.4.5}$$

We use it in the discussion of the staggered fermion model in Sect. 4.9.

A.5. Dispersion of a Quantum Hall System with Edge

In Sect. 3.3, we calculated the Landau levels for a system without disorder and edges. In this section, we want to see what effect a hard wall has on the energy levels. We can introduce a hard wall at $y = 0$ into our Hamiltonian (3.3.8) by adding a confinement potential

$$V_{\text{conf}}(y) = \begin{cases} 0 & \text{if } y \geq 0, \\ \infty & \text{if } y < 0. \end{cases} \tag{A.5.1}$$

The Hamiltonian remains translationally invariant in x-direction and the same ansatz as in Eq. (3.3.10) can be used. For $y > 0$ the same differential equation as in Eq. (3.3.12) has to be solved, but now the boundary condition $\phi_{nk_x}(0) = 0$ is added (additionally to the condition

that the wavefunction still needs to vanish for $y \to \infty$). Using $p_y = -i\hbar\partial_y$, we can write the Schrödinger equation as an ordinary second order differential equation for $\phi_k(y)$

$$\begin{cases} \left[-\frac{\hbar^2}{2m}\frac{\mathrm{d}^2}{\mathrm{d}y^2} + \frac{1}{2}m\omega_c^2\Big(y - l_B^2 k_x\Big)^2\right]\phi_{nk_x}(y) = E_n(k_x)\phi_{nk_x}(y), \\ \phi_{nk_x}(0) = 0. \end{cases} \tag{A.5.2}$$

The allowed eigenenergies will now depend on k_x, due to the boundary condition. The general solution of the differential equation can be expressed in terms of parabolic cylinder functions. To see this, we divide the differential equation by $\hbar\omega_c$ and get

$$\left[-\tfrac{1}{2}l_B^2\frac{\mathrm{d}^2}{\mathrm{d}y^2} + \tfrac{1}{2}\Big(y l_B^{-1} - l_B k_x\Big)^2\right]\phi_{nk_x}(y) = \frac{E_n(k_x)}{\hbar\omega_c}\phi_{nk_x}(y). \tag{A.5.3}$$

We will measure in the following energies in $\hbar\omega_c$ and lengths in l_B. This simplifies the problem to solving

$$\begin{cases} (\frac{1}{2}\frac{\mathrm{d}^2}{\mathrm{d}y^2} - \frac{1}{2}(y - k_x)^2 + E_n(k_x))\phi_{nk_x}(y) = 0, \\ \phi_{nk_x}(0) = 0. \end{cases} \tag{A.5.4}$$

The differential equation can be rewritten as

$$\left(\frac{\mathrm{d}^2}{\mathrm{d}z^2} - \frac{1}{4}z^2 - a\right)w = 0. \tag{A.5.5}$$

This equation has as a solution the parabolic cylinder function $U(a,z)$ [44], where $U(a,z)$ vanishes for $z \to \infty$. The parabolic cylinder function can be expressed using the confluent hypergeometric function

$${}_1F_1(a;b;z) = \sum_{n=0}^{\infty}\frac{a^{(n)}}{b^{(n)}n!}z^n, \tag{A.5.6}$$

where $a^{(n)} = a(a+1)(a+2)\dots(a+n-1)$ is the rising factorial ($a^{(0)} = 1$). Then with $\xi = \frac{1}{2}a + \frac{1}{4}$, the parabolic cylinder function reads

$$\begin{aligned} U(a,z) = \frac{1}{2^\xi\sqrt{\pi}}e^{-z^2/4}\Bigg[&\cos(\xi\pi)\Gamma\left(\tfrac{1}{2} - \xi\right){}_1F_1\left(\xi;\tfrac{1}{2};\tfrac{1}{2}z^2\right) \\ &-z\sqrt{2}\sin(\xi\pi)\Gamma(1-\xi){}_1F_1\left(\xi + \tfrac{1}{2};\tfrac{3}{2};\tfrac{1}{2}z^2\right)\Bigg]. \end{aligned} \tag{A.5.7}$$

By the substitution $z = \sqrt{2}(y - k_x)$ and $a = -E_n(k_x)$, the differential equation of the parabolic cylinder equation of Eq. (A.5.5) returns to our differential equation for the quantum Hall system, given in Eq. (A.5.4). Therefore, the solution to the differential equation is given by

$$\phi_{nk_x}(y) = U\Big(-E_n(k_x), \sqrt{2}(y - k_x)\Big), \tag{A.5.8}$$

where the allowed $E_n(k)$ values have to be determined by the boundary condition. They are obtained by the implicit equation

$$U\Big(-E_n(k_x), -\sqrt{2}k_x\Big) = 0. \tag{A.5.9}$$

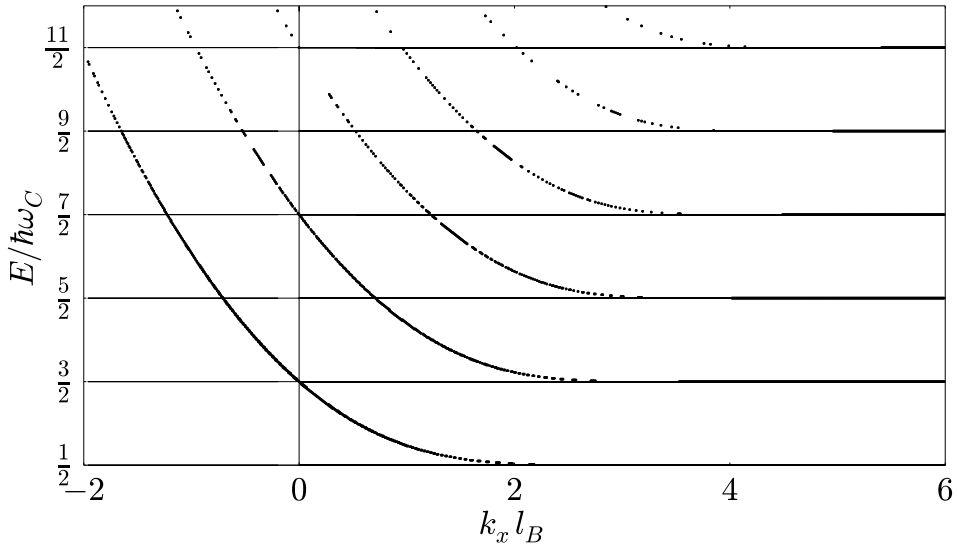

Figure A.3.: Due to the hard wall in the system the Landau levels in the dispersion relation bend upwards at the edge. At $k_x l_B = 0$, they take on the values of the half harmonic oscillator, whereas for $k_x l_B \gg 1$ they remain on the energy of the bulk Landau levels.

For $k_x = 0$, this describes just the half harmonic oscillator, and can be solved exactly. From $U(-E_n(0),0) = 0$, we get the equation

$$\cos\left(\frac{\pi}{4} - \frac{\pi}{2}E_n(0)\right)\Gamma\left(\frac{1}{4} + \tfrac{1}{2}E_n(0)\right) = 0. \tag{A.5.10}$$

The cosine function turns zero for $E_n(0) = 2n - \frac{1}{2}$, where as the Γ function restricts the integers to $n \in \mathbb{N}$, as it diverges otherwise. Thus, the eigenenergies of the half harmonic oscillator are given by every second energy of the full quantum harmonic oscillator. For $k_x \to \infty$ on the other hand, the wall is far away and therefore one retains the Landau levels from a bulk system. To understand this consider that we would have transformed the original problem of Eq. (A.5.2) by the transformation $\tilde{y} = y - l_B^2 k_x$. Then, the boundary condition from the wall potential would be that the wavefunction should vanish for $\tilde{y} < -l_B^2 k_x$. For $k_x \to \infty$, this is just the problem of the free harmonic oscillator without a hard wall.

For everything in between these two extremes, we can get the dispersion relation by numerically calculating the zeros of the parabolic cylinder function, which is shown in Fig. A.3. If we were to consider a second wall independent of the first one at the position $y = W$, we return to Eq. (A.5.2). We can transform the position variable by $y' = W - y$, and can reuse the previous results. This means, we will again obtain to an upbending of the dispersion relation, but this time at $k_x l_B = W/l_B$.

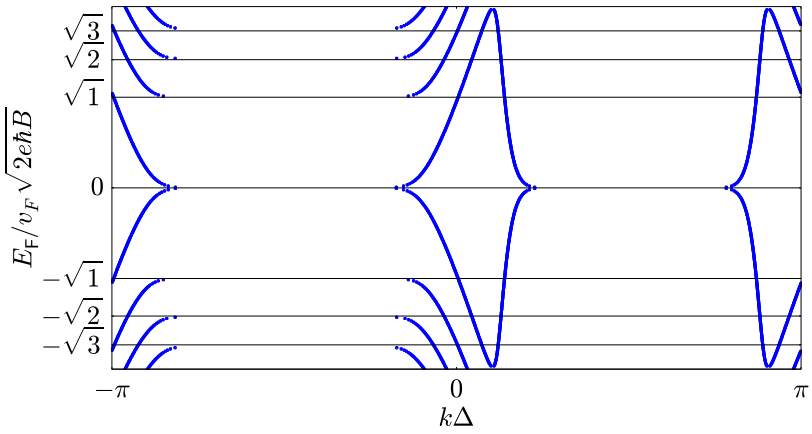

Figure A.4.: Implementing the magnetic field by starting from a gauge transformation doubles again the lowest mode, and therefore does not result in the expected result from a single Dirac cone. The dispersion relation was evaluated for a transfer matrix of Eq. (A.6.1), where the number of transverse lattice sites was $N = 101$, and the magnetic field was set to $B = \pi/N$.

A.6. Minimal Coupling in Staggered Fermions

In A.3, we showed how the effect of a vector potential can be introduced in a model by a U(1) gauge transformation. In this section, we want to see why we did not use this procedure for the staggered fermion model of Sect. 4.9. As we did before, we have to dress the wavefunction with the collected phase along the path to the site where it is being evaluated. Meaning in the structure of the lattice shown in Fig. 4.21, we have to add the phase collected along each path from the filled circles to the empty circles, where the Dirac equation is evaluated. There are ambiguities, as to which path to choose in the evaluation. This should however be unimportant if the relevant physical length scales are greater than the lattice spacing. The details as to how the new matrices J, K are defined, depends on where we define to evaluate the value of the vector potential (whether we evaluate them at each link, or choose a mean value at the crossed site, etc.). For a simple example, we only discuss the Landau gauge in the following with $A_y = 0$ and evaluate the vector potential at the links with $A_x = -By$. The resulting transfer matrix of this scheme has the form

$$M_m = (\mathcal{J} + iX_m)^{-1} \exp\left(i\mathcal{A}_x^{(m)}\right)(\mathcal{J} - iX_m), \tag{A.6.1}$$

with $X_m = \sigma_z\mathcal{K} + \frac{1}{2}\sigma_x\mathcal{V}^{(m)}$, and $\mathcal{A}_x^{(m)}$ as a diagonal matrix build by the vector potential values of the links associated with the m^{th} slice.

We show in Fig. A.4 the resulting dispersion relation of the transfer matrix from Eq. (A.6.1). Note however, that the chosen magnetic field is not completely consistent with the periodic boundary conditions of the model. Choosing multiples of $B = 2\pi/N$ does not result in any

propagating mode. Therefore, we chose $B = \pi/N$. We see in the spectrum that the lowest mode has doubled and we did not achieve to produce the expected dispersion of the single Dirac cone. Similar results were already obtained in a discussion in the framework of QED [45]. We therefore stepped back from trying to implement the magnetic field by a gauge transformation, especially as another great problem is to find a simple expression for the current operator of the system.

A.7. Computation Time

In the numerical study, we are limited in the number of lattice sites by the computation time and memory needed to evaluate the algorithms. We evaluated most calculations, which are presented in this thesis, on a system with a Intel(R) Core(TM) i7-2630QM processor and 8 Gb of memory. Several comparable systems from a cluster, which is located at the physics department of the university, were used to increase the computation power by the parallelization of the simulations. In Fig. A.5, we show the rough time needed for the calculation of the transmission probability of a two-terminal system of size $L \times L$, where the lattice constant a is defined respectively in Sect. 3.1, Sect. 4.1 and Sect. 4.9.

We can evaluate from the data that our calculations with kwant scale approximately with the system size in the order of $\mathcal{O}(L^{2.3})$. The offset from the calculation on the square lattice and the honeycomb lattice are due to the increased number of lattice sites per area in the honeycomb structure. The code used in the evaluation of the staggered fermion model is less optimized compared to the elaborate kwant code, and therefore it scales a bit worse in the order of $\mathcal{O}(L^{3.4})$. Consequently, as we are also interested in simulating systems for many different parameter regimes, we are somehow limited to simulating systems that are smaller than $L < 500a$ to keep the computation time on an acceptable level. Otherwise it quickly starts to exceed days. For systems of this size, the memory needed is below $\mathcal{O}(1\,\text{Gb})$, which is no limiting factor for modern computers. In the publication of the kwant group [8] further details on the computation time and memory requirement of simulations based on kwant can be found.

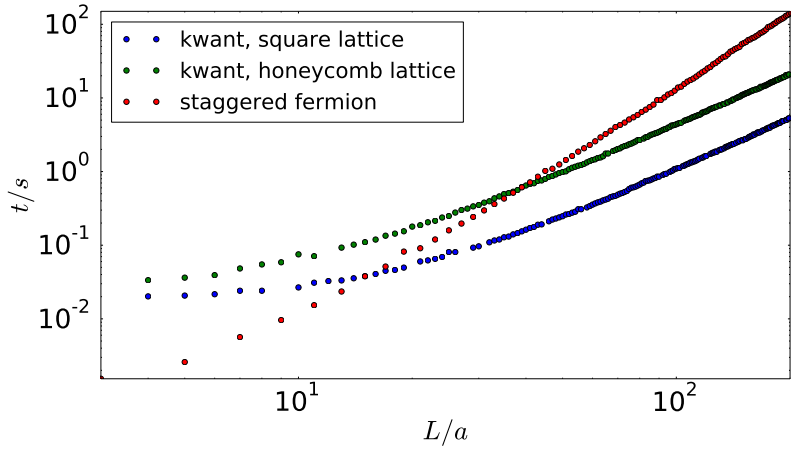

Figure A.5.: We show the computation time needed for the simulation of the transmission probability of a two-terminal system of size $L \times L$. The data shows that the computation time scales for systems, which are simulated with the kwant package, roughly in the order $\mathcal{O}(L^{2.3})$, and for the non-optimized staggered fermion code in the order of $\mathcal{O}(L^{3.4})$.

Acknowledgments

During the year that I performed my master thesis, I had the opportunity to learn a lot about contemporary research topics. I want to use this space to thank my supervisor Prof. Dr. Fabian Hassler for the countless discussions we had during this year. The topics we discussed, most of the time over the course of a few weeks, sometimes because of possible research topics, sometimes just because they are interesting, were always great sources to learn about new techniques. And as so much time is spent on topics, which do not find their way into a thesis, I feel at least obliged to count a list of topics I additionally learned about from Prof. Hassler: singular value decomposition, the polar decomposition of the scattering matrix and algorithms to optimize the numerical calculations, Lie groups and limits of the Baker-Campbell-Hausdorff formula in an attempt to optimize the transfer matrix formalism, series acceleration, palindromic eigenvalue equations, recursive Green's function algorithms as well as nested dissection algorithms, renormalization group procedures and scaling in the quantum Hall transitions, DMPK equation and stochastic differential equations in general, etc. During the thesis, Prof. Hassler was a great teacher, and always found encouraging words to step forward in the process.

I also want to thank Prof. Dr. Christoph Stampfer and his group, especially Gerard Verbiest and Jan Dauber, who provided me with experimental insights, and were therefore always a great and fruitful source for new projects to research.

Besides, I would like to thank everyone from the IQI in Aachen for the great working atmosphere and the daily discussions. Especially, I would like to thank Jascha Ulrich, who seems to be a walking Python library and could always help me with a smile on several small occasions.

Last but not least, I would like to thank my father, who had set through hard labor the conditions for me in life, such that I could pursue a career in science.

G. Glossary

Common Symbols and Definitions

o = outgoing mode (G.1)

i = incoming mode (G.2)

e = evanescent mode (G.3)

χ^a_m = transverse eigenstate of m^{th} eigenmode of lead for $a \in (\mathsf{o},\mathsf{i},\mathsf{e})$ (G.4)

λ^a_m = longitudinal eigenvalue of m^{th} eigenmode of lead for $a \in (\mathsf{o},\mathsf{i},\mathsf{e})$ (G.5)

H_{L} = Hamiltonian of lead unit cell (G.6)

T_{L} = Hopping matrix connecting two lead unit cells (G.7)

H_{S} = Hamiltonian of system (G.8)

T_{LS} = Matrix connecting system and lead (G.9)

$U_a = \left(\chi^a_1,\chi^a_2,\ldots,\chi^a_{N_a}\right)$, for $a \in (\mathsf{o},\mathsf{i},\mathsf{e})$ (G.10)

$\Lambda_a = \mathsf{diag}\left(\lambda^a_1,\lambda^a_2,\ldots,\lambda^a_{N_a}\right)$, for $a \in (\mathsf{o},\mathsf{i},\mathsf{e})$ (G.11)

$T_{ab} = \Lambda^\dagger_a U^\dagger_a T_{\mathsf{L}} U_b$, for $a,b \in (\mathsf{o},\mathsf{i},\mathsf{e})$ (G.12)

$T_{a\mathsf{s}} = \Lambda^\dagger_a U^\dagger_a T_{\mathsf{LS}}$, for $a \in (\mathsf{o},\mathsf{i},\mathsf{e})$ (G.13)

$K_{ab} = T_{ab} - T_{a\mathsf{e}} \dfrac{1}{T_{\mathsf{ee}}} T_{\mathsf{e}b}$, for $a,b \in (\mathsf{o},\mathsf{i},\mathsf{s})$ (G.14)

$W = \frac{1}{\sqrt{2\pi}} K^{-1}_{\mathsf{ii}} K_{\mathsf{is}}$ (G.15)

$W^\dagger W = \frac{1}{\pi} K_{\mathsf{si}}\, \mathsf{Im}\Big(K^{-1}_{\mathsf{ii}}\Big) K_{\mathsf{is}}$ (G.16)

$\Delta = T_{\mathsf{se}} T^{-1}_{\mathsf{ee}} T_{\mathsf{es}} + K_{\mathsf{si}}\, \mathsf{Re}\Big(K^{-1}_{\mathsf{ii}}\Big) K_{\mathsf{is}}$ (G.17)

$U_< = (U_{\mathsf{o}},U_{\mathsf{e}})$ (G.18)

$$U^{-1}_< = \begin{pmatrix} \Upsilon^\dagger_{\mathsf{o}} \\ \Upsilon^\dagger_{\mathsf{e}} \end{pmatrix} \tag{G.19}$$

$$\Lambda_< = \begin{pmatrix} \Lambda_{\mathsf{o}} & 0 \\ 0 & \Lambda_{\mathsf{e}} \end{pmatrix} \tag{G.20}$$

$g T_{\mathsf{L}} = U_< \Lambda_< U^{-1}_<$ (G.21)

$\Gamma = i\Big(T^\dagger_{\mathsf{L}} U_< \Lambda_< U^{-1}_< - U^{-1\,\dagger}_< \Lambda^\dagger_< U^\dagger_< T_{\mathsf{L}}\Big)$ (G.22)

$C_{\mathsf{io}} = U^\dagger_{\mathsf{i}} \Gamma U_{\mathsf{o}}$ (G.23)

Identities for the K matrices

We list various identities for the K-matrices defined by (A.1.16) which follow from the definitions and are useful for calculations.

$$K_{oo} - K_{oo}^{\dagger} = i\mathbb{1} \tag{G.24}$$

$$K_{ii} - K_{ii}^{\dagger} = -i\mathbb{1} \tag{G.25}$$

$$K_{so}\frac{1}{K_{oo}}K_{os} = K_{si}\frac{1}{K_{ii}^{\dagger}}K_{si} \tag{G.26}$$

$$K_{oi} = \Lambda_o^{\dagger}C_{oi}\Lambda_i K_{ii} \tag{G.27}$$

$$K_{io} = \Lambda_i^{\dagger}C_{io}\Lambda_o K_{oo} \tag{G.28}$$

$$K_{oi} = K_{oo}C_{oi} \tag{G.29}$$

$$K_{io} = K_{ii}C_{io} \tag{G.30}$$

$$K_{si} = K_{so}\Lambda_o^{\dagger}C_{oi}\Lambda_i \tag{G.31}$$

$$C_{oi} - \Lambda_o^{\dagger}C_{oi}\Lambda_i = \left(\mathbb{1} - \frac{K_{oo}}{K_{oo}^{\dagger}}\right)C_{oi} \tag{G.32}$$

$$\left(\mathbb{1} - \frac{K_{oo}}{K_{oo}^{\dagger}}\right) = -i\frac{1}{K_{oo}^{\dagger}} \tag{G.33}$$

$$K_{si} - K_{so}\frac{1}{K_{oo}}K_{oi} = iK_{si}\frac{1}{K_{ii}^{\dagger}} \tag{G.34}$$

$$\frac{1}{K_{oo}}K_{os} = C_{oi}\frac{1}{K_{ii}}K_{is} \tag{G.35}$$

(G.36)

Bibliography

[1] K. S. Novoselov et al. "Electric Field Effect in Atomically Thin Carbon Films". In: *Science* 306.5696 (2004), pp. 666–669.

[2] F. Schwierz. "Graphene transistors". In: *Nature Nanotechnology* 5.7 (2010), pp. 487–496.

[3] H. Bruus and K. Flensberg. *Many-body quantum theory in condensed matter physics*. Oxford Graduate Texts, 2004.

[4] S. Datta. *Electronic Transport in Mesoscopic Systems*. Cambridge University Press, 2005.

[5] S. Datta. *Quantum Transport: Atom to Transistor*. Cambridge University Press, 2005.

[6] E. Akkermans and G. Montambaux. *Mesoscopic Physics of Electrons and Photons*. Cambridge University Press, 2007.

[7] Y. Imry. *Introduction to mesoscopic physics*. Oxford University Press, 1997.

[8] C. W. Groth et al. "Kwant: a software package for quantum transport". In: *New Journal of Physics* 16 (2014), p. 063065.

[9] M. Wimmer. "Quantum transport in nanostructures: From computational concepts to spintronics in graphene and magnetic tunnel junctions". PhD thesis. Universität Regensburg, 2009.

[10] F. Tisseur and K. Meerbergen. "The Quadratic Eigenvalue Problem". In: *SIAM* 43.2 (2001), pp. 235–286.

[11] T.-M. Huang et al. "Structure-Preserving Arnoldi-type Algorithms for Solving Palindromic Quadratic Eigenvalue Problems in Leaky Surface Wave Propagation". In: *JAMC* 219.19 (2013), pp. 9947–9958.

[12] D. Kressner et al. "Implicit QR algorithms for palindromic and even eigenvalue problems". In: *Numer. Algor.* 51.2 (2008), pp. 209–238.

[13] P. W. Brouwer. "On the Random-Matrix Theory of Quantum Transport". PhD thesis. Leiden University, 1997.

[14] Y. Blanter and M. Büttiker. "Shot Noise in Mesoscopic Conductors". In: *Phys. Rep.* 336.1–2 (2000), pp. 1–166.

[15] D. S. Fisher and P. A. Lee. "Relation between conductivity and transmission matrix". In: *Phys. Rev. B* 23.23 (1981), pp. 6851–6854.

[16] M. Büttiker. "Four-Terminal Phase-Coherent Conductance". In: *Phys. Rev. L.* 57.14 (1986), pp. 1761–1764.

[17] T. Giamarchi et al. *Introduction to Many Body Physics*. Lecture notes. 2013. URL: http://dpmc.unige.ch/gr_giamarchi/Solides/Files/many-body.pdf.

[18] S. Souma and A. Suzuki. "Local density of states and scattering matrix in quasi-one-dimensional systems". In: *Phys. Rev. B* 65 (2002), p. 115307.

[19] G. D. Mahan. *Many-Particle Physics*. 3rd ed. Kluwer Academic / Plenum Publishers, 2000.

[20] C. W. J. Beenakker and H. van Houten. "Quantum Transport in Semiconductor Nanostructures". In: *Solid State Physics* 44 (1991), pp. 1–228.

[21] C. W. J. Beenakker. "Random-matrix theory of quantum transport". In: *Rev. Mod. Phys.* 69 (1997), pp. 731–808.

[22] P. W. Anderson et al. "Scaling Theory of Localization: Absence of Quantum Diffusion in Two Dimensions". In: *Phys. Rev. L.* 42.10 (1979), pp. 673–676.

[23] P. Lee and T. V. Ramakrishnan. "Disordered electronic systems". In: *Rev. Mod. Phys.* 57.2 (1985), pp. 287–337.

[24] Z. Fan et al. "Anderson localization in two-dimensional graphene with short-range disorder: One-parameter scaling and finite-size effects". In: *Phys. Rev. B* 89 (2014), p. 245422.

[25] K. Nomura et al. "Quantum Hall Effect of Massless Dirac Fermions in a Vanishing Magnetic Field". In: *Phys. Rev. L.* 100 (2008), p. 246806.

[26] T. Ando et al. "Theory of Hall Effect in a Two-Dimensional Electron System". In: *J. Phys. Soc. Jpn* 39 (1975), pp. 279–288.

[27] A. Tzalenchuk et al. "Towards a quantum resistance standard based on epitaxial graphene". In: *Nature Nanotechnology* 5 (2010), pp. 186–189.

[28] M. O. Goerbig. "Quantum Hall Effects". In: (2009). Lecture notes.

[29] B. Huckestein. "Scaling theory of the integer quantum Hall effect". In: *Rev. Mod. Phys.* 67.2 (2014), pp. 357–396.

[30] L. A. Fal'kovskii. "Density Attenuation of Surface Magnetic States". In: *Soviet Physics Jetp* 31.5 (1969), pp. 981–987.

[31] M. M. Kettenis and L. G. Suttorp. "Charge and current density profiles of a degenerate magnetized free-electron gas near a hard wall". In: *J. Phys. A: Math. Gen.* 31 (1998), pp. 6547–6560.

[32] A. H. Castro Neto et al. "The electronic properties of graphene". In: *Rev. Mod. Phys.* 81 (2009), pp. 109–162.

[33] K. Wakabayashi et al. "Electronic states of graphene nanoribbons and analytical solutions". In: *Sci. Technol. Adv. Mater.* 11 (2010), p. 054504.

[34] P. Dietl. "Numerical Studies of Electronic Transport through Graphene Nanoribbons with Disorder". MA thesis. Karlsruhe Institute of Technology, 2009.

[35] S. Russo et al. "Aharonov-Bohm effect in graphene". In: *Phys. Rev. B* 77.8 (2008), p. 085413.

[36] M. A. H. Vozmediano et al. "Gauge fields in graphene". In: *Phys. Rep.* 496.4-5 (2010), pp. 109–150.

[37] E.M. Lifschitz L.D. Landau. *Theory of Elasticity*. 3rd ed. Vol. 7. Pergamon Press, 1986.

[38] J. Tworzydlo et al. "Finite difference method for transport properties of massless Dirac fermions". In: *Phys. Rev. B* 78 (2008), p. 235438.

[39] R. Stacey. "Eliminating lattice fermion doubling". In: *Phys. Rev. D* 26.2 (1982), pp. 468–472.

[40] A. R. Hernandez and C. H. Lewenkopf. "Finite difference method for transport of two-dimensional massless Dirac fermions in a ribbon geometry". In: *Phys. Rev. B* 86.15 (2012), p. 155439.

[41] R. Peierls. "Zur Theorie des Diamagnetismus von Leitungselektronen". In: *Z. f. Phys.* 81.3–4 (1933), pp. 186–194.

[42] M. Höck. "Exakte und approximative Untersuchung kleiner Systeme im Hubbard-Modell". MA thesis. Bielefeld University, 2008.

[43] D. R. Hofstadter. "Energy levels and wave functions of Bloch electrons in rational and irrational magnetic fields". In: *Phys. Rev. B* 14.6 (1976), pp. 2239–2249.

[44] F. W. J. Olver et al. *NIST Handbook of Mathematical Functions*. Cambridge University Press, 2010.

[45] R. Stacey. "Gauge Invariance and Fermion Doubling". In: *Z. Phys. C - Particles and Fields* 19 (1983), pp. 75–78.